



A National Center of Excellence in Advanced Technology Applications

ISSN 1520-295X

Seismic Evaluation of a Masonry Infilled Reinforced Concrete Frame by Pseudodynamic Testing

by

Stephen G. Buonopane and Richard N. White

Cornell University

School of Civil and Environmental Engineering

Hollister Hall

Ithaca, New York 14853-3501

Technical Report MCEER-99-0001

February 16, 1999

This research was conducted at Cornell University and was supported in whole or in part by the National Science Foundation under Grant No. BCS 90-25010.

NOTICE

This report was prepared by Cornell University as a result of research sponsored by the Multidisciplinary Center for Earthquake Engineering Research (MCEER) through a grant from the National Science Foundation and other sponsors. Neither MCEER, associates of MCEER, its sponsors, Cornell University, nor any person acting on their behalf:

- a. makes any warranty, express or implied, with respect to the use of any information, apparatus, method, or process disclosed in this report or that such use may not infringe upon privately owned rights; or
- b. assumes any liabilities of whatsoever kind with respect to the use of, or the damage resulting from the use of, any information, apparatus, method, or process disclosed in this report.

Any opinions, findings, and conclusions or recommendations expressed in this publication are those of the author(s) and do not necessarily reflect the views of MCEER, the National Science Foundation, or other sponsors.



Seismic Evaluation of a Masonry Infilled Reinforced Concrete Frame by Pseudodynamic Testing

by

Stephen G. Buonopane¹ and Richard N. White²

Publication Date: February 16, 1999

Submittal Date: January 26, 1998

Technical Report MCEER-99-0001

Task Number 95-3111A

NSF Master Contract Number BCS 90-25010

- 1 Senior Engineer, Simpson Gumpertz and Heger Inc., Arlington, MA; former Graduate Research Assistant, School of Civil and Environmental Engineering, Cornell University
- 2 James A. Friend Family Professor of Engineering, School of Civil and Environmental Engineering, Cornell University

MULTIDISCIPLINARY CENTER FOR EARTHQUAKE ENGINEERING RESEARCH
University at Buffalo, State University of New York
Red Jacket Quadrangle, Buffalo, NY 14261

Preface

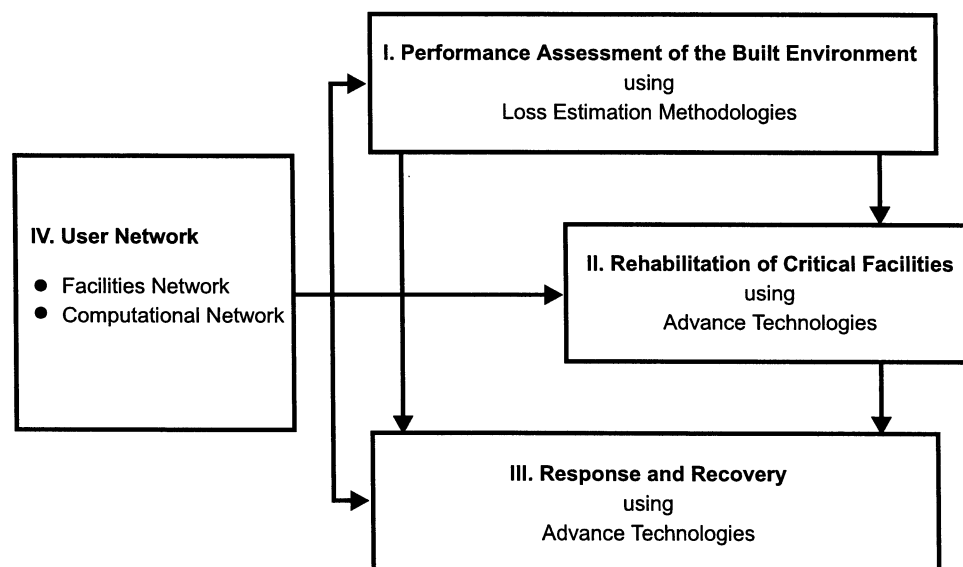
The Multidisciplinary Center for Earthquake Engineering Research (MCEER) is a national center of excellence in advanced technology applications that is dedicated to the reduction of earthquake losses nationwide. Headquartered at the University at Buffalo, State University of New York, the Center was originally established by the National Science Foundation in 1986, as the National Center for Earthquake Engineering Research (NCEER).

Comprising a consortium of researchers from numerous disciplines and institutions throughout the United States, the Center's mission is to reduce earthquake losses through research and the application of advanced technologies that improve engineering, pre-earthquake planning and post-earthquake recovery strategies. Toward this end, the Center coordinates a nationwide program of multidisciplinary team research, education and outreach activities.

MCEER's research is conducted under the sponsorship of two major federal agencies: the National Science Foundation (NSF) and the Federal Highway Administration (FHWA), and the State of New York. Significant support is derived from the Federal Emergency Management Agency (FEMA), other state governments, academic institutions, foreign governments and private industry.

The Center's NSF-sponsored research is focused around four major thrusts, as shown in the figure below:

- quantifying building and lifeline performance in future earthquake through the estimation of expected losses;
- developing cost-effective, performance based, rehabilitation technologies for critical facilities;
- improving response and recovery through strategic planning and crisis management;
- establishing two user networks, one in experimental facilities and computing environments and the other in computational and analytical resources.



This report presents the results from a seismic evaluation of masonry infilled frames performed by pseudodynamic testing. The test specimen was a two-story, two-bay half-scale model, which was subjected to four pseudodynamic tests of increasing magnitude. The experimental program provided detailed data on the behavior of frames and infills under realistic seismic loading conditions. The data can be used to calibrate and verify advanced finite element methods and to improve simple analytical models for evaluation and design.

ABSTRACT

Seismic evaluation of a masonry infilled frame was performed by pseudodynamic testing. The half-scale experimental specimen consisted of a two-story, two-bay, lightly reinforced concrete frame infilled with unreinforced concrete masonry block. The second story infill included window openings. Following stiffness and damping characterization by static and free vibration tests, the specimen was subjected to four pseudodynamic tests of increasing magnitude, based on the Taft (1952) ground motion. Explicit numerical integration with a small time step and an iterative actuator control algorithm limited the displacement control errors normally associated with pseudodynamic testing of stiff structures. The displacement control matrix necessary for the iterative actuator control was directly measured.

The final sequence of pseudodynamic tests produced extensive cracking in both upper and lower story masonry infill, as well as distress in frame columns. Relations between energy dissipation and the types of observed masonry cracking are investigated. A detailed history of crack development is presented, keyed to both story hysteresis and input excitation. Evidence of compressive strut mechanisms are drawn from frame moments and axial forces, and measured local strains and infill panel diagonal changes of length. Simple strut models are used to estimate infill stiffnesses and strut forces, and the results are compared with measured values. The effects of infill bed-joint shear failures on overall behavior are investigated with a simple analytical model. Estimated infill shear strength is shown to be highly dependent upon the assumed coefficient of friction.

ACKNOWLEDGMENTS

The experimental work for this research was conducted in the George Winter Laboratory for Structural Engineering at Cornell University and would not have been possible without the many dedicated, expert hours of Tim Bond, manager of the Winter Laboratory. Dave Farmer was always willing and able to lend a helpful hand at a wide range of tasks in the lab. The assistance of Daniel Morrissey helped keep the construction process moving along smoothly.

Cornell Professors Gregory G. Deierlein, Kenneth C. Hover and Mircea Grigoriu contributed valuable advice in specific areas of the work. Professor Khalid Mosalam of the University of California at Berkeley also made available the benefit of his research and experience in pseudodynamic testing.

The first author gratefully acknowledges the financial assistance provided as a part of the ACI-W.R. Grace Fellowship.

TABLE OF CONTENTS

SECTION	TITLE	PAGE
1.	OVERVIEW	1
1.1.	Objectives	1
1.2.	Experimental Scope	3
1.2.1.	Gravity Load Designed Frame	3
1.2.2.	Unreinforced Masonry with Openings	5
1.2.3.	Similitude Requirements	5
1.2.4.	Input Ground Motion	7
1.3.	Behavior of Masonry Infilled Frames	9
1.3.1.	Failure Modes	9
1.3.2.	Previous Research	10
2.	MATERIALS	15
2.1.	Mix Design	15
2.2.	Concrete and Steel Properties	15
2.3.	Masonry Testing	18
3.	EXPERIMENTAL SET-UP	21
3.1.	Loading System	21
3.2.	Strain Gages	21
3.3.	Displacement Transducers	22
4.	SPECIMEN CHARACTERIZATION	25
4.1.	Bare Frame	25
4.1.1.	Free Vibration Testing	25
4.1.2.	Flexibility Testing	27
4.2.	Infilled Frame	29
4.2.1.	Free Vibration Testing	29
4.2.2.	Flexibility Testing	29
4.2.3.	Analytical Verification	31
4.3.	Damage and Repair	32
4.4.	Recharacterization	33
4.4.1.	Flexibility Testing	33
4.4.2.	Shear Building Model	33
4.4.3.	Stiffness Testing	35
4.4.4.	Hysteretic Energy Dissipation	37
5.	PSEUDODYNAMIC METHOD	39
5.1.	Conceptual Basis	39
5.2.	Development of Pseudodynamic Testing	40
5.3.	Mathematical Formulation	43
5.4.	Control Algorithm for Stiff Structures	43
5.4.1.	Dual Displacement Control	43
5.4.2.	“Soft Coupling” Formulation	45

TABLE OF CONTENTS (cont'd)

SECTION	TITLE	PAGE
5.4.3.	Determination of Q Matrix	49
6.	PSEUDODYNAMIC IMPLEMENTATION	53
6.1.	Mass and Damping Properties	53
6.2.	Control Parameters	54
7.	PSEUDODYNAMIC VERIFICATION	57
7.1.	Bilinear Modeling of a Low-Level Test	57
7.2.	Sources of Error	58
7.3.	Tolerance and Displacement Error	62
7.4.	Over- and Undershooting Errors	63
7.5.	Numerical Simulation of Displacement Error	64
8.	PSEUDODYNAMIC RESULTS	65
8.1.	Testing Sequence	65
8.2.	Global Behavior	66
8.2.1.	Story Hysteretic Relations	67
8.2.2.	Energy Dissipation	75
8.2.3.	Frequency Spectra	80
8.3.	Masonry Crack Development	83
8.4.	Local Behavior Critical Event Series	88
8.5.	Infill-Frame Interaction	88
8.5.1.	Maximum Base Shear Series	88
8.5.2.	Maximum First Story Displacement Series	96
8.5.3.	Column Shear Cracking	96
8.6.	Infill Panel Behavior	101
8.6.1.	Strain Rosettes	101
8.6.2.	Panel DCDTs	102
8.7.	Strut Mechanisms	108
8.7.1.	Effective Strut Width and Stiffness	108
8.7.2.	Experimental Strut Forces	110
8.8.	Infill Shear Behavior	112
9.	CONCLUSIONS	117
9.1.	Pseudodynamic Testing	117
9.2.	Experimental Behavior and Strut Mechanisms	118
9.3.	Recommendations for Future Research	119
9.4.	Recommendations for Analysis and Design	120
10.	REFERENCES	123

LIST OF TABLES

TABLE	TITLE	PAGE
1-1	Scale Factors for Pseudodynamic Testing	6
2-1	Final Mix Proportions	15
2-2	28-day Cylinder Test Summary	16
2-3	28-day Split Cylinder Test Summary	16
2-4	15-month Cylinder Test Summary	16
2-5	15-month Split Cylinder Test Summary	16
2-6	Average Steel Properties	17
2-7	CMU Physical Properties	18
2-8	Masonry Block Compressive Properties	19
2-9	Mortar Cylinder Compressive Properties	19
2-10	Mortar Split Cylinder Properties	19
2-11	Masonry Prism Properties	19
2-12	Masonry Shear Properties	19
4-1	Bare Frame Characteristics	28
4-2	Infilled Frame Frequencies	32
6-1	Prototype Specimen Dead Loads	53
7-1	Bilinear Parameters	58
7-2	Displacement Tolerance	62
8-1	Linear Estimates of Initial Stiffnesses	73
8-2	Story Hysteretic Energies	76
8-3	Dissipated Energy	80
8-4	Maximum Base Shear Series	88
8-5	Maximum First Story Displacement Series	88
8-6	Rosette Strains: Maximum Base Shear Series	104
8-7	Rosette Strains: Maximum First Story Displacement Series	104
8-8	Panel Diagonal Displacements Due to Racking Deformation	107

LIST OF ILLUSTRATIONS

FIGURE	TITLE	PAGE
1-1	Specimen Elevation	2
1-2	Plan of Prototype Structure	4
1-3	GLD Frame Features	4
1-4	Interaction Diagrams	5
1-5	Taft 1.0g Accelerogram	8
1-6	Taft 1.0g Response Spectrum	8
1-7	Infilled Frame Failure Modes	9
2-1	Typical Cylinder Stress-Strain Curves	16
2-2	Typical Reinforcement Stress-Strain Curves	17
2-3	Average CMU Dimensions	18
2-4	Typical Masonry Stress-Strain Curves	20
3-1	Loading System Elevation	22
3-2	Strain Gage Locations—South Face	23
3-3	Displacement Transducers—North Face	24
3-4	Displacement Transducers—South Face	24
4-1	Bare Frame Free Vibration Test	26
4-2	Bare Frame Free Vibration Modal Response	27
4-3	Infilled Frame Free Vibration Test	30
4-4	Infilled Frame Flexibility Tests	31
4-5	Infilled Frame Flexibility Tests	34
4-6	Infilled Frame Story Stiffness Tests	36
5-1	Explicit Pseudodynamic Algorithm	44
5-2	Pseudodynamic Control Schematic	45
5-3	“Soft-Coupling” Idealization	46
5-4	Displacement Cycle with Load System Interaction	50
5-5	Q Matrix Test Results	52
7-1	Bilinear Hysteresis Rules	58
7-2	Bilinear and Measured Displacement Time Histories	59
7-3	Bilinear and Measured Hysteretic Relations	60
7-4	Bilinear and Measured Frequency Spectra	61
8-1	Normalized Deflected Shapes at Peak 1st Story Displacements	66
8-2	Taft 0.10g Story Hysteresis	68
8-3	Taft 0.35g Story Hysteresis	69
8-4	Taft 0.55g Story Hysteresis	70
8-5	Taft 0.80g Story Hysteresis	71
8-6	Gap Opening Displacement at DT32	72

8-7	Linear Estimates of Initial Stiffnesses: (a) First Story; (b) Second Story	73
8-8	Final Crack Patterns: (a) Taft 0.55g; (b) Taft 0.80g	74
8-9	Taft 0.55g Story Hysteretic Energies	76
8-10	Normalized Story Hysteretic Energies	76
8-11	Taft 0.10g Energy Components	77
8-12	Taft 0.35g Energy Components	78
8-13	Taft 0.55g Energy Components	78
8-14	Taft 0.80g Energy Components	79
8-15	Dissipated Energy: (a) Energy Increase with p_{ga} ; (b) Normalized Hysteretic and Damping Fractions	79
8-16	1st Story Displacements: Taft 0.10g and Taft 0.80g	81
8-17	1st Story Displacement Frequency Spectra: Taft 0.10g and Taft 0.80g	82
8-18	Taft 0.80g 1st Story Displacement Frequency Spectra: Initial and Final	82
8-19	Taft 0.80g Crack Development: (a) 0.00 sec to 5.13 sec (b) 5.45 sec to 6.65 sec (c) 9.44 sec to 10.76 sec	84
8-20	Taft 0.80g 1st Story Hysteresis and Associated Input Motion	87
8-21	Taft 0.80g Strain Gage Time Histories	90
8-22	Moment and Axial Diagrams for Maximum Base Shear Series	91
8-23	Hypothesized Strut Mechanism	95
8-24	Moment and Axial Diagrams for Maximum 1st Story Displacement Series	97
8-25	Strain Gage Rosette Locations	102
8-26	Taft 0.55g Strain Gage Rosette Time Histories	103
8-27	Taft 0.35g DCDT Time Histories	105
8-28	Taft 0.35g DCDT Displacements at Maximum Base Shear	106
8-29	Taft 0.80g DCDT Displacements at Maximum Base Shear	107
8-30	Infill Panel Dimensions	110
8-31	Strut Configurations	111
8-32	Shear Strength Dependence on μ	115

SECTION 1 OVERVIEW

1.1. Objectives

Much of the existing building stock in the United States and worldwide consists of structures designed without the benefit of up-to-date seismic design procedures and, therefore, are particularly vulnerable to damage during a seismic event. The potential for such widespread damage in such areas as the Eastern United States had led to substantial research efforts into the assessment of existing buildings during the past decade. Assessment, repair and rehabilitation have been a major component of research sponsored by the National Center for Earthquake Engineering Research (NCEER, 1994) as well as a National Science Foundation initiative, "Repair and Rehabilitation Research for Seismic Resistance of Structures" (Jirsa, 1996).

Reinforced concrete frames infilled with masonry form the structural system of many of these vulnerable buildings. The reinforced concrete frames typically have been designed for gravity loads only (GLD), and common design practice considers the infill a non-structural component. By neglecting the masonry infill during design of the frame, one is assuming that the final infilled structure will have the same reliability as the frame alone. Such a belief is vastly misleading. Historically, such structures have been plagued with poor performance during seismic events. Paulay and Priestley (1992) cite examples from the Philippine earthquake of 1990; while Abrams (1994) contains a paper detailing damage in Cairo, Egypt from a moderate event in 1992. Numerous other examples may be found in reconnaissance reports. Clearly the "non-structural" masonry infill can drastically alter the seismic behavior of infilled frames. The complex interaction between frame and infill makes lateral strength and seismic behavior difficult to quantify.

The complexity of the interactive behavior has resulted in heavy reliance on experimental research, and more recently, on advanced computer modeling. Despite nearly four decades of experimental research, resolutions from a technical workshop (Abrams, 1994), detail certain areas that need further investigation for the proper evaluation of the seismic performance of infilled frames. Among these research needs were:

1. Behavior of infills with openings.
2. Effects of infill on weak, non-ductile (i.e. GLD) frames.
3. Extrapolation of existing knowledge to multi-bay, multi-story frames.

The current research program addresses these three specific needs through the pseudodynamic (PSD) testing of a two-story, two-bay specimen at half-scale (Figure 1-1). The specimen consists of a GLD reinforced concrete frame infilled with unreinforced concrete masonry units (CMU), with window

openings in the second story walls. The experimental program provides detailed data on the behavior of frame and infill under realistic seismic loading. The data presented is intended for calibrating and verifying advanced finite element models, and, in conjunction with such models, to improve simple but effective analytical models which can be used for evaluation and design.

The remainder of this chapter will introduce the prototype structure and model specimen used for this experimental program and briefly review previous relevant experimental research.

1.2. Experimental Scope

A low rise structure composed of a series of concrete frames serves as the prototype structure for the pseudodynamic experimentation, as shown in plan in Figure 1-2. GLD frames with unreinforced masonry infills as partitions are a common style of construction for many older buildings in areas of moderate or low seismicity, particularly in the eastern United States. The infill partitions often contain window openings. The experimental specimen (Figure 1-1) models one transverse frame of such a building.

1.2.1. Gravity Load Designed Frame

Without modern considerations for seismic loading, a typical GLD reinforced concrete frame may have highly variable lateral strength and behavior. The performance of GLD bare frames and joints has been studied extensively at Cornell University, with findings published in Pessiki et al. (1990), El-Attar et al. (1991a, 1991b, 1997) and Beres et al. (1992a, 1992b, 1996). The salient features of a typical GLD reinforced concrete frame (Figure 1-3) are:

1. Widely spaced confinement steel in columns.
2. Beam-column joints with no confining steel.
3. Positive moment (bottom) beam reinforcement discontinuous or poorly embedded within joints.
4. Column-to-beam moment capacity ratios that do not meet modern code provisions.
5. Column lap splices immediately above floor levels.
6. Construction joints above and below the beam-column joint.

All of these features have been incorporated into the design and construction of the model frame. For reference, Figure 1-4 presents interaction diagrams for a column section and a beam section in a negative moment region. The beam moment capacity neglects the additional capacity due to the overhanging portions of the floor slab, found to be only about 2.5% of the

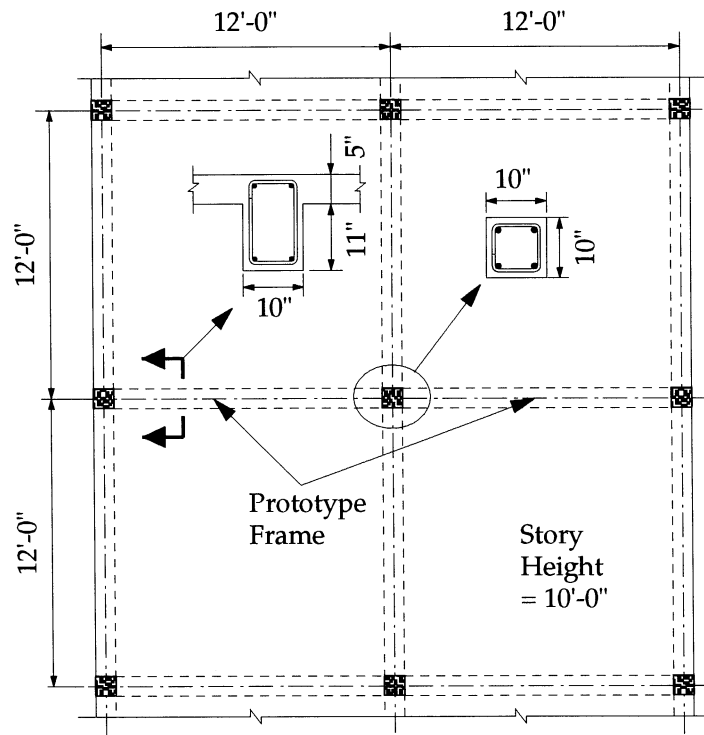


FIGURE 1-2 Plan of Prototype Structure

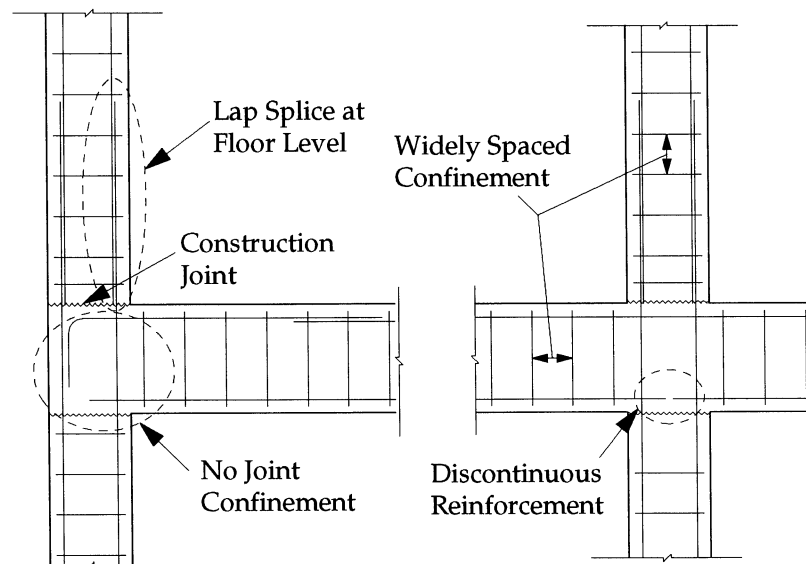


FIGURE 1-3 GLD Frame Features

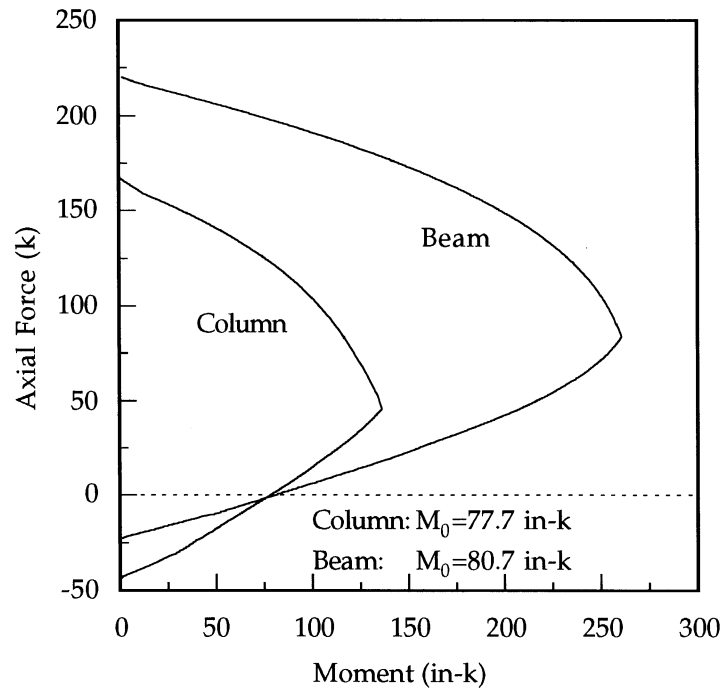


FIGURE 1-4 Interaction Diagrams

moment capacity at zero axial load, M_0 . Material testing results for the concrete and reinforcement are given in Section 2.2.

1.2.2. Unreinforced Masonry with Openings

The masonry infill was constructed from half-scale, two-cell concrete masonry units described in Section 2.3. The masonry was laid with face-shell mortaring by professional masons in a manner consistent with local practice. No shear connection, other than the plain mortar, was provided between the infill and frame. The infill was unreinforced and ungrouted, except surrounding the window openings, as indicated in Figure 1-1. The cells on all four sides of the windows were filled with mortar, and a bond beam formed with two lengths of 1/4" threaded rod in the three units immediately above the window. This reinforcement was required in the model structure to restrain the blocks from falling into the window opening. In a real structure such restraint would be provided by a window or door frame. Measured material properties for the masonry are given in Section 2.3.

1.2.3. Similitude Requirements

Reduced-scale models have been used widely for the study of infilled frames. Although well-proven techniques and methods for small-scale testing of reinforced concrete and masonry structures have been developed (Sabnis et al., 1983, Kim et al., 1988), full-scale or near-full-scale specimens allow for the use of standard materials and construction methods. Full-scale or near-full-scale specimens are particularly useful for masonry structures to provide a realistic representation of workmanship which can affect behavior. Due to practical constraints of the laboratory and available equipment, the specimen for this research was built at one-half scale. This scale allowed use of locally available materials for reinforcement and concrete aggregates. The masonry units were custom made, but the 4"x4"x8" nominal block size allowed standard installation by the masons.

The use of a scaled specimen requires certain considerations to relate the prototype and model properties (Sabnis et al., 1983). A general scale factor, S , relates model and prototype properties by

$$(model) = S \cdot (prototype). \quad (1.1)$$

A half-scale model uses a length scale factor, $S_l = 1/2$, from which the scale factors of other important quantities may be derived (Table 1-1). The constitutive behavior of the prototype and model materials are assumed to be equal, thus the modulus scale factor $S_E = 1$.

TABLE 1-1 Scale Factors for Pseudodynamic Testing

Quantity	Scale Factor
Length	S_l
Time	$\sqrt{S_l}$
Velocity	$\sqrt{S_l}$
Acceleration	1
Mass	S_l^2
Force	S_l^2
Frequency	$1/\sqrt{S_l}$
Strain	1
Stress	1

1.2.4. Input Ground Motion

For multi-degree of freedom (MDOF) systems, pseudodynamic testing allows realistic simulation of story forces, with no assumptions of load distribution necessary. However, a pseudodynamic test uses a single, specific ground input motion, which may be an actual or synthetic record. The Taft-Lincoln School S69E record of the event at Kern County, California on July 20, 1952 was selected as the ground motion for this series of PSD tests. A normalized accelerogram for this record appears as Figure 1-5. Hereafter, "Taft 0.10g" will refer to this record scaled to a peak ground acceleration (pga) of 0.10g; and likewise for other pga levels. In Figure 1-5, the upper time scale gives real time, while the lower scale gives time compressed by the factor $\sqrt{1/2}$ used for the half-scale PSD tests. The original accelerogram was discretized in real time at $\Delta t = 0.01$ sec. To meet the numerical stability criterion for the explicit integration (see Section 5.2), linear interpolation was applied to reduce the discretization to $\Delta t = 0.005$ sec. Finally, application of the scale factor results in a compressed time step, $\Delta t \approx 0.0035$ sec. Hereafter, all times cited will refer to the compressed time scale.

Figure 1-6 shows the Taft 1.0g response spectrum. The vertical lines indicate the periods of the fundamental mode for the undamaged infilled frame and the bare frame. As the trend of the spectrum rises within this window, damage caused to the infilled frame will increase the fundamental period and increase the seismic demand on the structure. The Taft record also was selected to allow comparisons to other shake table and PSD testing at Cornell University (El-Attar et al., 1991a, 1991b; Mosalam, 1996; Abdel-Mouti, 1997).

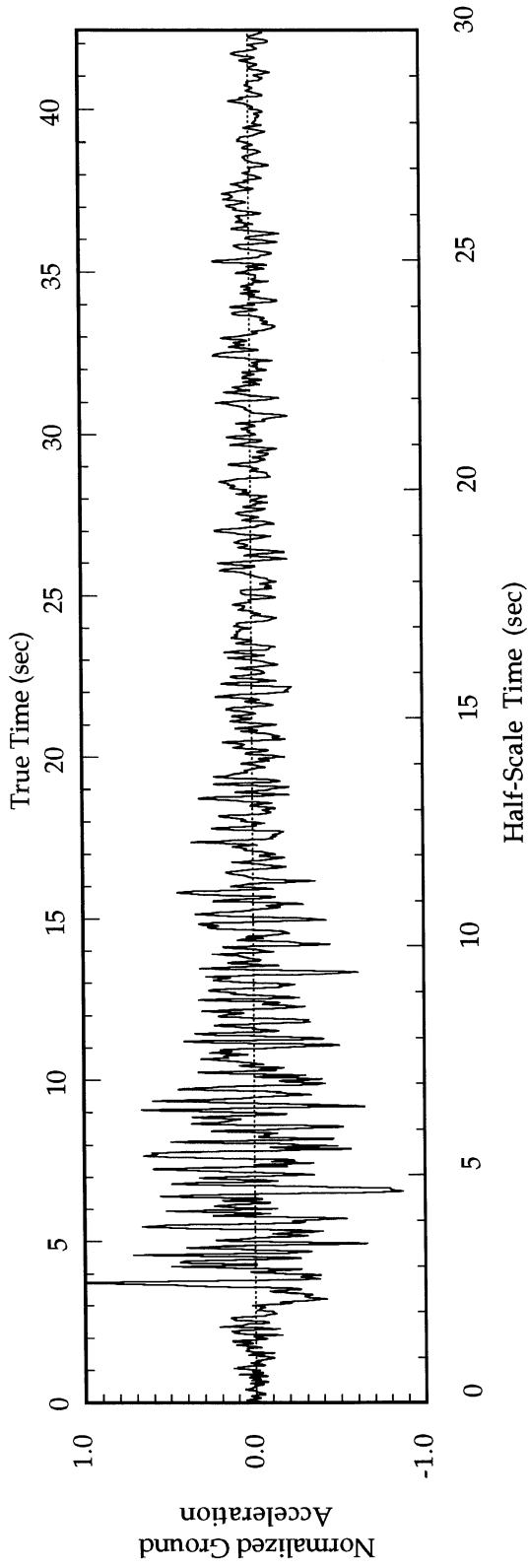


FIGURE 1-5 Taft 1.0g Accelerogram

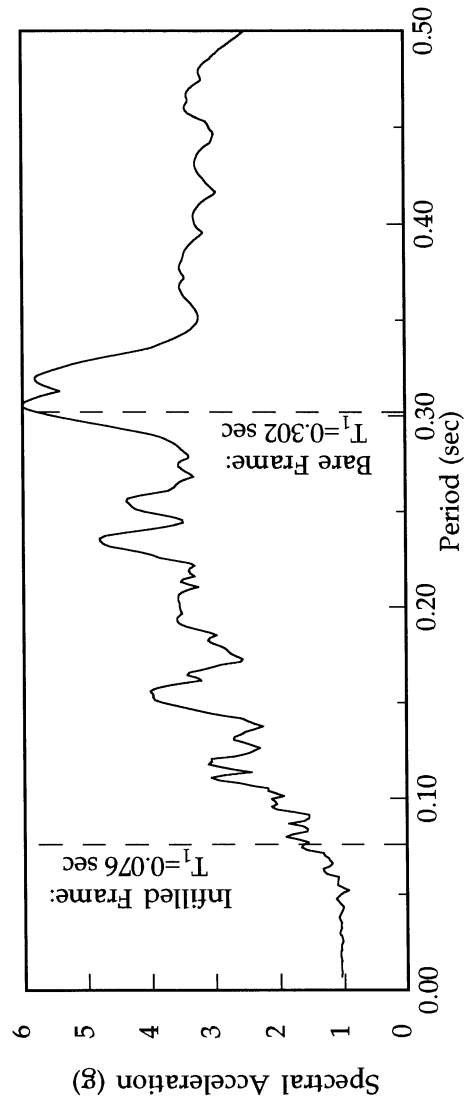


FIGURE 1-6 Taft 1.0g Response Spectrum

1.3. Behavior of Masonry Infilled Frames

1.3.1. Failure Modes

The masonry infill itself may fail in a wide variety of modes, most often involving some combination of bed joint sliding, corner crushing and diagonal cracking. Figure 1-7 shows five failure modes identified by Mehrabi et al. (1996) as commonly occurring. The exact mode of failure depends upon material properties—such as compressive strength, shear strength and coefficient of friction; geometric constraints—such as frame-wall interface gaps, window openings or shear connectors; and other characteristics—such as workmanship.

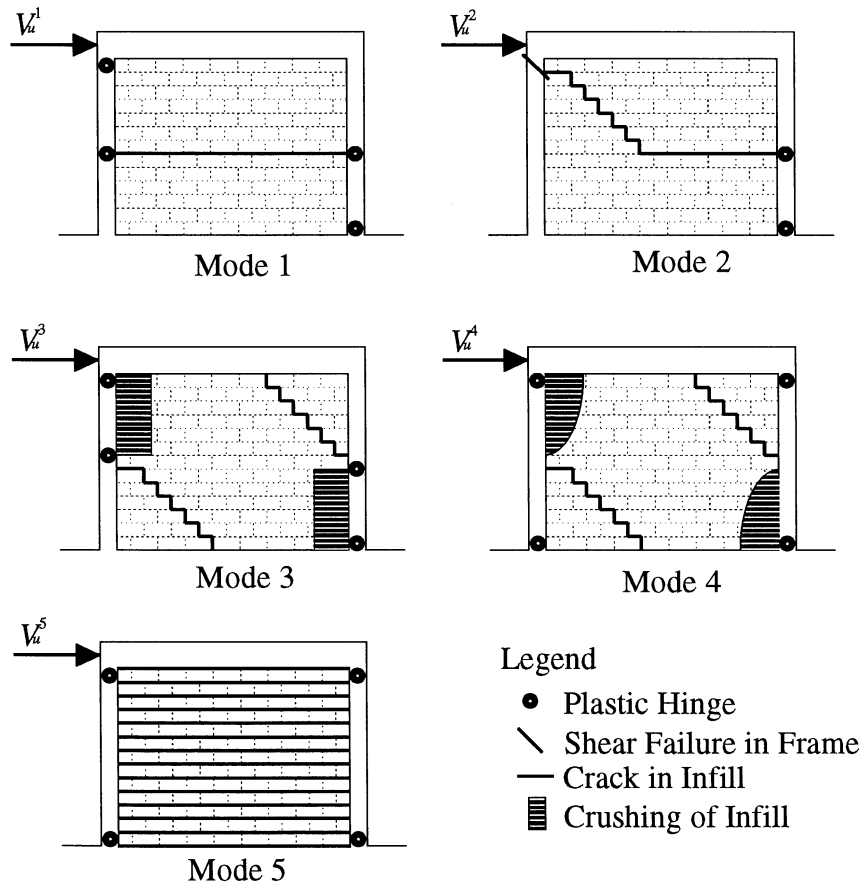


FIGURE 1-7 Infilled Frame Failure Modes (after Mehrabi et al., 1994)

The failure mode of the masonry is of particular concern as the masonry can apply large local forces to the bounding frame, often in regions not designed for these forces. The most prevalent example of unintended frame failure caused by infill interaction is the “short column” effect, common in half-height infills but also occurring in full infills. Masonry failure over part of the panel height removes lateral restraint provided by the masonry to the column, resulting in significant moments near mid-height of the column, normally considered a low-moment region. The “short column” refers to this unrestrained length of column. In the worst case, for a given column moment capacity, plastic hinging at mid-height of the column increases the lateral shear demand by a factor of two. But even below the moment capacity, the increased shear forces in the column may produce premature shear failure. The non-ductile behavior of GLD frames may also be heightened by local force and deformation demands imposed by the deteriorating masonry.

1.3.2. Previous Research

The complex interaction of frame and infill has been the subject of numerous experimental programs and recently many advanced finite element model analyses. A brief review of previous research focuses primarily on experimental work and especially that which has addressed the effects of openings, GLD frames and multi-panel specimens.

Early experiments performed by Wood (1958) used full-scale, single-bay, concrete-encased steel frames infilled with brick and clay block. A test with a door opening showed an ultimate load of about twice that of the frame alone but about a third less than a fully infilled specimen. Benjamin and Williams (1958) tested both steel and concrete single bay frames infilled with brick. Specimens from 1/3 to full-scale were subjected to monotonic loading, including one specimen with a window opening. Empirical formulas to predict lateral strength were developed using normal stress-shear stress interaction from couplet tests. Sachanski (1960) also performed experiments at full and reduced scale on concrete frames with masonry infill, both with and without openings. In addition, he developed expressions for ultimate load and deflection based on classical, plane stress elasticity.

Holmes (1961) first proposed the concept of an equivalent compressive strut based on a series of small and full-scale steel frames infilled with both concrete and masonry. The first group of tests subjected single panel specimens to monotonic racking (horizontal) loads only, but a second group of tests (Holmes, 1963) considered both horizontal and vertical loads, as well as including a two-story specimen.

The work of Stafford-Smith (1962, 1966, 1967, 1968) established the equivalent compressive strut as a practical method for prediction of the lateral strength and stiffness of multi-story infilled frame structures. Extensive experimentation on small-scale frames infilled with mortar, including one-, two- and three-story specimens, resulted in a series of empirical relations used to determine equivalent strut properties from basic dimensions and material properties of the frame and infill. A group of experimentally derived curves allow estimation of strut width from contact length. Contact length between frame and infill is expressed as a function of the relative stiffnesses of frame and infill, based on beam-on-elastic-foundation theory. These relations developed by Stafford-Smith still form the basis for current, recommended analyses of infilled frames in such texts as Drysdale et al. (1994).

Typical full-scale frames infilled with brick or block usually have lower relative stiffnesses than those of the small-scale frames infilled with mortar tested by Stafford-Smith, thus limiting the application of the empirical relations for real building structures. Later researchers, including Mainstone (1971) and Hendry (1990), proposed other relations between contact length and strut width. Mainstone (1971) performed a group of parallel small-scale and full size experiments with infills of microconcrete, model and real bricks and found wide variation of behavior even within nominally identical specimens. Specimens which used scaled or full-size masonry as opposed to the more homogeneous microconcrete, showed a tendency for crack initiation along masonry bed joints prior to any crushing of the infill.

Further, Stafford-Smith's experiments used solid mortar infill, not individual masonry units bedded in mortar, and always failed under diagonal compression—either corner crushing or diagonal cracking. Masonry, especially unreinforced masonry, may often contain significant weak shear planes along the bed joints, which may initiate failure prior to diagonal compression failures, as noted by Mainstone (1971). The significance of masonry shear and tensile bond strengths to the overall behavior of infilled frames was studied in detail by Dhanasekar and Page (1986) through finite element models and companion experiments. Sliding shear failures cause excessive local forces on the bounding frame and may induce sudden column shear failure in concrete frames. Further, cyclic loading rapidly degrades the shear-friction resistance of the infill, leaving "short columns" as the primary lateral resisting mechanism (Paulay and Priestley, 1992). In new construction reinforcement and grouting of the masonry cells could alleviate this problem, although many walls included for architectural reasons only often remain ungrouted and unreinforced. In assessment of unreinforced masonry, bed joint shear failure must be a prime consideration.

Other significant experimental programs during the 1960's were conducted by Mallick and Severn (1967) to verify the possibilities of early finite element

analysis as a predictive model, and by Mallick and Severn (1968) to characterize dynamic properties of infilled frames. Mallick and Garg (1971) conducted a substantial study on the effects of openings and boundary shear connectors using small-scale, mortar-filled frames and verified results with finite element models. To maximize strength of the infilled frame, they recommend locating door and window openings outside the main diagonal area, thus avoiding disturbance of the main diagonal compressive strut.

During the 1980's Liauw and Kwan greatly advanced the use of finite element models, with companion experiments, as a tool for understanding the behavior of infilled frames. By introducing plasticity models for the infill and interface elements between frame and infill, Liauw and Kwan (1983a) identified new frame failure modes. Crushing or softening of infill regions of high compressive stress, at the ends of a main diagonal strut, may significantly reduce lateral support to the column provided by the infill, resulting in a "short column" effect. Although the resultant plastic hinging in the frame may appear similar to that caused by bed joint sliding failures, the hinging due to infill plasticity must be considered a distinct failure mode and will occur at a different ultimate load than for the joint sliding failure. In the finite element modeling of Liauw and Kwan (1982), no interface elements were used within the infill and therefore joint sliding could not be reproduced. In the scale model experiments only microconcrete was used, no discrete masonry units. Plasticity-induced frame effects are a significant concern for infills of both reinforced concrete or masonry, but with unreinforced masonry infills, bed joint sliding failures may occur at a lower load and must not be neglected.

Cyclic testing of masonry infilled specimens began during the 1970's with research addressing seismic performance for both evaluation and retrofit. Experimental programs have been conducted by Klingner and Bertero (1976), Kahn and Hanson (1979), Brokken and Bertero (1983) and Liauw and Kwan (1985). Dawe et al. (1989) tested scale model infill panels under sinusoidal base excitation. Dawe and Seah (1989) also summarize an extensive experimental program of full size infilled steel frames performed at the University of New Brunswick. A total of twenty-eight specimens, tested monotonically, examined the effects of various characteristics including door openings, truss-type bed joint reinforcement and infill-frame interface conditions.

Much research has focused on single-story specimens, and extrapolation to multi-story, multi-bay specimens is not straightforward due to different boundary conditions. As shown by Paulay and Priestley (1992), multi-story frames typically impose a ductility demand in the lowest story in excess of its capacity. Such behavior has been observed in reduced-scale experiments by Harris et al. (1993) on three story models under monotonic, triangular

loading. All failures occurred in the lowest story, with significant bed joint sliding and failure in the columns.

A substantial program has been carried out by Zarnic and Tomazevic (1984, 1985); also reported in Zarnic (1994a, 1994b). Cyclic tests were performed on one-half and one-third scale reinforced concrete frames infilled with brick and block. Both unreinforced and reinforced infills were tested, as well as panels with window and door openings. Results have been used to propose some innovative nonlinear strut models, including multiple strut schemes for panels with openings. Other recent European research includes cyclic testing by Pires and Carvalho (1992), shake table testing of a three-story reduced-scale specimen by San Bartolomé (1992) and pseudodynamic testing of two-story full and reduced scale specimens by Scaletti et al. (1992).

In the United States, the most recent generation of experimental research has been well documented in Angel et al. (1994) which tabulates eleven then-current experimental programs at several universities and engineering firms within the United States. The projects include various combinations of concrete or steel frames and brick, block or clay tile infill tested at full and reduced scales under monotonic, cyclic and some PSD loading. The most extensive programs have been by Angel et al. (1994) with cyclic testing of full-scale, single-bay, single-story reinforced concrete frames infilled with brick and block. Mehrabi et al. (1994) tested a group of half-scale, single-bay, single-story specimens infilled with both hollow and solid block. The reinforced concrete bounding frames included specimens with both modern seismic detailing and non-ductile (GLD) detailing.

Previous research at Cornell University has focused on unreinforced infill at one-fourth scale with steel bounding frames. Testing has included quasistatic loading of single-story, two-bay specimens with solid panels (Zawilinski, 1994), and similar specimens with door and window openings (Mosalam, 1996). A quarter-scale, two-story, two-bay specimen with second story window openings has been tested pseudodynamically (Mosalam, 1996). Most recently, shake table testing was performed on a two-frame, quarter-scale, two-story, two-bay specimen with second story window openings (Abdel-Mouti, 1997). The half-scale experimental specimen of the present research was modeled after the same prototype used for this quarter-scale test to allow future comparative study of PSD and shake table test results.

SECTION 2 MATERIALS

2.1. Mix Design

In order to approximate the strength of concrete typical of older construction in the half-scale model, a target 28-day compressive cylinder strength in the range of 4000 to 4500 psi was selected. Similar concrete strengths have been used for previous scale-model frame specimens at Cornell University (El-Attar et al. 1991a, 1991b, 1997). Two other important criteria in the mix design were small aggregate size and good workability. Coarse aggregate with a nominal maximum size of 3/8" was used to approximate at half-scale typical concrete aggregate of about 3/4" size. The reinforcement cover of about 1/2" necessitated the use of aggregate limited to 3/8" top size. Good workability was required to achieve proper consolidation due to potentially difficult placement of the concrete into small column cross-sections with little reinforcement cover. The 5"x5" columns had about a 3.5" wide clear opening in the center, and the 50" height had to be poured in a single lift. Initial trial mix design followed the guidelines of "Standard Practice for Selecting Proportions for Normal, Heavyweight, and Mass Concrete" (ACI 211.1-91). Details of the results of the mix design process appear in Buonopane (1997). The final mix proportions are given in Table 2-1.

TABLE 2-1 Final Mix Proportions

w/c=0.70	lbs/CY	% by weight
Water	388	0.11
Cement	554	0.15
FA	1189	0.33
CA	1500	0.41

WRA: 0.75 ml/lb cement

2.2. Concrete and Steel Properties

Compressive cylinder and split cylinder tests were performed on cylinders cast from each pour of the concrete frame. Tables 2-2 and 2-3 give the results of the 28-day tests. Tables 2-4 and 2-5 give the results of 15-month tests conducted during the pseudodynamic testing phase to assess the actual strength of the frame concrete. Figure 2-1 compares sample stress-strain curves from 28-day and 15-month cylinder tests. The average concrete strength and modulus from the compression tests will be used to define the Todeschini stress-strain model, allowing calculation of moments and axial

forces in the concrete members from strain gages mounted on the reinforcing steel. Further details on the concrete testing appear in Buonopane (1997).

TABLE 2-2 28-day Cylinder Test Summary

8 samples	f'_c (psi)	E_c (ksi)
Average	4437	3178
COV (%)	7.56	33.77

TABLE 2-3 28-day Split Cylinder Test Summary

8 samples	f'_{ct} (psi)	$f'_{ct}/\sqrt{f'_c}$
Average	520	7.8
COV (%)	6.97	--

TABLE 2-4 15-month Cylinder Test Summary

13 samples	f'_c (psi)	E_c (ksi)
Average	5796	3758
COV (%)	6.43	28.93

TABLE 2-5 15-month Split Cylinder Test Summary

11 samples	f'_{ct} (psi)	$f'_{ct}/\sqrt{f'_c}$
Average	516	6.7
COV (%)	15.75	--

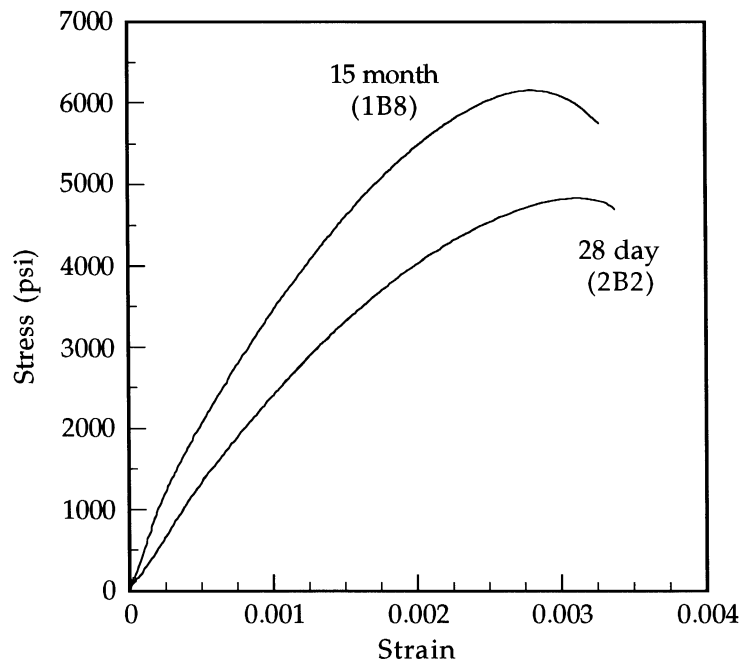


FIGURE 2-1 Typical Cylinder Stress-Strain Curves

The four different types of reinforcing steel used in the concrete frame were tested in tension to determine yield stress and elastic modulus. For each bar type, three tensile specimens were tested, the results summarized in Table 2-6. Representative stress-strain curves for a #4 and #2 deformed bar are shown in Figure 2-2. The 1/4" plain bars exhibited an elastic range and yield plateau but only slight strain hardening before fracture. The #2 deformed bars behaved as a higher strength structural steel might, with no distinct yield point or plateau, but a gradual strain hardening to fracture.

TABLE 2-6 Average Steel Properties

Bar	Yield Stress (ksi)	Modulus (ksi)
#4 Def'd.	54.5	29272
#3 Def'd.	51.8	30176
#2 Def'd.	68.1	31420
#2 Plain	44.2	29726

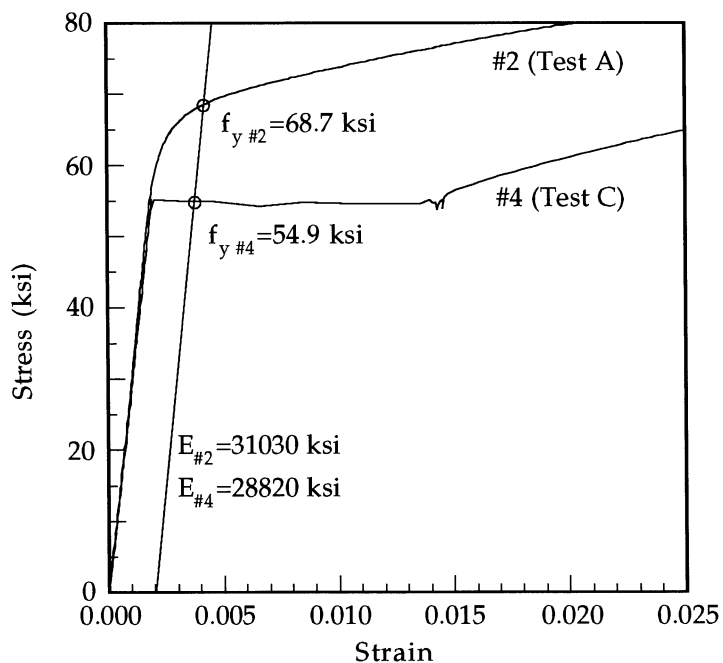
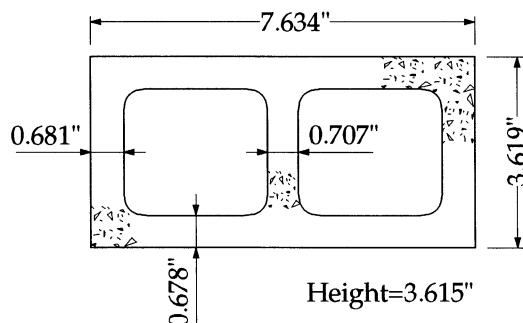


FIGURE 2-2 Typical Reinforcement Stress-Strain Curves

2.3. Masonry Testing

The two-cell concrete masonry units (CMUs) used in construction of the infill were intended as half-scale models of a typical 8"x16" CMU. The CMU were originally cast by Valley Block Co. of Loveland, Colorado for research by Mehrabi et al. (1996). Figure 2-3 and Table 2-7 give average physical dimensions measured from twelve blocks. Compression tests were conducted on single blocks, mortar cylinders (2"x4", Type S) and three course prisms according to the appropriate ASTM specifications. Results from these tests are summarized in Tables 2-8 to 2-11. Figure 2-4 shows a representative single block stress-strain curve, along with representative curves for mortar cylinders and masonry prisms. Shear strength of the masonry was determined using six square panel assemblages tested according to ASTM E519-81. The average shear properties appear in Table 2-12. See Buonopane (1997) for further details of the masonry tests.



Average measured dimensions
from 12 blocks.

FIGURE 2-3 Average CMU Dimensions

TABLE 2-7 CMU Physical Properties

Equiv. Thickness	in	1.910
Ambient Weight	lbs	2.80
Density	lb/ft ³	90.4
Gross Area	in ²	27.63
Net Area	in ²	14.58
Ave. Net Area	%	52.8
Mortared Area	in ²	10.61

TABLE 2-8 Masonry Block Compressive Properties

12 samples	f_m (psi)	E_m (ksi)
Average	2337	1220
COV (%)	16.1	40.3

TABLE 2-9 Mortar Cylinder Compressive Properties

15 samples	f'_c (psi)	E_c (ksi)
Average	2014	1837
COV (%)	21.4	43.3

TABLE 2-10 Mortar Split Cylinder Properties

15 samples	f'_{ct} (psi)	$f'_{ct}/\sqrt{f'_c}$
Average	263	5.86
COV (%)	14.4	

TABLE 2-11 Masonry Prism Properties

14 samples	f_m (psi)	E_m (ksi)
Average	1473	1095
COV (%)	12.5	16.1

TABLE 2-12 Masonry Shear Properties

6 samples	Shear Strength psi	Peak Shear Strain $\times 10^{-6}$	Shear Modulus ksi
Average	111	576	195
COV(%)	8.7	11.7	11.8

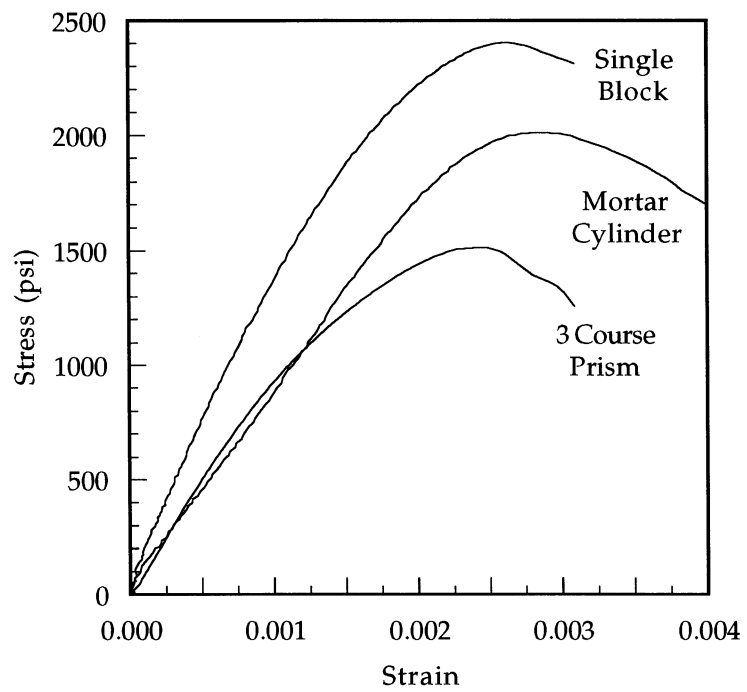


FIGURE 2-4 Typical Masonry Stress-Strain Curves

SECTION 3 EXPERIMENTAL SET-UP

3.1. Loading System

An important consideration in design of the load system was the ability to apply fully reversing (both east and west) displacements to the structure through a connection mechanism which would not interfere with the behavior of the concrete frame itself. A single, rigid connection at the center column joints of each story would have required heavy reinforcement at the connection point to prevent local failure, thereby unrealistically altering behavior of the joint. The devised loading system allows for fully reversing loading of the structure through bearing (compression-only) connections at either end of the story beams. With bearing connections at each end of the beams, the beam stubs must carry compressive loads only, and therefore no longitudinal reinforcement need connect the stubs to the main beams, producing an unaltered reinforcement pattern in the joint (see Figure 1-1). A 1/2" steel bearing plate is mounted on the face of each stub with cast-in-place embedded screw anchors and seated with high-strength gypsum. Load is applied through a high-strength, high-hardness 3/4" diameter tungsten-carbide ball bearing. The ball bearing seats between greased conical depressions in the two steel loading plates, thus minimizing rotational restraint of the exterior beam-column joint.

One 55 k capacity, ± 3 in stroke hydraulic actuator at each story level controlled displacement of the specimen. Two 55 k capacity load cells are positioned in the load system as shown in Figure 3-1. Two displacement transducers (DCDTs) mounted on an external reference frame measured the story displacements at the center of the interior beam-column joints. An additional DCDT mounted on the same reference frame measured the displacement at the top of the base beam, which was later subtracted from the story measurements to give true story displacements. Complete details on the hydraulic control system and data acquisition system appear in Buonopane (1997).

3.2. Strain Gages

A total of eighty strain gages were applied to the reinforcing steel prior to casting of the concrete. Column gages were located about 1 1/2" from each end to avoid interference with shear reinforcement, and at mid-height. Beam gages were installed adjacent to the center joint on the eastern beams only. The locations of the gages on the south face (S00-S39) are shown in Figure 3-2, with a parallel set placed on the north face reinforcing steel. Proper surface preparation of the reinforcing steel required removal of some bar ribs with an electric grinder prior to bonding, and gages were protected with a rubber

coating for waterproofing and wax coating for protection from physical damage during the placing of concrete. Strain gage delta rosettes were applied at six locations on the face of the masonry as shown in Figure 3-2 to measure principal strains and directions.

3.3. Displacement Transducers

A total of twenty-eight displacement transducers (DCDTs) were installed on the specimen—twenty to measure total strain across large portions of the masonry panels or across window openings, and eight to measure interface gap openings at panel corners. Figure 3-3 shows main diagonal DCDTs installed on the north face of the wall. DCDTs installed on the south face, shown in Figure 3-4, include those along off-diagonals, across window openings and across frame-wall interfaces (DT30-DT37).

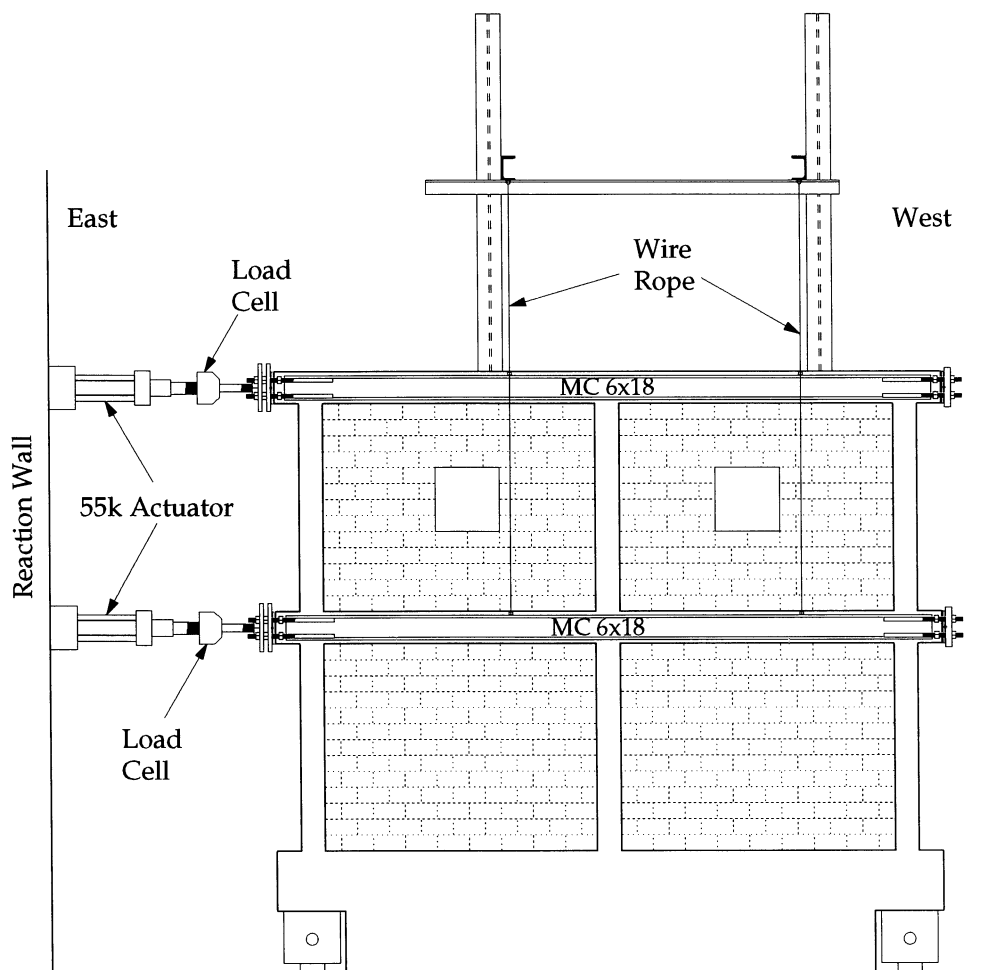


FIGURE 3-1 Loading System Elevation

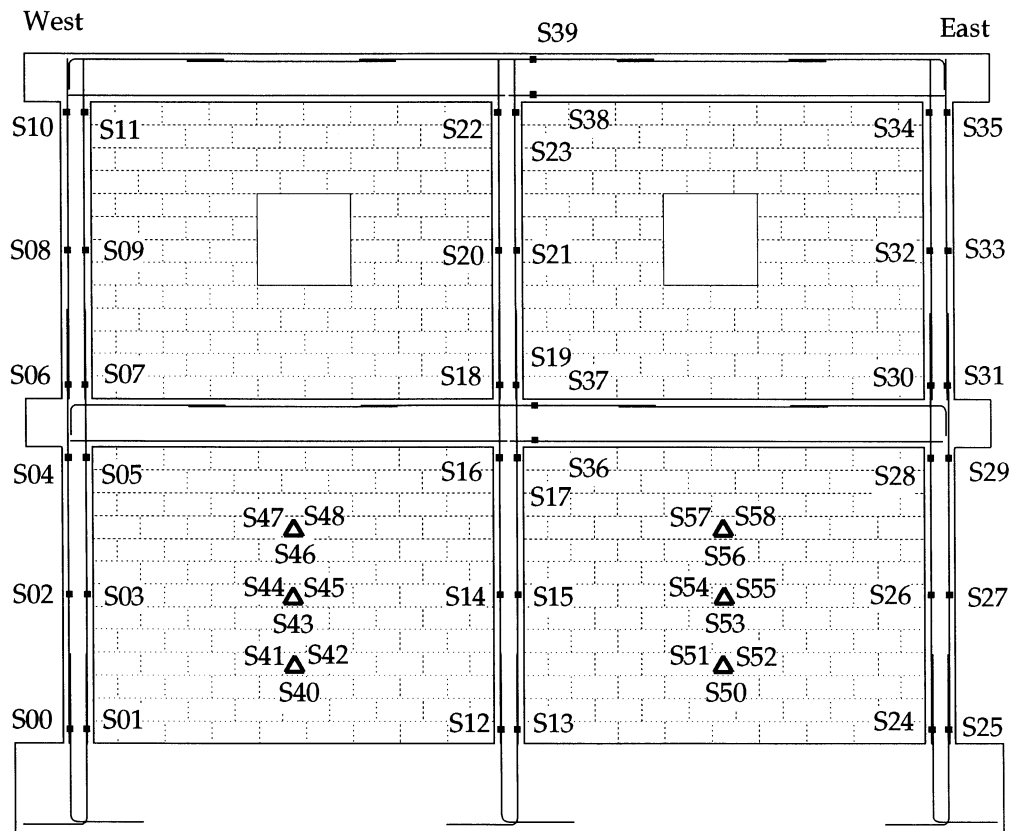


FIGURE 3-2 Strain Gage Locations—South Face

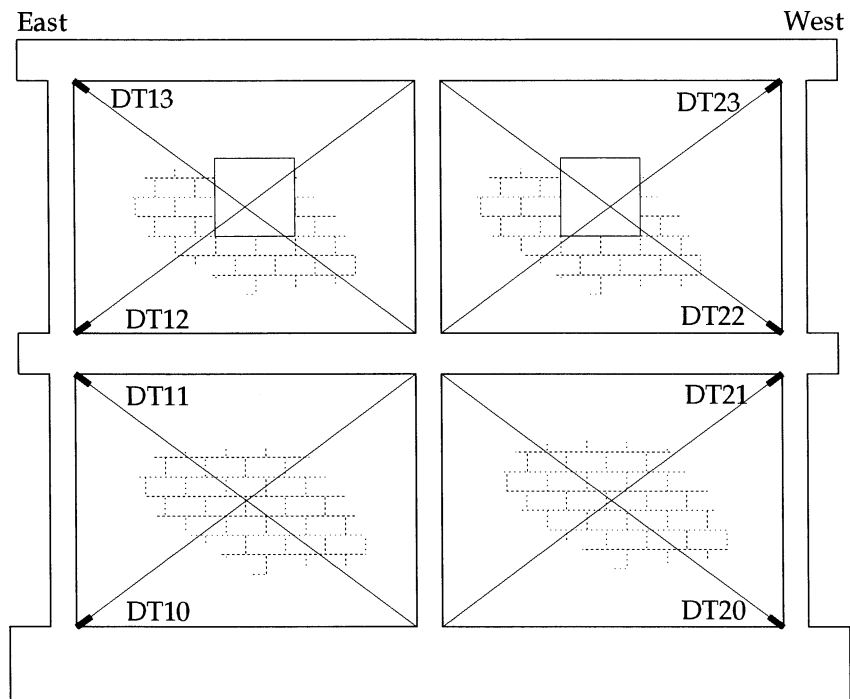


FIGURE 3-3 Displacement Transducers—North Face

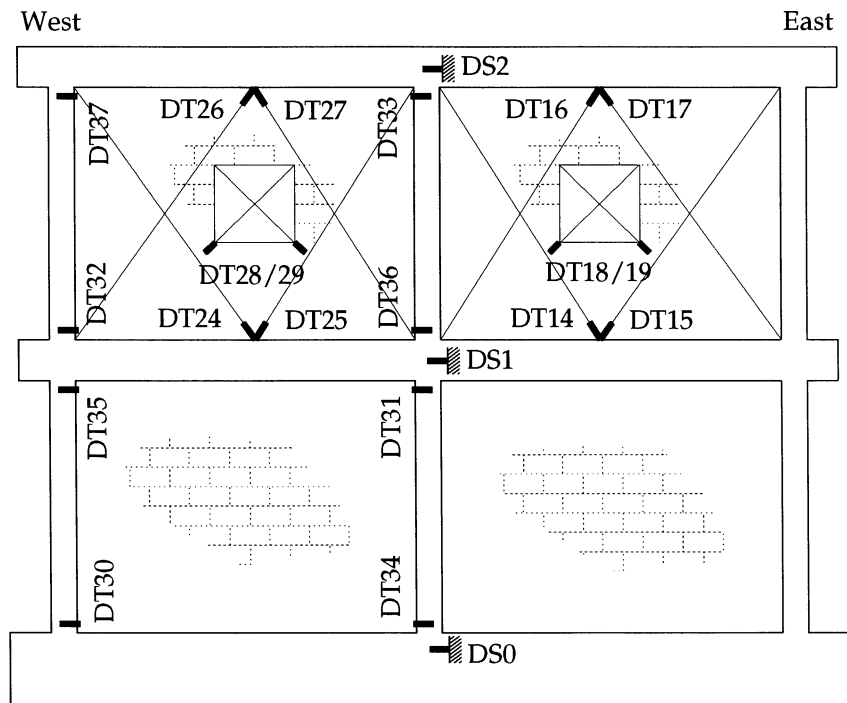


FIGURE 3-4 Displacement Transducers—South Face

SECTION 4 SPECIMEN CHARACTERIZATION

Preliminary testing serves to verify proper functioning of the loading system and all instrumentation and to characterize structural properties of the specimen, such as stiffness and damping. This testing measures properties required for the pseudodynamic algorithm and provides data for calibration of analytical models under simple, controlled loading conditions.

4.1. Bare Frame

4.1.1. Free Vibration Testing

Modal frequencies and damping ratios are determined from free vibration testing. Accelerometers were mounted on the beam stubs at one end of the frame and a small impact imparted to the frame from the opposite end. For the bare frame tests, the accelerometers were sampled 1024 times at a rate of 160 per second, allowing for frequency spectrum information up to 80 Hz with a resolution of about 0.16 Hz. A typical normalized acceleration time history and associated frequency spectrum are shown in Figure 4-1. The frequency spectrum clearly identifies two modes of vibration near 12 Hz and 36 Hz. These results are from first story accelerations due to a first story impact, although nearly identical results were obtained from accelerations of either story resulting from impact at either story. Only the relative magnitudes of the spectral peaks differed with changing impact or analysis story.

The acceleration decay over time in a free vibration test provides a good measure of the natural damping, which is present in the structure even with no damage or structural nonlinearity. In most cases the force provided by this natural damping is idealized as proportional to velocity for mathematical convenience, and thus the damping often termed viscous damping. The free vibration motions are of extremely small magnitude and thereby minimize the contributions of other damping mechanisms. The rate of decay of the acceleration envelope defines the damping ratio of the structure in each mode. However, for multi-degree of freedom (MDOF) systems, the total acceleration time history (as in Figure 4-1) must first be decomposed into its pure modal time histories. Here, the composite acceleration signal was filtered through a fifth-order butterworth filter in the MATLAB (1993) numerical software. Bandpass filtering with a semibandwidth of 5 Hz centered about each modal frequency was used. The resultant filtered time histories appear in Figure 4-2. The peaks of the modal acceleration signal are fitted with an exponential decay curve of the form

$$a(t) = a_0 e^{-\zeta\omega(t-t_0)} \quad (4.1)$$

where ζ is the modal damping ratio, ω the circular frequency and t_0 the time of the initial peak. The results of this test gave damping ratios of 1.36% and 1.00% for the first and second modes, respectively. Other free vibration tests on the bare frame gave very similar viscous damping ratios.

One unexpected result of the free vibration tests was the presence of a second mode peak in the frequency spectrum higher than that of the first mode. As mentioned, the relative magnitudes of the peaks varied with impact and analysis story, but almost always the second mode peak was the greater. To verify these results, free vibration tests were simulated numerically using the stiffness matrix of Eq. (4.3) and mass matrix of Eq. (4.5). The free vibration simulations showed similar results to the actual tests, the modal peaks occurring at 10.9 Hz and 27.6 Hz and the second mode having a greater peak in the frequency spectrum. Details of the numerical analysis appear in Buonopane (1997).

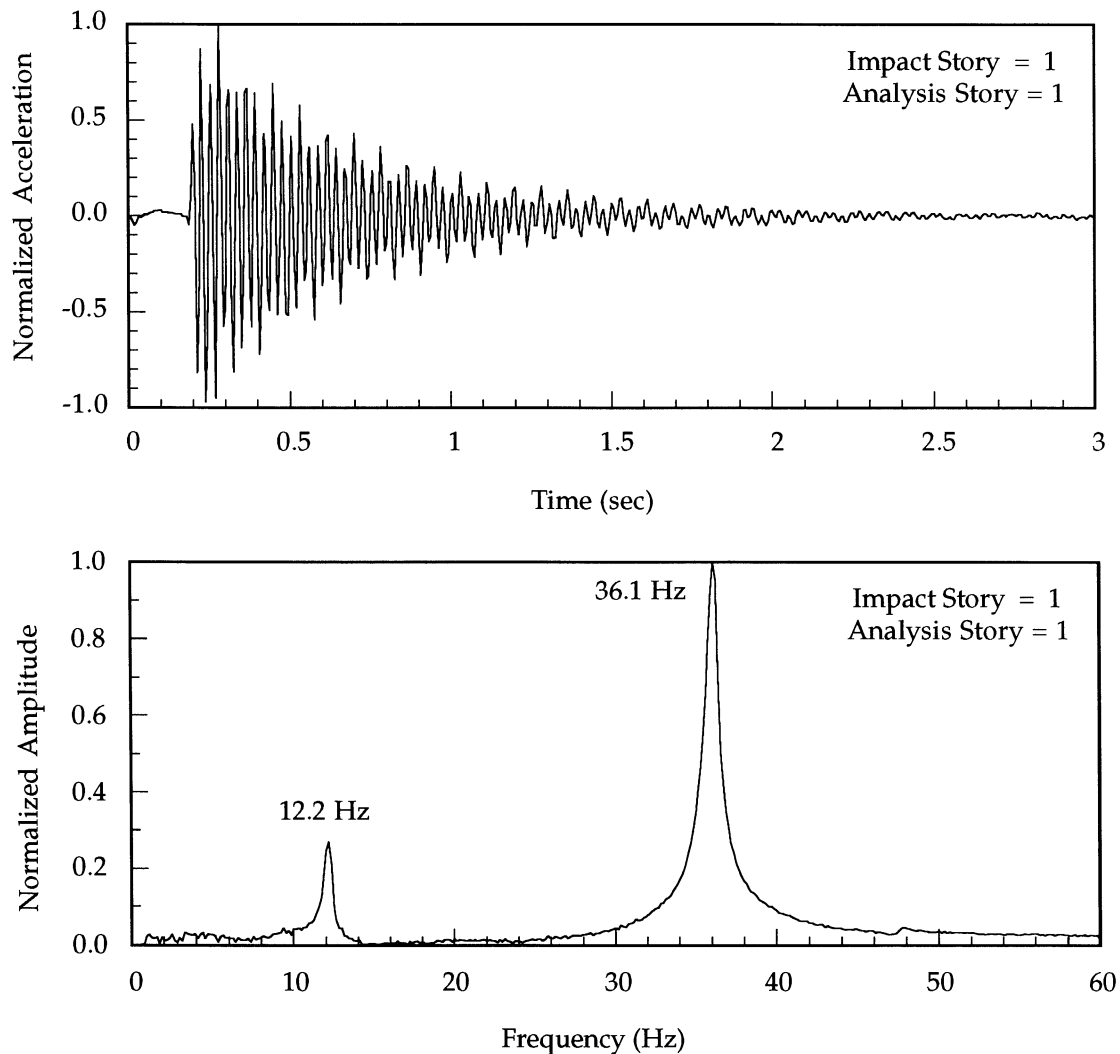


FIGURE 4-1 Bare Frame Free Vibration Test

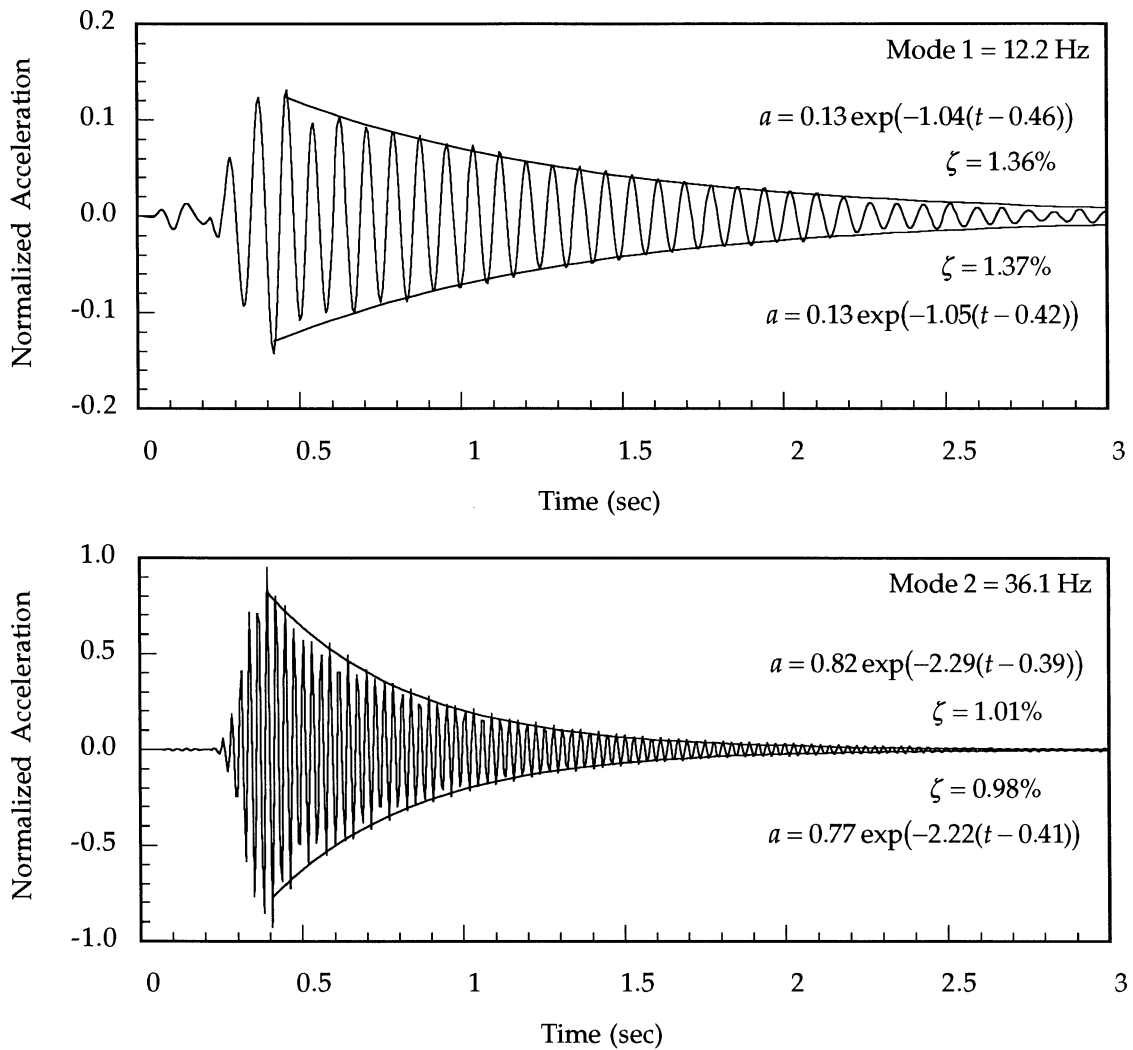


FIGURE 4-2 Bare Frame Free Vibration Modal Response

4.1.2. Flexibility Testing

One translational degree of freedom (DOF) is assigned at each story of the experimental specimen. The 2x2 lateral stiffness matrix of the bare frame was determined by static flexibility testing, with lateral load applied at a single DOF while displacements at all DOFs are measured. Applied load was measured with a load cell at the jack and story displacements calculated from the average readings of dial gages placed at the east and west ends of the structure. The assembled flexibility matrix was found to be

$$\mathbf{F}_{bare} = \begin{bmatrix} 0.0357 & 0.0393 \\ 0.0415 & 0.0828 \end{bmatrix} \text{ in/k.} \quad (4.2)$$

Averaging the off-diagonal terms and inverting, gives the stiffness matrix

$$\mathbf{K}_{bare} = \begin{bmatrix} 62.7 & -30.7 \\ -30.7 & 27.0 \end{bmatrix} \text{ k/in.} \quad (4.3)$$

The experimental stiffness matrix may be verified with a beam element frame model assuming elastic behavior. Using centerline dimensions, elastic transformed moments of inertia (uncracked), and a concrete modulus, $E_c = 3178$ ksi, from the 28-day cylinder tests (Table 2-2), results in the analytical stiffness matrix

$$\mathbf{K}_{analytical} = \begin{bmatrix} 84.0 & -35.4 \\ -35.4 & 31.4 \end{bmatrix} \text{ k/in.} \quad (4.4)$$

The first term of $\mathbf{K}_{analytical}$ is about 1.33 times greater than the corresponding term in \mathbf{K}_{bare} , while the three remaining three terms are all about 1.15 times greater. At the time of bare frame testing, the ages of the four concrete pours ranged from 18 to 44 days, and thus the elastic moduli of the frame members may have varied significantly from the 28-day cylinder test average. However, the near-scalar relationship between the two stiffness matrices suggests that they should have similar eigenvalues, and thus modal frequencies.

To determine modal frequencies, the mass matrix of the bare frame is estimated as

$$\mathbf{M}_{bare} = \begin{bmatrix} 2.27 & 0 \\ 0 & 1.86 \end{bmatrix} \times 10^{-3} \text{ k - sec}^2/\text{in.} \quad (4.5)$$

The first story term includes mass of the beam and half the height of columns on each story; the second story, the beam and half the height of the second story columns only. Based on the mass and stiffness matrices, modal frequencies are found from the eigenvalues. Modal frequencies determined from various methods are presented in Table 4-1; all compare favorably.

TABLE 4-1 Bare Frame Characteristics

	Flexibility Test	Analytical	Free Vibe Test
Stiffness (k/in)	$\begin{bmatrix} 62.7 & -30.7 \\ -30.7 & 27.0 \end{bmatrix}$	$\begin{bmatrix} 84.0 & -35.4 \\ -35.4 & 31.4 \end{bmatrix}$	--
f_1 (Hz)	11.0	12.7	12.2
f_2 (Hz)	30.8	33.0	36.1

4.2. Infilled Frame

4.2.1. Free Vibration Testing

Free vibration tests of the infilled frame were performed at a sampling rate of 480 per second over 1024 samples, giving frequency information up to 240 Hz at a resolution of 0.47 Hz. The higher sampling rate was necessary to capture the second mode response expected around 140 Hz. A typical time history and frequency spectrum are given in Figure 4-3. In the frequency spectrum, only the first mode is distinguishable around 44 Hz. The small amplitudes of the second mode vibration may have been below the acceleration resolution limit of the accelerometers, and thus no second mode peak appears in the spectrum. All tests performed gave similar results with damping ratios in the range of 2.00% to 2.15% based on the decay curve of the filtered, first-mode acceleration time history.

In order to estimate the damping of the second mode, numerical simulations of the free vibration tests on the infilled wall were also performed. Simulations were run for several damping ratios between 1% and 10%, all of which exhibited a prominent second mode peak, unlike the actual free vibration test. Second mode damping of 5% produced time histories with a good qualitative match to the true free vibration test, and 5% damping was used for the pseudodynamic algorithm.

4.2.2. Flexibility Testing

A static flexibility test was performed on the infilled frame, subjecting it to three complete low-level displacement cycles. As for the bare frame, each story DOF was displaced with the other story unrestrained. Figure 4-4 shows the flexibility plots for the complete test. A best fit line on each set of data gives the flexibility matrix as

$$\mathbf{F} = \begin{bmatrix} 0.00153 & 0.00265 \\ 0.00204 & 0.00520 \end{bmatrix} \text{in/k.} \quad (4.6)$$

The assembled flexibility matrix inverted with off-diagonal terms averaged, gives the stiffness matrix

$$\mathbf{K} = \begin{bmatrix} 2116 & -954 \\ -954 & 623 \end{bmatrix} \text{k/in.} \quad (4.7)$$

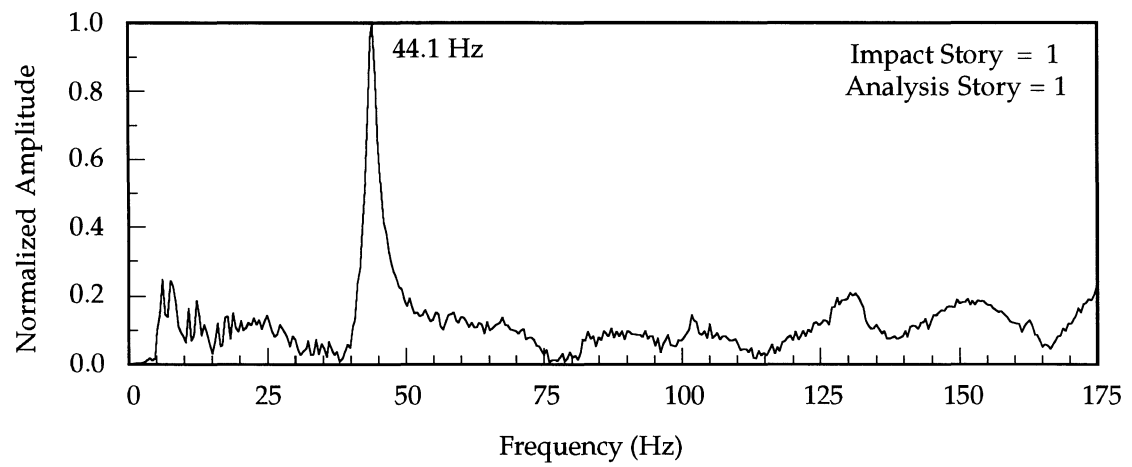
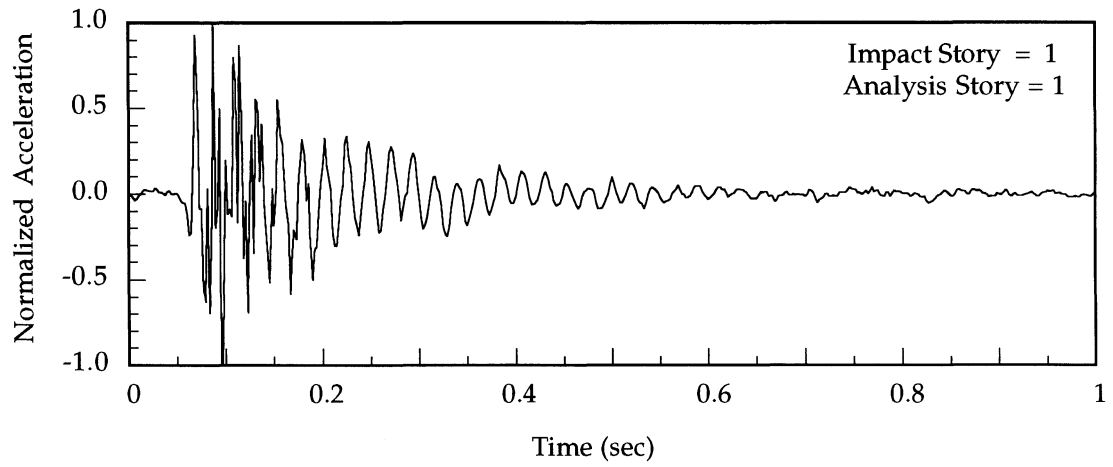


FIGURE 4-3 Infilled Frame Free Vibration Test

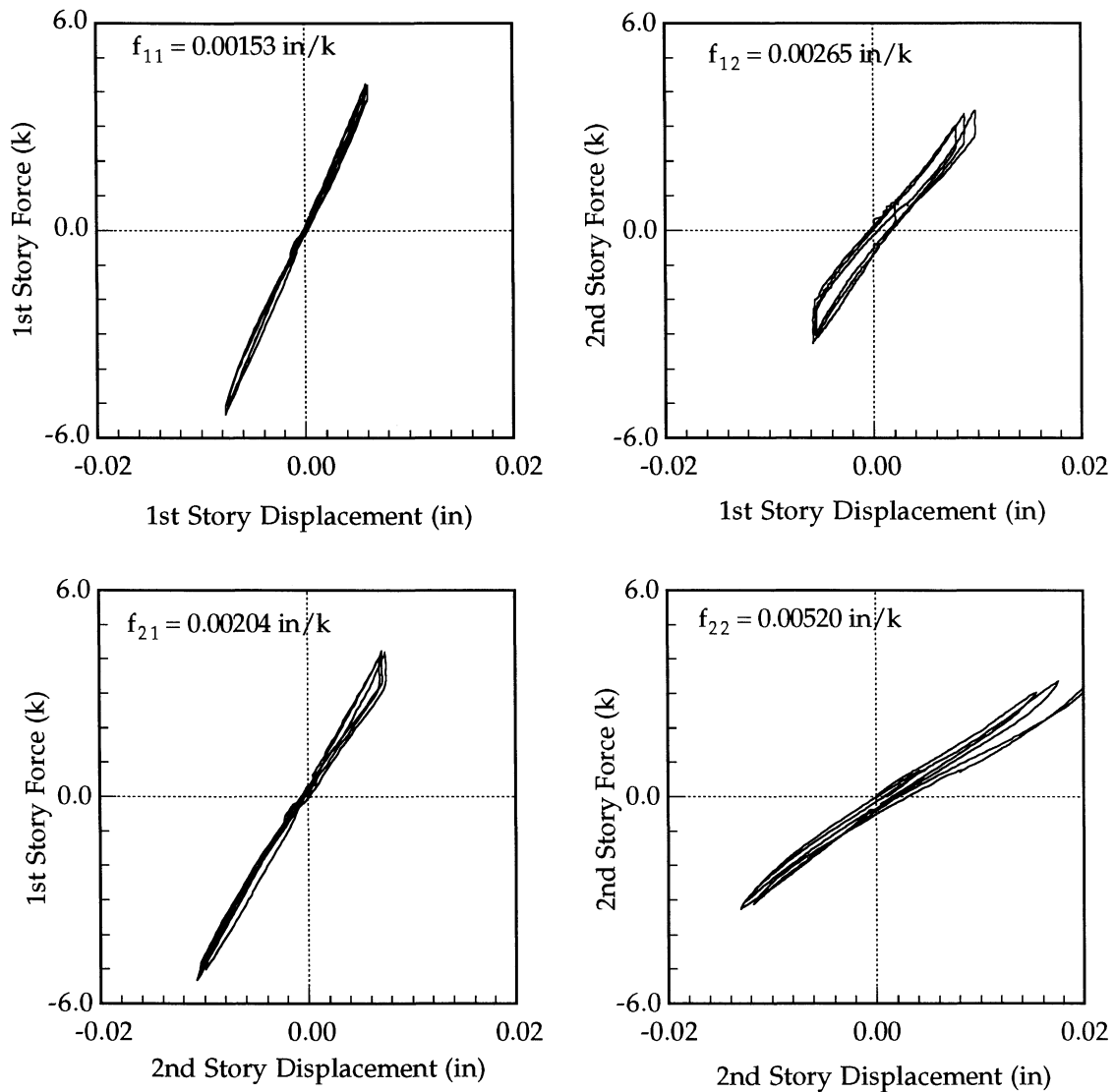


FIGURE 4-4 Infilled Frame Flexibility Tests

4.2.3. Analytical Verification

Although the infilled frame cannot be modeled analytically by a simple beam-column model as was done for the bare frame, the modal frequencies may still be verified with eigenvalue analysis. The specimen mass matrix including infill is

$$\mathbf{M}_{specimen} = \begin{bmatrix} 4.15 & 0 \\ 0 & 2.73 \end{bmatrix} \times 10^{-3} \text{ k} - \text{sec}^2/\text{in}. \quad (4.8)$$

This mass matrix represents the actual mass of the specimen in the laboratory; the subscript 'specimen' distinguishes it from the pseudodynamic

mass matrix, \mathbf{M} , which includes prototype mass not physically modeled in the lab (see Section 6.1). Using the matrices of Eqs. (4.7) and (4.8), the eigenvalue analysis shows reasonable correspondence in the first mode and predicts a second mode at 141 Hz which was not detectable in the free vibration tests (Table 4-2).

TABLE 4-2 Infilled Frame Frequencies

	Flexibility Test	Free Vibe Test
f_1 (Hz)	39.7	45.6
f_2 (Hz)	141.1	--

4.3. Damage and Repair

During the preliminary flexibility testing, significant horizontal movement of the base beam was detected, often as large as half of the first story displacement. Although the base displacement was always subtracted out from the story displacement readings, it was thought desirable to limit the base displacements before beginning pseudodynamic testing. The movement was suspected to be due to flexibility of the support head over the unsupported length of shaft in the below-floor recess. A mechanical jack was inserted between the reaction column and the east end of the base beam with the intention of supplying enough displacement to force the mounting shaft to bottom-out against the restraining collar at the floor level. During adjustment of this jacking system, the wall itself was accidentally overloaded, resulting in some cracking damage to the masonry.

As the damage resulted from loading in a single direction, the stiffness of the cracked structure was assumed now to be significantly asymmetric. In order to restore the nominally symmetric behavior of the wall, several methods of repair were considered. After consultation with two professional concrete repair and rehabilitation companies, an in-house technique was devised. The extent of damage and the repair method are detailed in Buonopane (1997).

The intention of the repair method was to allow future cracks to form at the damaged joint, but along the unrepaired mortar-block interface, and to allow stepped or diagonal cracks to propagate across the epoxy-repaired joints. Both such effects were observed during the later pseudodynamic testing. Thus it is believed that the damage and subsequent repair minimally affected the overall behavior of the structure during the pseudodynamic testing sequence.

4.4. Recharacterization

4.4.1. Flexibility Testing

A flexibility test was again performed on the infilled wall in the same manner as described previously. The curves presented in Figure 4-5 reveal reasonable symmetry and good repeatability, but a significant increase in hysteretic energy absorption, as evidenced by the increase in enclosed area (compare Figure 4-4). Note also that the initial loading curves exhibit noticeable softening, but appear to be asymptotic to a constant slope before load reversal. Linear fits to the load-deflection curves, shown as dashed lines in Figure 4-5, give an estimate of the average flexibility matrix

$$\mathbf{F} = \begin{bmatrix} 0.00378 & 0.00387 \\ 0.00435 & 0.01056 \end{bmatrix} \text{in/k}, \quad (4.9)$$

and average stiffness matrix

$$\mathbf{K} = \begin{bmatrix} 459 & -179 \\ -179 & 164 \end{bmatrix} \text{k/in.} \quad (4.10)$$

Eigenvalue analysis using this stiffness matrix and the specimen mass matrix of Eq. (4.8) results in new modal frequencies of 26 Hz and 60 Hz, compared to 40 Hz and 141 Hz from Table 4-2. All of these measurements indicate a significant overall reduction in stiffness for the repaired wall.

4.4.2. Shear Building Model

Idealization of the specimen as a shear building allows convenient isolation of the behavior of each story. The shear building concepts will also be used extensively for pseudodynamic testing. The shear building model assumes the rotational DOFs associated with each story level to be negligible. Thus the stiffness matrix of a shear building is

$$\mathbf{K} = \begin{bmatrix} k_1 + k_2 & -k_2 \\ -k_2 & k_2 \end{bmatrix}, \quad (4.11)$$

where k_1 and k_2 are lateral story stiffnesses. For the two DOF structure, story shears and drifts are defined by

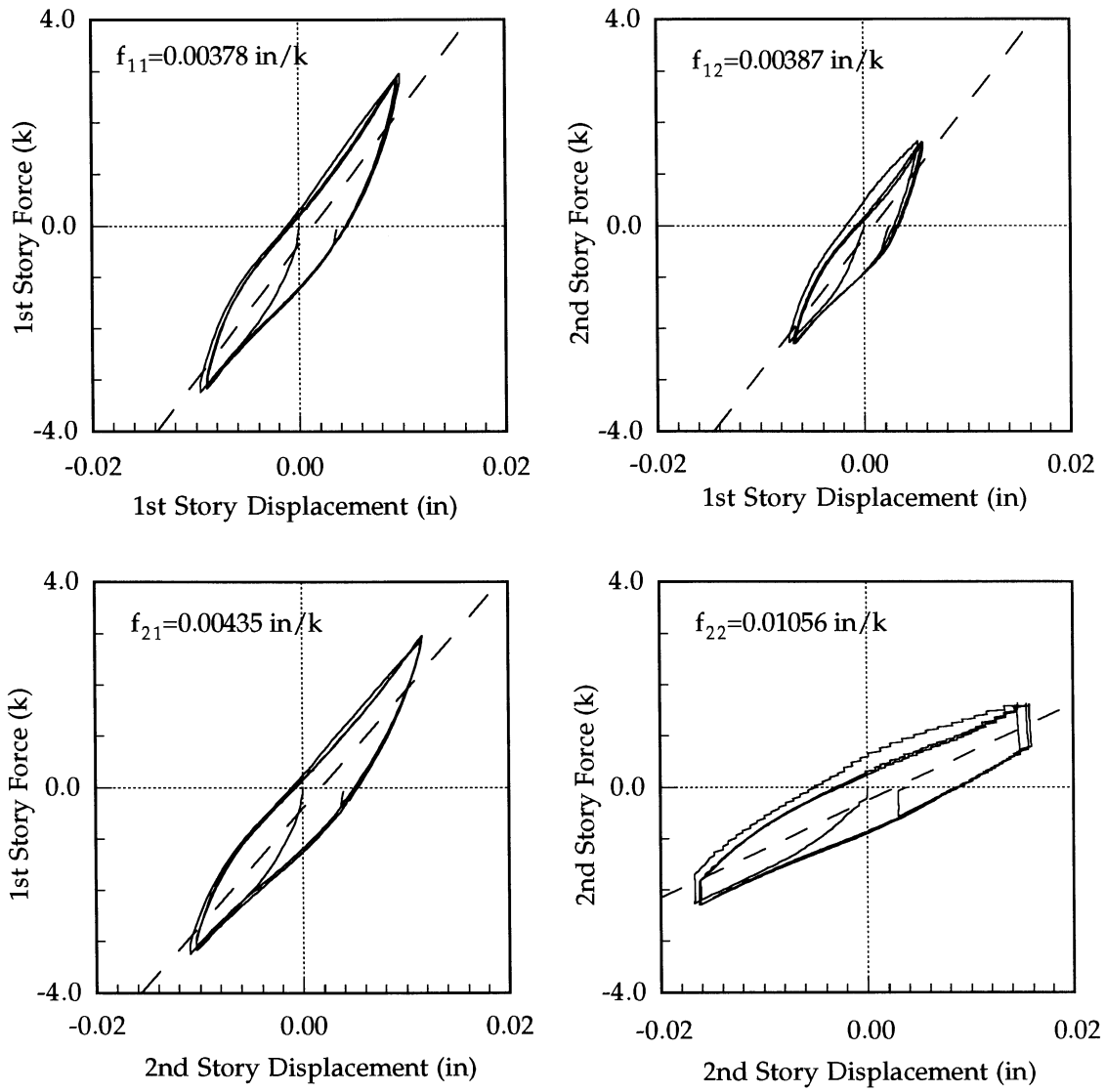


FIGURE 4-5 Infilled Frame Flexibility Tests

$$\begin{aligned}
(\text{Story Shear})_1 &= F_2 + F_1 \\
(\text{Story Shear})_2 &= F_2 \\
(\text{Drift})_1 &= d_1 \\
(\text{Drift})_2 &= d_2 - d_1
\end{aligned} \tag{4.12}$$

where F_i and d_i are story forces and displacements. From the matrix equation of static equilibrium,

$$\begin{Bmatrix} F_1 \\ F_2 \end{Bmatrix} = \begin{bmatrix} k_1 + k_2 & -k_2 \\ -k_2 & k_2 \end{bmatrix} \begin{Bmatrix} d_1 \\ d_2 \end{Bmatrix}, \tag{4.13}$$

the equations

$$\begin{aligned}
F_1 + F_2 &= k_1 d_1 \\
F_2 &= k_2 (d_2 - d_1)
\end{aligned} \tag{4.14}$$

directly relate story shear and drift. Thus on a plot of story drift versus story shear, the slope gives the appropriate story stiffness, and the matrix \mathbf{K} of Eq. (4.11) may be assembled. Note that this method can be applied to an arbitrary loading of the structure, not just a traditional stiffness test where each DOF is cycled in turn.

4.4.3. Stiffness Testing

Stiffness testing, as opposed to flexibility testing, is performed by displacing one DOF while holding the others fixed at zero displacement, and measuring forces and displacements of the structure. Stiffness testing was necessary for determination of the displacement control matrix, \mathbf{Q} , (see Section 5.4.2), but also provided a convenient method for determination of story stiffnesses, k_1 and k_2 . Due to flexibility in the loading system, holding an actuator fixed at a particular DOF did not guarantee that the structure itself remained fixed, nevertheless, the shear building approximation allows estimation of the stiffness matrix. Figure 4-6 shows the results of the stiffness test with gross stiffness values determined from the slope of a best fit line, giving

$$\mathbf{K} = \begin{bmatrix} 726 & -240 \\ -240 & 240 \end{bmatrix} \text{ k/in.} \tag{4.15}$$

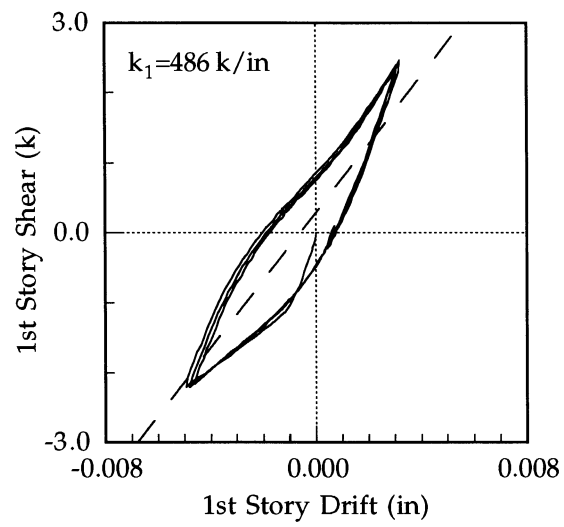
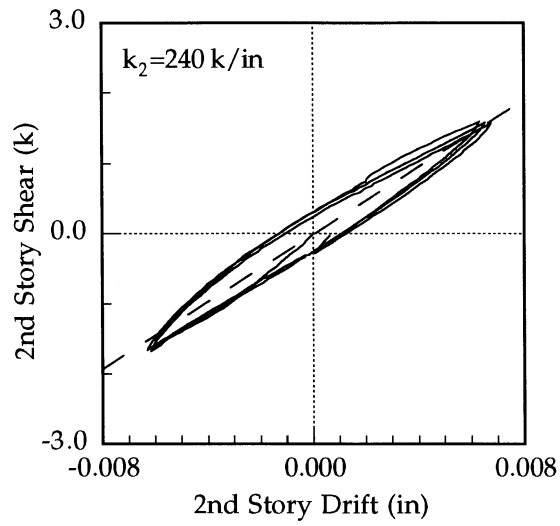


FIGURE 4-6 Infilled Frame Story Stiffness Tests

4.4.4. Hysteretic Energy Dissipation

Having isolated the behavior of each story, the hysteretic energy dissipation may now be quantified from story shear–story drift plots (Figure 4-6). A normalized energy ratio may be defined as

$$r_E = \frac{E_d}{E_s}, \quad (4.16)$$

where E_d represents the dissipated energy in one cycle and E_s the strain energy at peak displacement. The ratio in Eq. (4.16) is similar to that typically used to define the equivalent modal viscous damping ratio. However, here the dissipated energy ratio is used to measure hysteretic energy within a single story; the resulting values have no direct relation to modal damping ratios.

The dissipated energy equals the area enclosed by the story shear–story drift curves. Approximating the measured loops by a quadrilateral, the area of the loop may be easily calculated from the coordinates of the four corner points. From the post-repair plots of Figure 4-6, the energy ratios are approximately 1.47 in the first story and 0.81 in the second story. From the pre-damage flexibility test summarized in Figure 4-4, story shear–story drift relations may be plotted which give energy ratios of approximately 0.39 in the first story and 0.27 in the second story. Thus the damage and repair of the wall reduced the overall stiffness and increased the damping present.

SECTION 5 PSEUDODYNAMIC METHOD

5.1. Conceptual Basis

Pseudodynamic (PSD) testing combines features of quasistatic and shake-table testing, and numerical time-history analysis. A traditional static testing set-up is used with a specimen fixed to the testing floor, and with the relevant mass degrees of freedom (DOFs) controlled by hydraulic actuators. Similar to a shake table test, the pseudodynamic test subjects the structure to a specific excitation, for instance, a seismic ground acceleration record. However, instead of exciting the base, the pseudodynamic test moves the pertinent DOFs such that the time-history of relative displacements between the base and DOFs are comparable to those which would have occurred had the structure undergone the true base excitation. Such a displacement time history can only be determined beforehand for a linear system, where the properties of the system (\mathbf{M} , \mathbf{C} , \mathbf{K}) remain constant throughout the excitation. But, structures under extreme loading may exhibit significant nonlinear stiffness due to damage incurred during the excitation. Whereas numerical simulations rely on certain hysteretic rules to trace the changing stiffness based on some evolving system parameters, such as displacements or interstory drifts, pseudodynamic tests account for the nonlinear effects directly through experimentally measured restoring forces.

A general structure under dynamic excitation may be discretized into degrees of freedom and represented by the matrix equation of motion

$$\mathbf{M}\mathbf{a} + \mathbf{C}\mathbf{v} + \mathbf{K}\mathbf{d} = \mathbf{p}. \quad (5.1)$$

A quasistatic testing set-up in the laboratory allows convenient measurement of the displacements and forces, which are related to the stiffness matrix, \mathbf{K} , by

$$\mathbf{r} = \mathbf{K}\mathbf{d}. \quad (5.2)$$

Proper measurement of \mathbf{K} , however, requires a series of static tests, one for each DOF considered. The fundamental insight of pseudodynamic testing is the substitution of the term $\mathbf{K}\mathbf{d}$ in Eq. (5.1) by \mathbf{r} , the restoring force vector. All of the components of \mathbf{r} can be measured in a single step, and included in such measurements will be the effects of any nonlinearities in \mathbf{K} . Pseudodynamic testing measures the effects of nonlinearities in \mathbf{K} directly without any explicit determination of \mathbf{K} , whereas, nonlinear numerical simulation proceeds by explicit assembly of \mathbf{K} according to certain predefined rules. The remainder of

the PSD testing method follows directly from numerical integration techniques. A specific excitation record defines the load vector, \mathbf{p} . The mass and viscous damping matrices are specified numerically to represent the prototype structure, but do not need to be physically modeled in the lab. Displacement is related to its first and second time derivatives—velocity and acceleration—using any of the various numerical integration techniques available.

5.2. Development of Pseudodynamic Testing

The pseudodynamic test method was first proposed and used by Japanese researchers in 1975 (Takanashi et al., 1975). A U.S.-Japan Cooperative Earthquake Research Program in the 1980's provided impetus for further development of the method, with significant research effort in the US occurring primarily at University of California, Berkeley and University of Michigan, Ann Arbor. At that time much of the research focused on verification of accuracy of the test method itself and investigation into control of certain experimental intricacies found to affect the tests. Early comparative testing by pseudodynamic and shake table methods by Yamazaki et al. (1989) revealed two ongoing concerns: (1) loading rate effects lead to reduced restoring forces in PSD tests, and (2) experimental errors in displacement and force measurement may produce unrealistic higher mode response. Takanashi and Nakashima (1987) and Mahin et al. (1989) provide excellent summaries of this early development of the PSD test method in both Japan and the United States, and identify other practical concerns such as improvement in control of hydraulic actuators to limit the inevitable experimental errors in displacement and force measurements. Loading rate effects have largely been accepted as tolerable in comparison to uncertainties in small-scale shake table modeling, although the recent generation of tables capable of exciting full-scale specimens may again make this a significant concern.

Most of this first-generation PSD testing and research focused on the use of explicit time integration methods—central difference or explicit Newmark (Mahin and Shing, 1985). The intention of using PSD tests to study nonlinear behavior led to an avoidance of implicit techniques. With varying tangent stiffness at each time step, implicit solutions would require some iteration unless reliable prediction of the nonlinear stiffness could be made. Such iterations must actually be imposed on the specimen by moving the structure and therefore may introduce unrealistic loading cycles—one of the very drawbacks of quasistatic testing meant to be avoided with PSD testing. The application of explicit integration is limited by a conditional stability limit of

$$\Omega = \omega_n(\Delta t) < 2, \quad (5.3)$$

with ω_n , the largest circular frequency of the structure. For structures with one, or few, DOFs, the limit on Δt necessary for accurate representation of the earthquake loading usually satisfies the stability condition. But even for small DOF systems tested pseudodynamically, the numerical accuracy in each mode is proportional to frequency. Further, this error is cumulative in nature, so the additional experimental error added to the numerical process can develop rapidly into spurious higher mode response (Shing and Mahin 1987a, 1990).

The desire to test full scale structures with many DOFs and stiff, shear wall-type structures led to much research effort towards controlling higher-mode error propagation and introducing implicit integration to overcome the stability limit. Early methods developed included the introduction of numerical damping (Shing and Mahin 1987b), and a novel, hybrid algorithm implemented as a combination of numerical and analog-electronic methods (Thewalt and Mahin 1995). The most recent developments have focused on PSD-specific adaptations of implicit numerical integration algorithms. Two such schemes have emerged as the most widely accepted: (1) the α -method of Shing et al. (1991) based on Hilber- α integration (Hilber, 1976), and (2) the operator-splitting (OS) algorithm of Nakashima et al. (1990). The α -method of Shing possesses extremely favorable error accumulation characteristics over a wide range of frequencies and prevents cyclic loading during iteration through a relaxation parameter. The OS algorithm requires no iteration by using an estimated tangent stiffness matrix and by introducing numerically a residual force imbalance correction. An excellent summary of this second generation of PSD test methods appears in Shing et al. (1996). Donea et al. (1996) present comparative results from PSD tests on a 3-story steel frame using both implicit methods and the central difference method.

As a result of these developments the use of PSD testing for stiff, multistory specimens has become more common in both the United States and Europe. A major PSD experimental program at the University of California, San Diego has been conducted on a five-story, full-scale reinforced masonry specimen. Two significant innovations developed during the course of this research include "soft-coupling" (Section 5.4.2) to improve actuator control, and the "generated sequential displacement" method to generalize the PSD test beyond a single ground motion. Results of this program have been published in numerous fora, including Seible et al. (1994a, 1994b) and Seible et al. (1996), as well as several technical reports between 1991 and 1994. In Europe, Donea et al. (1996) report on the testing of a four-story, full-scale reinforced concrete frame, and a reduced-scale series of bridge piers using substructuring. At Cornell University previous PSD testing has been performed on a two-story, two-bay infilled steel frame (Mosalam, 1996). All of the aforementioned tests used some form of the implicit integration schemes. However, recent testing by Negro et al. (1996) used the central difference algorithm on a four-story full-scale reinforced concrete specimen.

Review of PSD development reveals certain unique advantages and disadvantages of PSD testing as compared to quasistatic or shake-table testing, and nonlinear numerical analysis.

Advantages:

1. For multi-DOF systems, no assumptions on the distribution of seismic forces among the DOFs need to be made.
2. Full-scale and large specimens may be tested with equipment requirements not much different than necessary for quasistatic testing.
3. Controlled testing speed allows for data acquisition from extensive instrumentation with modest electronics, and careful recording of important information such as crack trajectories.
4. Specimen mass need not be accurately reproduced in the lab as it is modeled numerically.
5. Effects of damage on behavior are physically modeled with no numerical assumptions regarding degradation necessary.
6. Unique substructure tests are possible, where part of the prototype is built and tested in the lab, while the remainder is modeled numerically within the time integration loop.

Disadvantages:

1. Error propagation characteristics of numerical integration require excellent hydraulic control of actuators and tight tolerances on experimental error in displacement and force feedback.
2. Nonlinear behavior sensitive to strain rate cannot be reproduced without real-time PSD testing.
3. Controlled testing speed and small integration time steps for numerical accuracy may cause excessive testing times.
4. Test response is often specific to a particular input motion.

Of course many of these advantages and disadvantages apply to one or more of the other testing methods.

5.3. Mathematical Formulation

The pseudodynamic test proceeds through sequential numerical integration of the equation of motion, application of the specified displacement, and measurement of the restoring forces. The numerical integration may be based on any of the Newmark-Beta family of algorithms or several adaptations developed specifically for pseudodynamic testing. For the present testing the explicit Newmark ($\beta=0$, $\gamma=0.5$) algorithm was used, with a small time step (≈ 0.0035 sec) to ensure stability and accuracy. The fundamental displacement and velocity relations are

$$\mathbf{d}_{i+1} = \mathbf{d}_i + (\Delta t)\mathbf{v}_i + \frac{1}{2}(\Delta t)^2 \mathbf{a}_i \quad (5.4)$$

$$\mathbf{v}_{i+1} = \mathbf{v}_i + (\Delta t)(1 - \gamma)\mathbf{a}_i + (\Delta t)\gamma\mathbf{a}_{i+1}. \quad (5.5)$$

Substituting these into the equation of motion, the acceleration, \mathbf{a}_{i+1} , may be found by the equivalent system

$$\mathbf{a}_{i+1} = \mathbf{M}^{*-1} \mathbf{p}^*, \quad (5.6)$$

where the effective mass, \mathbf{M}^* , and effective load, \mathbf{p}^* , are given by

$$\mathbf{M}^* = \mathbf{M} + (\Delta t)\gamma\mathbf{C} \quad (5.7)$$

$$\mathbf{p}^* = \mathbf{p}_{i+1} - \mathbf{r}_{i+1} - \mathbf{C}(\mathbf{v}_i + (\Delta t)(1 - \gamma)\mathbf{a}_i). \quad (5.8)$$

To step forward in time, the target displacement, \mathbf{d}_{i+1} , calculated from Eq. (5.4) is applied to the structure and the restoring force vector, \mathbf{r}_{i+1} , measured. The effective load vector is calculated and used to determine the new acceleration. Finally the new velocity is calculated from Eq. (5.5) and the process repeated. The flowchart in Figure 5-1 summarizes the explicit PSD algorithm.

5.4. Control Algorithm for Stiff Structures

5.4.1. Dual Displacement Control

A dual displacement control system is used in which internal displacement transducers (LVDTs) drive the actuator servo-hydraulic control loop and external displacement transducers (DCDTs) measure building story displacements directly. This arrangement, shown schematically in Figure 5-2, was first used in Japan by Takanashi and Nakashima (1987) and in the U.S. by Shing et al. (1991). The command displacement vector to the actuators is

designated by $\bar{\mathbf{d}}^a$, as opposed to the measured story displacement vector, $\hat{\mathbf{d}}^s$. In general, variables with the 'overbar' refer to numerically calculated command or target values, while variables with the 'overcaret' refer to measured values. A superscript 's' refers to structure displacements, and 'a' to the actuator. The advantages of this technique include eliminating the effects of reaction frame deformation, active compensation due to base beam movement and prevention of external disturbances from directly affecting the actuator control.

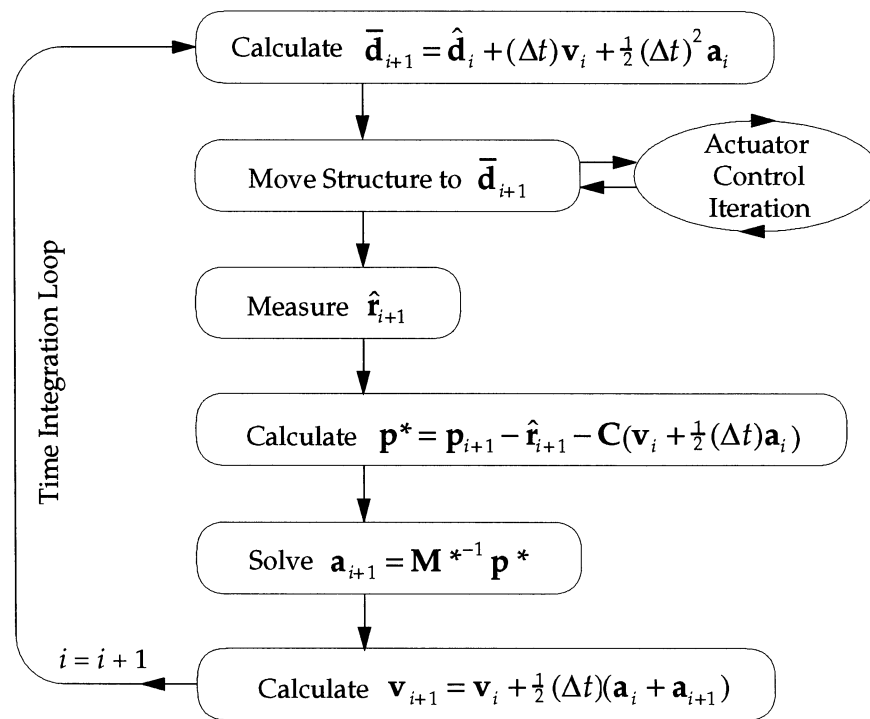


FIGURE 5-1 Explicit Pseudodynamic Algorithm

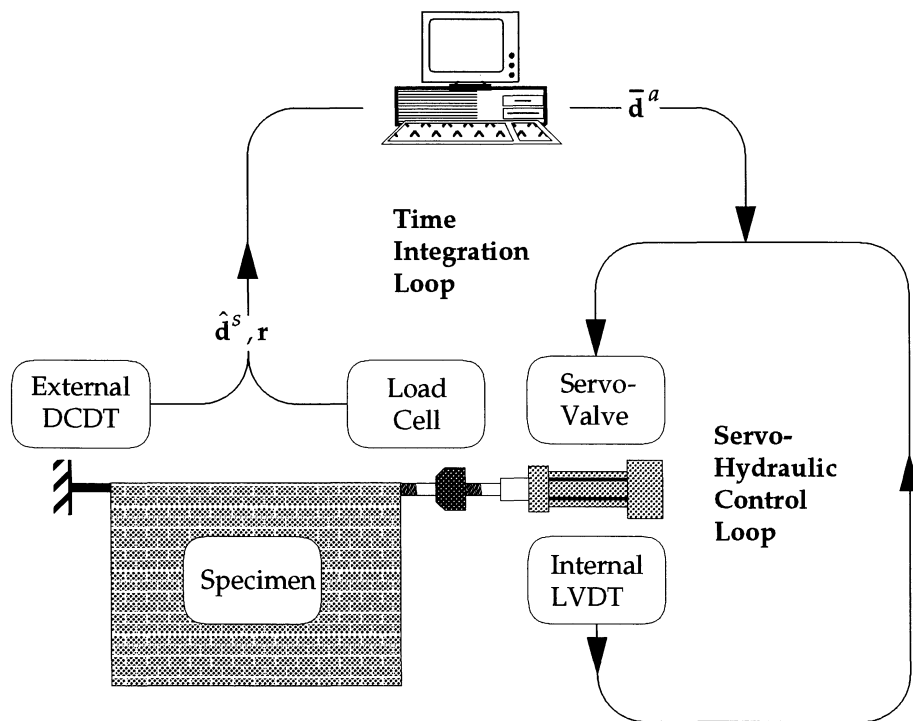


FIGURE 5-2 Pseudodynamic Control Schematic

5.4.2. "Soft Coupling" Formulation

"Soft coupling" refers to an experimental set-up with a loading system in which the actuator displacements are significantly less than the corresponding structural displacements. This method, first introduced and studied at University of California, San Diego, is described in detail in Igarashi et al. (1994). In testing the five-story reinforced masonry building, lateral load was applied at four points (two per loading beam) on the floor slab, none of which were directly over the lateral load-resisting walls. In order to help produce a more uniform load on the walls, elastomeric pads were inserted between the load beams and floor slabs. As a result the displacements of the actuators and building are significantly different, with no direct control of the story displacements. For quasistatic testing measuring the story displacements may be sufficient, but in PSD testing the structure must be moved to a specific displacement profile dictated by the numerical integration before restoring forces can be measured. Target building displacements from the numerical integration can no longer be used directly as actuator command displacements.

A typical two-story structure may be represented by the idealized stick model shown in Figure 5-3 and by the matrix equation

$$\begin{pmatrix} R_1^s \\ R_2^s \end{pmatrix} = \begin{bmatrix} k_1^s + k_2^s & -k_2^s \\ -k_2^s & k_2^s \end{bmatrix} \begin{pmatrix} d_1^s \\ d_2^s \end{pmatrix}, \quad (5.9)$$

where k_1^s and k_2^s represent the first and second story stiffnesses of the structure, respectively. Including the loading system as two ideal springs (Figure 5-3) results in the partitioned matrix equation

$$\begin{pmatrix} \mathbf{R}^s \\ \mathbf{R}^a \end{pmatrix} = \begin{bmatrix} \mathbf{K}^{ss} & \mathbf{K}^{sa} \\ \mathbf{K}^{as} & \mathbf{K}^{aa} \end{bmatrix} \begin{pmatrix} \mathbf{d}^s \\ \mathbf{d}^a \end{pmatrix}, \quad (5.10)$$

where the terms with superscript 's' represent the DOFs associated with the structure itself, and 'a' with the actuators. If the stiffnesses of the loading linkages are given by k_1^a and k_2^a the entire stiffness matrix, \mathbf{K} , can be shown to be

$$\mathbf{K} = \begin{bmatrix} k_1^s + k_2^s + k_1^a & -k_2^s & -k_1^a & 0 \\ -k_2^s & k_2^s + k_2^a & 0 & -k_2^a \\ -k_1^a & 0 & k_1^a & 0 \\ 0 & -k_2^a & 0 & k_2^a \end{bmatrix}. \quad (5.11)$$

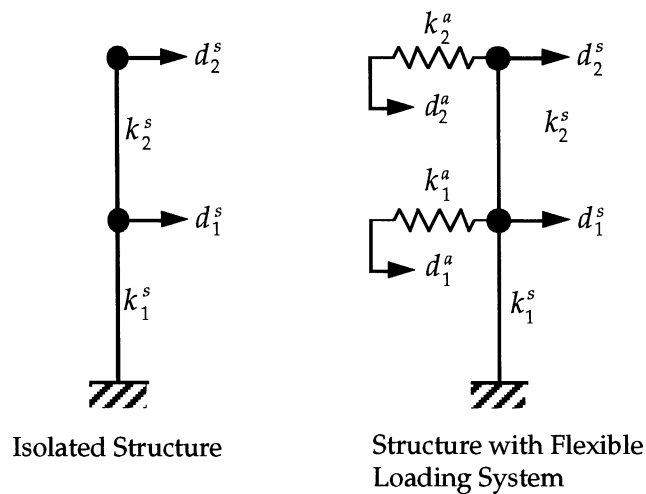


FIGURE 5-3 "Soft-Coupling" Idealization

The system with the included flexible loading system contains two potential complexities: (1) can the static behavior of the structure alone be isolated from that of the loading system, and (2) can a successful control scheme be developed and implemented?

The first question may be answered by recognizing that the forces measured at the actuators by the load cells are equal to the internal forces at the structure's story DOFs. Thus the measured story displacements, $\hat{\mathbf{d}}^s$, will be related to the measured restoring forces, \mathbf{r} , through the structural stiffness matrix alone. This may be shown rigorously by static condensation of Eq. (5.10), resulting in

$$\begin{aligned}\mathbf{R}_{cond} &= \mathbf{K}_{cond} \mathbf{d}^s \\ \mathbf{R}_{cond} &= \mathbf{R}^s - \mathbf{K}^{sa} (\mathbf{K}^{aa})^{-1} \mathbf{R}^a \quad . \\ \mathbf{K}_{cond} &= \mathbf{K}^{ss} - \mathbf{K}^{sa} (\mathbf{K}^{aa})^{-1} \mathbf{K}^{as}\end{aligned}\tag{5.12}$$

From the matrix of Eq. (5.11), \mathbf{K}_{cond} is equal to the two degree of freedom structural stiffness matrix in Eq. (5.9). Since $\mathbf{R}^s = \mathbf{0}$, $\mathbf{R}_{cond} = \mathbf{R}^a$, and Eq. (5.12) reduces to

$$\mathbf{R}^a = \mathbf{K}^s \mathbf{d}^s, \tag{5.13}$$

where \mathbf{K}^s denotes the stiffness matrix in Eq. (5.9). As \mathbf{K}^s is the stiffness matrix of the structure independent of the loading system, the forces measured at the actuator DOFs are truly related to the displacements measured at the structure DOFs by \mathbf{K}^s alone.

The development of a successful control scheme for "soft coupled" experiments has been published in Seible et al. (1996), and is reviewed briefly here with some minor modifications. This scheme must relate actuator displacements, \mathbf{d}^a , to the structure displacements \mathbf{d}^s , so that the desired \mathbf{d}^s can be achieved through servo-hydraulic control of \mathbf{d}^a alone. The first equation from the partitioned matrix of Eq. (5.9) with $\mathbf{R}^s = \mathbf{0}$, results in

$$\mathbf{d}^a = \mathbf{Q} \mathbf{d}^s \tag{5.14}$$

$$\mathbf{Q} = (\mathbf{K}^{sa})^{-1} \mathbf{K}^{ss}, \tag{5.15}$$

where \mathbf{Q} is termed the "displacement control matrix." Using the matrix of Eq. (5.11) and assuming that $k_1^a = k_2^a = k^a$ gives the result of Seible et al. (1996)

$$\mathbf{Q} = \mathbf{I} + \frac{1}{k^a} \mathbf{K}^s, \quad (5.16)$$

where \mathbf{I} is the identity matrix. Eq. (5.16) reveals that the matrix \mathbf{Q} is a function of the relative stiffnesses of the loading system and the structure, and that when the loading system is much stiffer than the structure, $k^a \gg \|\mathbf{K}^s\|$, then $\mathbf{Q} = \mathbf{I}$.

Although \mathbf{Q} will change as the structural stiffness \mathbf{K}^s deteriorates, it may be assumed constant over a single small actuator movement. Thus we may write

$$(\bar{\mathbf{d}}^a - \hat{\mathbf{d}}^a) = \mathbf{Q}(\bar{\mathbf{d}}^s - \hat{\mathbf{d}}^s) \quad (5.17)$$

where $\hat{\mathbf{d}}^a$ and $\hat{\mathbf{d}}^s$ are the current measured position vectors of the actuator and structure, $\bar{\mathbf{d}}^s$ the target displacement of the structure, and $\bar{\mathbf{d}}^a$ the displacement command signal to the actuator. If \mathbf{Q} were known exactly and remained constant, the target displacement $\bar{\mathbf{d}}^s$ could be achieved with a single actuator command $\bar{\mathbf{d}}^a$. However, the matrix \mathbf{Q} may be difficult to determine (Section 5.4.3) and may change during the duration of a single test as \mathbf{K}^s changes. Therefore a reduction factor of ξ is applied to \mathbf{Q} to prevent overshooting the target $\bar{\mathbf{d}}^s$, and an iteration loop is used to converge to that target. The iteration scheme over index k proposed by Seible et al. (1996) is

$$\bar{\mathbf{d}}_{(k+1)}^a = \bar{\mathbf{d}}_{(k)}^a + \xi \mathbf{Q}(\bar{\mathbf{d}}^s - \hat{\mathbf{d}}_{(k)}^s), \quad (5.18)$$

where the iteration is halted when the difference $(\bar{\mathbf{d}}^s - \hat{\mathbf{d}}_{(k)}^s)$ falls below a certain tolerance level. The current actuator command signal, $\bar{\mathbf{d}}_{(k)}^a$, is used in Eq. (5.18) rather than the measured actuator position, $\hat{\mathbf{d}}_{(k)}^a$, because Seible et al. (1996) show that use of $\hat{\mathbf{d}}_{(k)}^a$ can produce a stagnancy in the convergence due to inaccuracies inherent in typical servo-hydraulic control systems (Section 6.2).

Seible et al. (1996) demonstrate that intentional soft coupling may be used to overcome several experimental problems typically associated with pseudodynamic testing of stiff structures. The reduction in displacement from the actuator to the structure allows movement of the structure in increments below the resolution limit of the actuator. Such fine displacement control can be especially useful during shakedown testing when extremely low-level excitations are used to verify the pseudodynamic algorithm and testing software without causing any damage to the specimen. This displacement reduction also implies a reduction in effective actuator

stroke, but generally with stiff and brittle specimens enough degradation will occur at moderate displacement ranges to reduce the magnitude of \mathbf{Q} to where $\mathbf{d}^a \approx \mathbf{d}^s$.

More significantly, the iteration scheme of Eq. (5.18) with an ideal \mathbf{Q} matrix has equal convergence rates in all modes. By preventing extreme error accumulation in higher modes, this iteration scheme avoids one of the long-standing pitfalls of PSD testing. Even under laboratory conditions, an approximate \mathbf{Q} matrix has shown to be extremely effective in reducing the spurious higher-mode response which plagues so many pseudodynamic tests.

5.4.3. Determination of \mathbf{Q} Matrix

The success of this control algorithm depends largely upon the use of a well-determined matrix \mathbf{Q} . Seible et al. (1996) present only the simplified case where $k_1^a = k_2^a = k^a$ with \mathbf{Q} defined by Eq. (5.16). The load system flexibility, or soft-coupling, is assumed to be due entirely to the elastomeric pad connection. Both the elastomeric pad stiffness, k^a , and specimen stiffness, \mathbf{K}^s , can be individually measured and \mathbf{Q} assembled from Eq. (5.16). For the scale factor ξ Seible et al. (1996) recommend applying separate factors to each term in Eq. (5.16) so that the term $\xi\mathbf{Q}$ of Eq. (5.17) would become

$$\xi\mathbf{Q} = \xi_1\mathbf{I} + \frac{\xi_2}{k^a}\mathbf{K}^s. \quad (5.19)$$

Since \mathbf{Q} should approach \mathbf{I} as the structure deteriorates, separation of the scale factors allows for more realistic control of \mathbf{Q} over a series of tests.

In the present test set-up, "soft coupling" occurred as a result of several flexible components in the loading system. This effect was observed during initial stiffness testing and can be seen in the Figure 5-4 where both stories exhibit significant displacement when only a single actuator is moved. By placing a series of DCDTs along the loading chain from the building column to the reaction column, the majority of the extraneous displacement was found to occur in the threaded connections surrounding the load cell and in the loading plates (see Figure 3-3). The loading plates undergo significant bending due to the arrangement of the channel connections relative to the loading point. Also loading of the structure in both the east and west directions from actuators at only one end of the specimen introduces asymmetric contributions of flexibility from the loading system. Without the presence of discrete flexible items in the load system, the flexibilities of which could be measured individually, a direct experimental method to estimate \mathbf{Q} was devised.

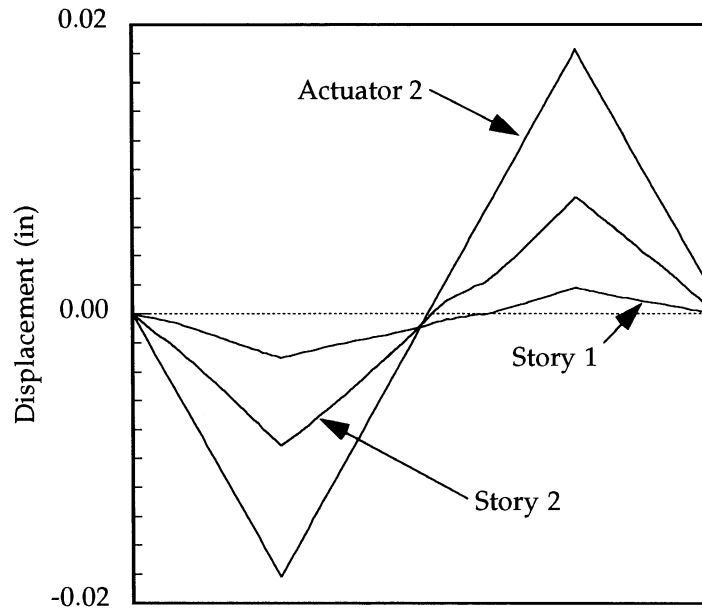


FIGURE 5-4 Displacement Cycle with Load System Interaction

The \mathbf{Q} matrix may be measured directly through static testing of the specimen, thus accounting for flexibility distributed anywhere in the loading system, symmetric or not. The fundamental relation of \mathbf{Q} in Eq. (5.14) may be inverted to give

$$\mathbf{d}^s = \mathbf{Q}^{-1} \mathbf{d}^a. \quad (5.20)$$

Experimental control of the actuator displacements, $\bar{\mathbf{d}}^a$, and measurement of both actuator and structure displacements, $\hat{\mathbf{d}}^a$ and \mathbf{d}^s , allow a static test to be performed wherein a single d_i^a is moved in a cyclic fashion while all other d_i^a 's are fixed at zero. Conveniently such measurements may be recorded during a typical stiffness test. From the measurements of \mathbf{d}^s , the value of $(Q^{-1})_{ij}$ may be determined as

$$(Q^{-1})_{ij} = \frac{\Delta d_i^s}{\Delta d_j^a} \quad (5.21)$$

Typically the plots of d_i^a versus d_i^s show some nonlinearity and asymmetry, but a reasonable estimate will usually give acceptable performance (Section 6.2). Further the scale factor, ξ , helps to produce monotonic convergence with a less than ideal estimate of \mathbf{Q} .

Figure 5-5 shows a typical set of plots generated during preliminary stiffness testing of the infilled frame. Linear approximations to the plots are used to estimate the displacement control matrix

$$\mathbf{Q} = \begin{bmatrix} 4.69 & -1.24 \\ -1.57 & 2.52 \end{bmatrix}. \quad (5.22)$$

After each pseudodynamic test a static stiffness test was conducted to determine both the new stiffness and \mathbf{Q} matrices. In general, the \mathbf{Q} matrix did tend to approach the identity matrix after successive damage in the PSD testing sequence. The final matrix used for the Taft 0.80g test was

$$\mathbf{Q} = \begin{bmatrix} 1.73 & -0.30 \\ -0.53 & 1.31 \end{bmatrix}. \quad (5.23)$$

The plots for the Taft 0.80g test showed even greater irregularity than those of Figure 5-5. In the pseudodynamic testing software, an option was included to pause the test momentarily and manually input new terms in \mathbf{Q} . However even with the severe degradation during the Taft 0.80g test, \mathbf{Q} of Eq. (5.23) provided satisfactory actuator control throughout the duration of the test.

Direct measurement of \mathbf{Q} also helps to alleviate other experimental complications, such as base movement, by accounting for these effects implicitly. If the measured displacements used in Eq. (5.21) include the effects of base movement, then the actuator control routine will perform more efficiently in producing the desired true structural displacements relative to the base. Initially in these experiments, the base displacement had little effect on \mathbf{Q} , but when applying larger story shears during the higher level tests the effects of base movement needed to be included in order to determine a reasonable \mathbf{Q} matrix. The base beam slipped in both the east and west directions with a time history similar to those of the story displacements, but with a much smaller amplitude. As the structure sustained damage and decreased in stiffness, the base beam displacement decreased relative to the story displacements. However, the absolute magnitude of base beam displacement continued to increase with increasing applied peak story shear.

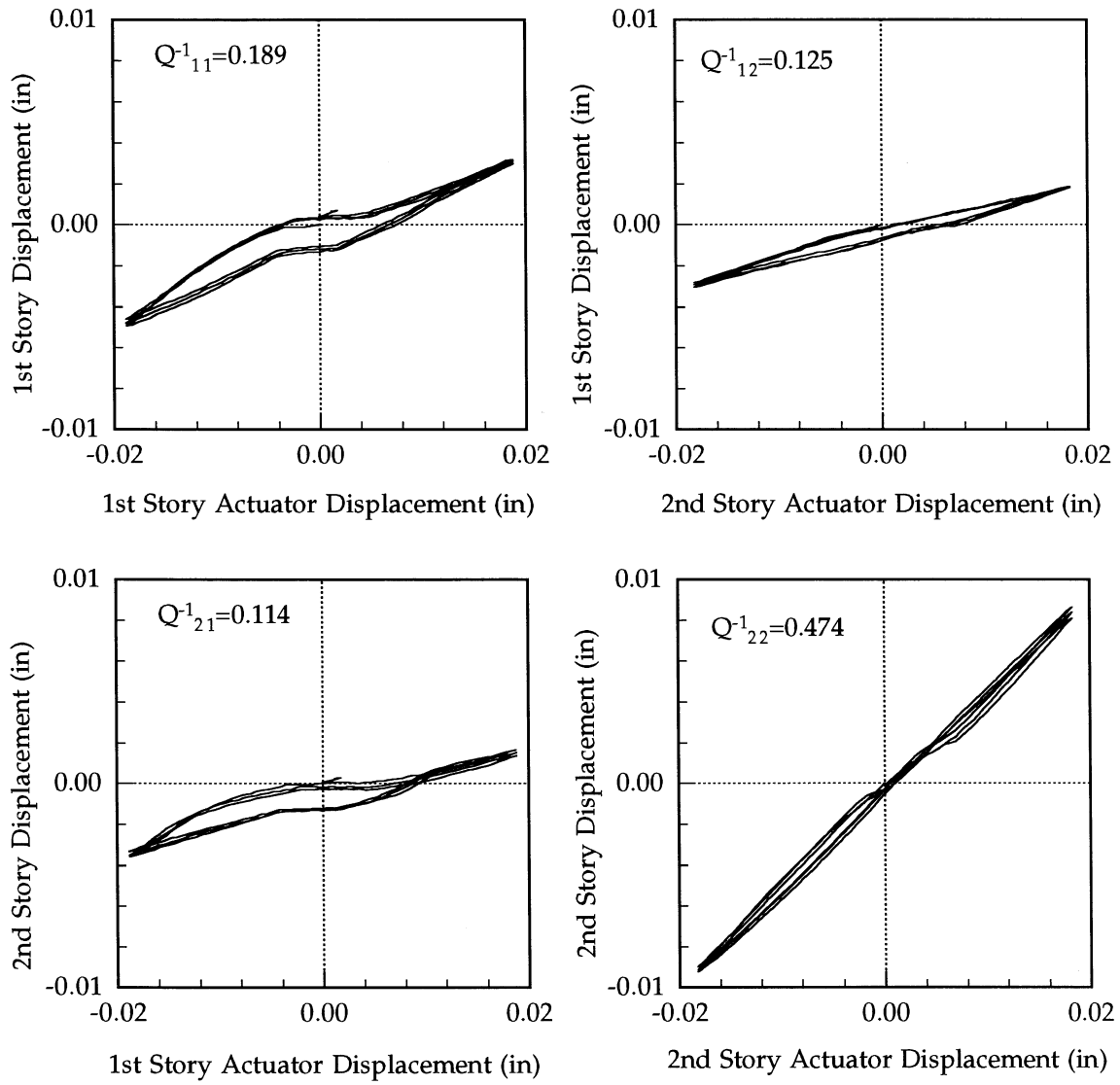


FIGURE 5-5 Q Matrix Test Results

**SECTION 6
PSEUDODYNAMIC IMPLEMENTATION**

6.1. Mass and Damping Properties

The pseudodynamic algorithm requires numerical specification of the mass and viscous damping properties of the specimen. The mass matrix represents the true mass of the scaled prototype structure and may include mass not physically modeled in the specimen. A typical partial floor plan of the prototype structure was shown in Figure 1-2. Prototype dead loads considered in the calculation of the mass matrix appear in Table 6-1. Masonry infill and partition walls are assumed to rest on the supporting floor, therefore no contribution appears in the second story mass. Beams exist in both the tested direction (24 ft) and the transverse direction (3x12 ft), and the beam weights include only the stem of the effective T-section below the slab. Live loads are not included in the dynamic mass matrix. The total weights from Table 6-1 are divided by $g = 386 \text{ in/sec}^2$ and scaled according to

$$\mathbf{M}_{model} = (S_1)^2 \mathbf{M}_{prototype} \quad (6.1)$$

where $S_1 = 1/2$. The resulting mass matrix used in the pseudodynamic algorithm is

$$\mathbf{M} = \begin{bmatrix} 0.029 & 0 \\ 0 & 0.019 \end{bmatrix} \text{k - sec}^2/\text{in}. \quad (6.2)$$

Using this mass matrix and the shear building stiffness matrix of Eq. (4.15), the expected modal frequencies during low-level pseudodynamic testing are 13 Hz and 28 Hz in the first and second modes, respectively.

TABLE 6-1 Prototype Specimen Dead Loads

Item	Unit Weight	1st Story		2nd Story	
		Quantity	Weight (k)	Quantity	Weight (k)
Slab, 5" thick	62.5 psf	288 ft ²	18.0	288 ft ²	18.0
Beams, 10"x11"	115 lb/ft	60 ft	6.9	60 ft	6.9
Masonry Walls	50 psf	240 ft ²	12.0	--	--
Partition Walls	15 psf	360 ft ²	5.4	--	--
Ceiling & Mechanical	15 psf	288 ft ²	4.3	288 ft ²	4.3
Flooring or Roofing	3 psf	288 ft ²	0.9	288 ft ²	0.9
TOTAL			47.5		30.1

Idealization of natural damping as viscous allows convenient solution of the equation of motion. As the sources of damping in structures are extremely varied and complex, such an idealization is acceptable in most situations. Equivalent viscous damping estimates the total effect of viscous, hysteretic and Coulomb friction damping on the behavior of structure. However in pseudodynamic testing, the energy dissipation associated with hysteretic and friction damping is reproduced in the experiment itself and reflected implicitly in the measurements of displacement and restoring force. Only the natural damping, which causes the decay of small amplitude free vibrations, must be represented numerically. From the free vibration testing of the infilled frame, the modal damping ratios were estimated as $\zeta_1 = 2\%$ and $\zeta_2 = 5\%$ (see Section 4.2). Rayleigh or classical damping is an acceptable assumption for determination of the damping matrix, since the system has only 2 DOFs with roughly equal magnitude damping. The damping matrix is a linear combination of mass and stiffness

$$\mathbf{C} = a_0\mathbf{M} + a_1\mathbf{K}. \quad (6.3)$$

For desired damping ratios ζ_1 and ζ_2 , the coefficients a_0 and a_1 may be found from (Chopra, 1995)

$$\frac{1}{2} \begin{bmatrix} 1/\omega_1 & \omega_1 \\ 1/\omega_2 & \omega_2 \end{bmatrix} \begin{Bmatrix} a_0 \\ a_1 \end{Bmatrix} = \begin{Bmatrix} \zeta_1 \\ \zeta_2 \end{Bmatrix}. \quad (6.4)$$

Based on the stiffness matrix of Eq. (4.10) and mass matrix of Eq. (6.2), the damping matrix for pseudodynamic testing is

$$\mathbf{C} = \begin{bmatrix} 0.318 & -0.126 \\ -0.126 & 0.112 \end{bmatrix} \text{k - sec/in.} \quad (6.5)$$

The damping matrix was assumed constant throughout the pseudodynamic testing sequence and was not updated based on degrading stiffness.

6.2. Control Parameters

The actuator control system should be able to move the structure to the desired story displacements within a specified tolerance, without grossly overshooting the target, and with a minimum number of iterations. Displacement control accuracy is necessary to minimize error in the force feedback, which may rapidly build up and overwhelm the numerical process (Shing and Mahin, 1990). A comprehensive discussion of experimental errors in pseudodynamic testing appears in Buonopane (1997, Secs. 7.2-7.3). Overshooting the target displacement may cause irreversible damage to the

specimen which then affects the remainder of the test. Excessive iterations can increase testing time beyond practical limits and can result in many load reversals near the target displacement which have the potential to cause unrealistic cyclic damage to the specimen.

In an effort to optimize performance of the pseudodynamic algorithm, the effects of several parameters on the control iteration of Eq. (5.18) were investigated using the first ten seconds of the Taft 0.10g record. The first two seconds of the Taft record contain extremely low-level excitation, which test the ability of the actuator to track small structure displacements near its resolution limit. The remaining eight seconds contain the large majority of strong ground motions from the complete record. During larger motions, the control system must be able to move the structure to the new target accurately and with a minimum number of iterations. In some cases the test was halted before ten seconds of input motion due to near-instability or excessive iterations.

The control parameters investigated were the use of the full \mathbf{Q} matrix compared with use of the identity matrix \mathbf{I} in place of \mathbf{Q} . In addition, the effects of the scale factor, ξ , were verified. The actuator stagnation effects cited in Seible et al. (1996) were observed experimentally through comparative tests using the command value, $\bar{\mathbf{d}}^a$, and the measured position, $\hat{\mathbf{d}}^a$ in Eq. (5.18). Finally, the effects of measured displacement updating (Shing and Mahin, 1990 and Mosalam, 1996) and the use of a time delay (Mosalam, 1996) were also examined. Detailed results, including numerical data and representative figures, for all of these effects appear in Buonopane (1997).

SECTION 7 PSEUDODYNAMIC VERIFICATION

7.1. Bilinear Modeling of a Low-Level Test

A low-level test of Taft 0.10g was used to verify the accuracy and stability of the pseudodynamic algorithm. The story drift-story shear plots (see Figure 8-2) show that the structure remained essentially undamaged under the low-level excitation, although enough nonlinearity was present to produce noticeable hysteresis, as in the static testing (see Section 4.4 and Figure 4-6). Thus a bilinear stiffness model with no degradation was used to capture the observed hysteresis with no damage. Figure 7-1 summarizes the bilinear stiffness rules based on the shear building model. The behavior in each story is defined by an initial stiffness, k^a , final stiffness, k^b , and critical drift, d^0 , and the total stiffness matrix assembled according to Eq. (4.11). A drift reversal at d^r on the final stiffness branch results in a change to initial stiffness, and calculation of the new critical drift

$$d^* = d^r - 2d^0. \quad (7.1)$$

Upon reaching that critical drift, the stiffness reverts to the residual stiffness. Explicit Newmark integration is used to perform time history analysis. Table 7-1 gives bilinear parameters determined from examination of the plots of Figure 8-2 at low and high drifts ranges. These parameters were also verified against the results of the static stiffness tests described in Section 4.4.3.

Figure 7-2 compares measured and bilinear displacement and force time histories for both stories for four seconds of strong motion excitation. All of these comparisons show good correspondence between the measured and bilinear values, with most local extremes reproduced very closely. The hysteretic behavior in Figure 7-3 also shows good correspondence between measured and bilinear cases. Finally, the frequency spectra compared in Figure 7-4 verify the bilinear model as an acceptable representation of the low-level pseudodynamic test. The primary conclusion from the bilinear modeling is that experimental errors in displacement and force feedback, present in the low-level test but not in the bilinear model, have been controlled and reduced to the point which they do not significantly effect the performance of the pseudodynamic test.

TABLE 7-1 Bilinear Parameters

	k^a (k/in)	k^b (k/in)	d^0 (in)
1st Story	800	425	0.0010
2nd Story	325	240	0.0015

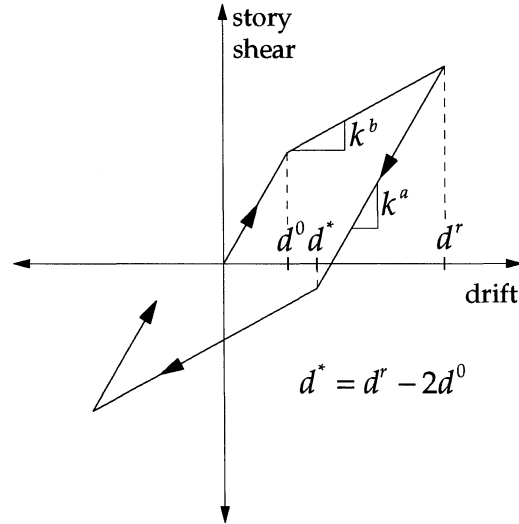


FIGURE 7-1 Bilinear Hysteresis Rules

7.2. Sources of Error

As pseudodynamic testing combines an experimental and numerical process, error from both sources may affect results. The numerical portion of the pseudodynamic test uses established integration routines, the error characteristics of which are reported in many standard dynamics textbooks (e.g. Chopra, 1995) and can usually be well controlled with small time steps relative to the fundamental period. Experience has shown that these numerical errors are generally of much smaller magnitude than experimental errors. On the other hand, experimental errors enter the numerical process through force and displacement feedback and may accumulate and overwhelm the numerical integration. Control of experimental errors always has been a major concern in pseudodynamic testing (see Section 5.2). A thorough examination of the error characteristics from these PSD tests appears in Buonopane (1997).

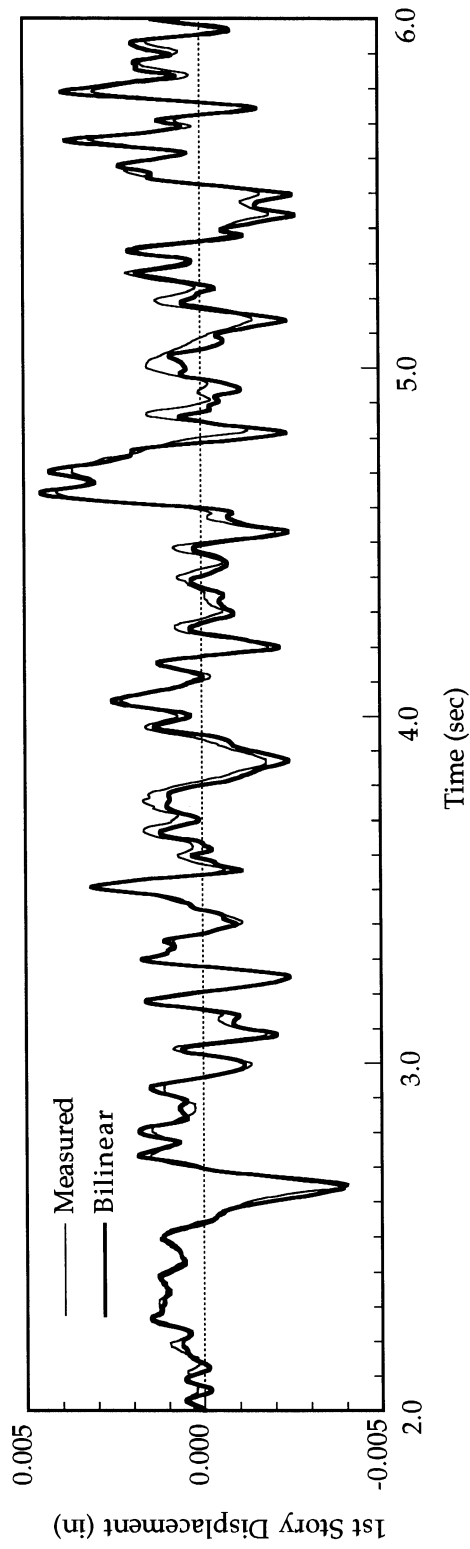
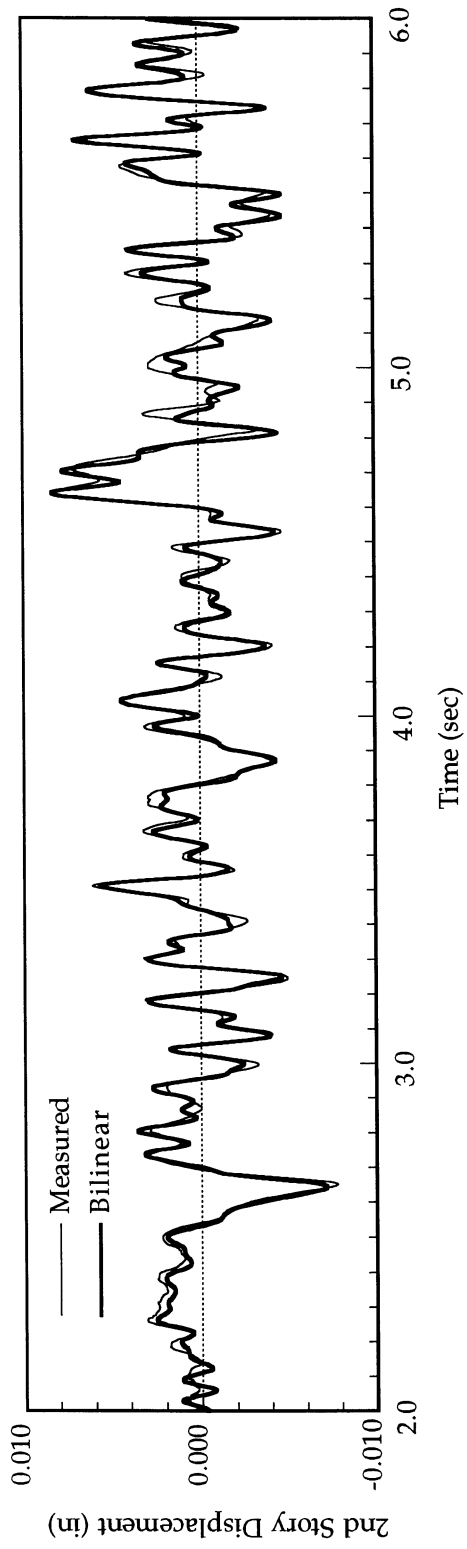


FIGURE 7-2 Bilinear and Measured Displacement Time Histories

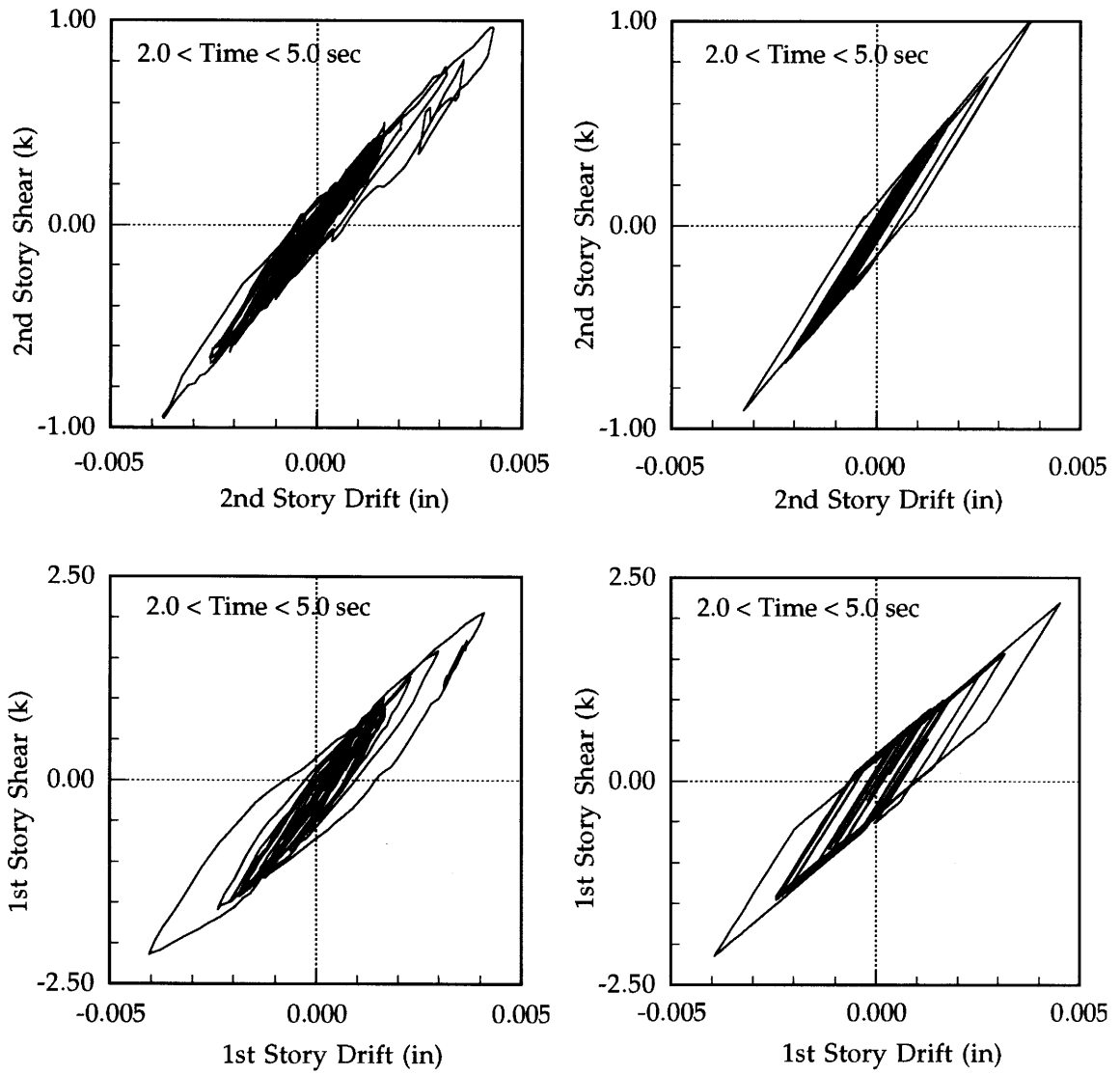


FIGURE 7-3 Bilinear and Measured Hysteretic Relations

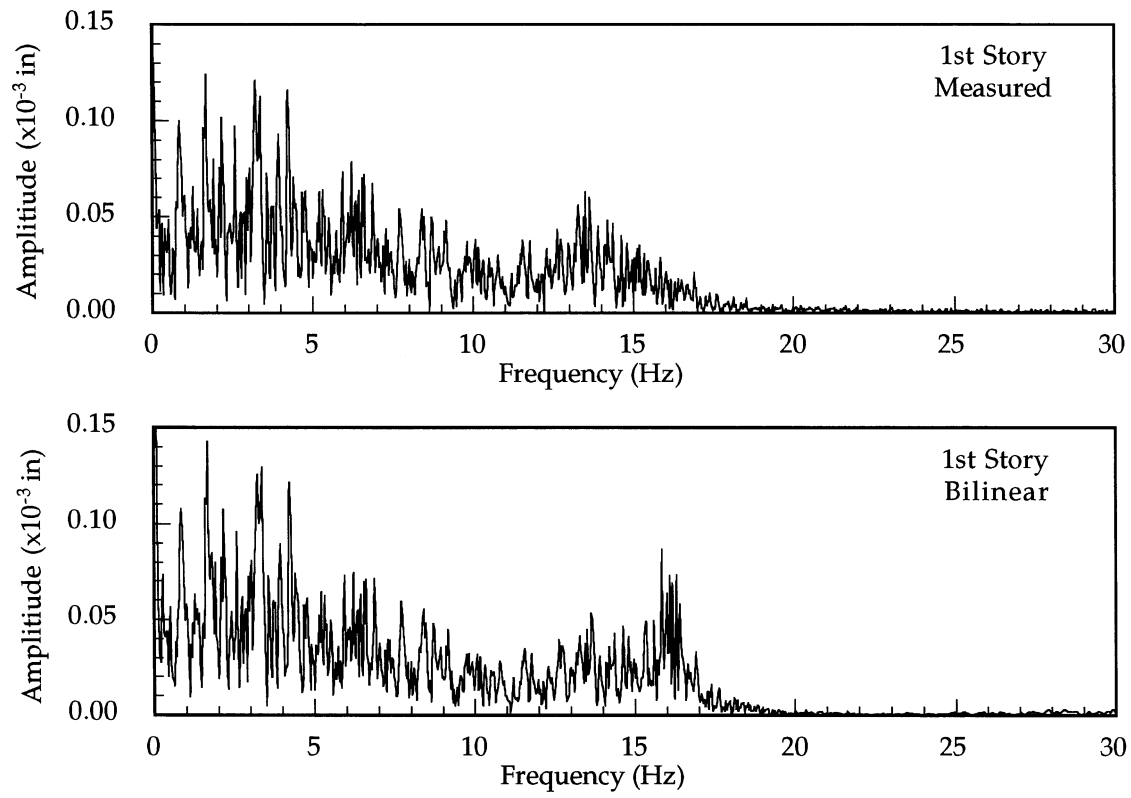


FIGURE 7-4 Bilinear and Measured Frequency Spectra

7.3. Tolerance and Displacement Error

The tolerance used to converge Eq. (5.18) sets an upper bound on the allowable displacement error at each time step. Actuator resolution generally limits the tolerance, but “soft coupling” does allow tolerances below the actuator resolution. For any given test, the actuator stroke should be adjusted based on expected peak displacements to maximize resolution. Table 7-2 lists the tolerances used in the final sequence of pseudodynamic tests. Tolerance is expressed as a semi-bandwidth, where measured displacement within one semi-bandwidth above or below the target displacement is considered converged. The tolerance expressed as a percentage of maximum measured displacement allows for comparison across tests of different excitation levels and to tests by other researchers. For instance, results reported by Seible et al. (1996) show percentages of about 0.7% and 0.4% for two of the tests on the five-story masonry structure.

While a small tolerance reduces displacement errors, the tolerance must not be so small as to cause excessive control iterations. In three of the four pseudodynamic tests the error never exceeded the preset tolerance. However, in the Taft 0.35g test the tolerance was extremely low relative to peak displacement, and at several time steps the control algorithm failed to converge within the iteration limit of 25. Of these unconverged steps, the maximum error carried forward into the numerical integration was about 1.4% of peak displacement, and therefore did not greatly affect the progress of the test. Similar excessive iterations have been reported by Seible et al. (1996), where errors on the order of 2 to 4% of peak displacement occurred at several steps.

The distribution of displacement error within the tolerance band was evaluated through histograms. In most cases the errors were fairly evenly distributed, although certain tests showed histograms significantly weighted near zero, while others exhibited a bimodal distribution. Representative error histograms appear in Buonopane (1997). In all cases the magnitudes of the errors remained within the tolerance band.

TABLE 7-2 Displacement Tolerance

Test pga (g)	Tolerance Semi- Bandwidth ($\times 10^{-3}$ in)	Maximum Displacement (in)	Tolerance as % of Max. Disp.	Maximum Error ($\times 10^{-3}$ in)
0.10	0.073	0.0084	0.87%	0.073
0.35	0.073	0.0835	0.09%	1.15
0.55	0.37	0.2004	0.18%	0.37
0.80	0.75	0.4659	0.16%	0.75

7.4 Over- and Undershooting Errors

Frequency spectra of displacement errors typically have been used as a performance benchmark in numerical pseudodynamic error studies (Shing and Mahin, 1987). Shing et al. (1996) state that Fourier spectra may be used to reveal systematic displacement control errors, as consistent actuator overshooting will cause a spike at the fundamental frequency; undershooting, at the highest natural frequency. Gross overshooting may lead to unintended damage, but of greater concern here is consistent undershooting, even of small magnitude, which consistently adds energy to the system near the highest modal frequency, potentially leading to spurious higher mode response. Nearly all of the previous pseudodynamic error studies have been based on numerically specified error functions. However, a recent study by Thewalt (1994) relies on error data from actual pseudodynamic testing and shows that a frequency spectrum of displacement error cannot distinguish between under- and overshooting. No other error spectra from actual experimental data appear to have been published, but the same conclusion can be reached from the experimental error data of these PSD tests.

Literature prior to Thewalt (1994) does not comprehensively define the difference between an overshoot and undershoot error. Undershooting and overshooting must be distinguished based on the absolute values of the desired and applied displacement increments. Application of a displacement increment smaller in magnitude than desired corresponds to an undershoot; larger, to an overshoot. Buonopane (1997) presents analyses of the displacement error frequency spectra and comparisons to occurrence frequency of under and overshooting errors. With a consistent definition of under and overshooting errors, there does not appear to be a direct relationship between spikes in the error frequency spectra and the occurrence or magnitude of under or overshooting errors. In these PSD tests, undershoot errors consistently occur more frequently and with greater magnitude, yet the error frequency spectra show varied distributions including near uniform, and peaks near high and low modal frequencies.

More importantly, the displacement control iteration presented in Section 5.4 prevents time integration from proceeding unless a certain predefined tolerance level is met. With a tight tolerance band, experimental displacement errors entering the numerical integration are limited to very small magnitudes. Even with actuator movement which consistently undershoots to protect the specimen from unintended damage, a tight tolerance can limit excessive energy addition and maintain cumulative error within acceptable bounds.

7.5 Numerical Simulation of Displacement Error

The determination of a proper tolerance level is crucial to contain error propagation within acceptable limits. Buonopane (1997) presents a series of numerical analyses which simulate the effects of experimental error using a random variable. The magnitude of the error can be varied, simulating different tolerance bands, and the effects on time histories and frequency spectra, studied.

The brief analyses of displacement control errors in true pseudodynamic testing suggest that they may have significantly different characteristics than previously published results based primarily on numerical simulation of linear elastic systems. The relatively simple numerical simulations reproduce the frequency effects cited elsewhere, but these frequency characteristics seem to have no clear relation to numerical time history performance, or measured PSD testing errors. Thewalt (1994) develops more reliable performance parameters which quantify the added or dissipated energy due to over- and undershooting displacement control errors. Although it has been expected that an inelastic system would exhibit milder error propagation problems, even the very small nonlinear behavior of the Taft 0.10g test greatly altered the behavior of error propagation. In fact, with the implementation of a successful displacement control iteration scheme, the error propagation problems appear to be significantly reduced.

SECTION 8 PSEUDODYNAMIC RESULTS

8.1. Testing Sequence

The final pseudodynamic testing sequence subjected the specimen to a series of four Taft earthquake records scaled to peak ground accelerations (pga) of 0.10, 0.35, 0.55 and 0.80g. These selected excitation levels for the PSD testing sequence can be compared with the "maximum considered earthquake" from the most recent edition of the NEHRP (1997) Provisions, which map spectral acceleration contours for 0.2 sec and 1.0 sec period structures. A period of 0.2 sec falls approximately midway between the undamaged infilled frame period (0.076 sec) and the bare frame period (0.302 sec). From the Taft 1.0g response spectrum (Figure 1-6), the spectral acceleration at 0.2 sec is about 3.5g. The corresponding spectral acceleration for the Taft 0.55g test is 1.9g; and for the Taft 0.80g test, 2.8g. The NEHRP maps give spectral acceleration contours for a seismic event with 2% probability of occurrence in 50 years, or a 2500 year return event. Contours in the Los Angeles, California area generally range from 1.50g up to 2.50g; while those in the San Francisco area range from 1.50g up to 2.00g. In other areas of the United States, the peak contour surrounding Charleston, South Carolina is 1.50g, while that surrounding the New Madrid area is 3.00g. Thus the two strongest PSD excitations are reasonable representations of the spectral accelerations currently believed to be expected in major seismic events in these areas of the United States.

The testing sequence was also selected to provide a basis for comparison with previous research on similar bare frames (El-Attar et al., 1991a, 1991b, 1997) and current shake-table testing of an infilled specimen based on the same prototype structure (Abdel-Mouti, 1997).

Further, the widely-spaced excitation levels were selected to minimize the effects of previous damage on any given test. That is, damage comparable to that existing from a previous test is considered likely to have occurred within the initial low-level excitation (prior to about 2.5 sec) of the current test, thereby leaving the specimen in the same approximate damage state at the onset of strong input motions (at about 2.5 sec). For instance, assuming damage to be related to story drift, the peak second story drift during the entire Taft 0.35g test was 0.050 in, while during the first 2.50 sec of the Taft 0.55g test the second story drift reached 0.045 in, and eventually reached 0.139 in. No attempt was made to quantify rigorously such damage assumptions; the numbers presented here are intended only to support the basic qualitative reasoning.

The Taft 0.10g excitation caused no visible damage, the structure responding mostly linearly with only slight hysteresis, similar in magnitude to that

observed during the static testing. As discussed in Section 7.1, this low-level, predictable response was used to verify the pseudodynamic algorithm, testing software and experimental setup. In addition it can provide insight into the behavior of the infilled frame system under mild lateral loads such as wind. The Taft 0.35g test introduced enough nonlinearity to test the behavior of the pseudodynamic control algorithm with true stiffness degradation due to minor damage and some separation between infill and frame. Having demonstrated the ability of the pseudodynamic scheme in the nonlinear range, the final tests at 0.55g and 0.80g were intended to produce significant damage and degradation of the infill and frame comparable to that caused during a strong excitation.

8.2. Global Behavior

Figure 8-1 summarizes the global behavior of the infilled frame for increasing levels of excitation, showing normalized displaced shapes of the structure at the times of peak first story displacement. This figure gives preliminary indication that low-level excitations impose greater drift demand, relative to resistance, on the second story. The story drifts are about equal in each story, but the window openings in the upper walls make them more flexible and less resistant to drift-sensitive damage. Thus significant cracking in the second story occurred during the Taft 0.55g test, but not in the first story until the Taft 0.80g test. In the final test at 0.80g, the seismic demand on the lower walls exceeds their strength and rapid loss of stiffness allows for large first story drifts producing the “soft-story” response. These general observations will be borne out in more detail in the following sections on global behavior.

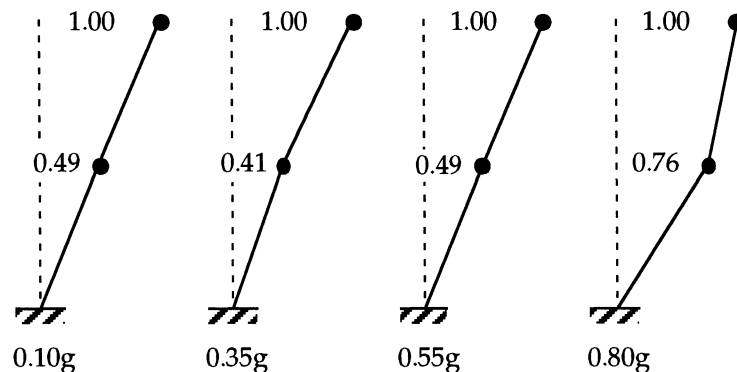


FIGURE 8-1 Normalized Deflected Shapes at Peak 1st Story Displacements

8.2.1. Story Hysteretic Relations

Figures 8.2 to 8.5 present the story drift-story shear relations for each test. The Taft 0.10g test showed little nonlinearity due to degradation and has been discussed in detail in Section 7.1. The Taft 0.35g and 0.55g tests show the typical low-level behavior of the specimen, where the first story carries more shear but drifts slightly less due to its greater overall stiffness than the second story. During the 0.55g level test, the second story was visibly damaged and its drifts reached nearly twice those of the first story in the positive direction.

The increase in hysteresis shown in the Taft 0.35g test, as compared to the 0.10g test, is evidence of minor damage sustained. Although no visible damage was found, it is suspected that some separation between frame and infill occurred. In Figure 8-6 two time histories of gap opening from the lower, west corner of the second story panel (DT32 in Figure 3-8) show symmetric fluctuation for the 0.10g test, but a definite gap-opening behavior for the 0.35g test. A large part of the fluctuation in the 0.10g time history may be experimental noise, as measurements are near the resolution limit of the displacement transducer (DCDT), although local tension and compression behavior without loss of bond also may be occurring. Similar gap behavior was observed at the lower, center corner of the panel (DT36). The beginning of separation of wall and infill cause the reduced story stiffness at small displacements shown in the hysteresis plots. Further possible sources of minor damage include microcracking in the masonry and concrete.

The Taft 0.55g test exhibits further nonlinearity due to more complete separation of frame and infill on both stories, and some masonry cracking, primarily in the second story. Gap instrumentation on the west walls measured clearly visible openings as large as 0.04 in at the upper center corner of the lower panel (DT31). Instrumentation showed other gaps peaking over 0.01 in. This more complete separation caused the small-displacement stiffness of the specimen to approach that of the bare frame.

To estimate the initial stiffness of each story, backbone curves are fit to the story drift-story shear relations of Figures 8.2 through 8.5. As discussed in Section 4.4.2, the shear building approximation allows for convenient isolation of the performance of each story in terms of the quantities of drift and story shear. The backbone curves relate story shear (SS) to drift (dr) by

$$SS = a_0 + a_1(dr) + a_2(dr)^2 + a_3(dr)^3. \quad (8.1)$$

The derivative of Eq. (8.1) evaluated at zero drift gives initial story stiffnesses, k_i^0 , equal to the coefficient, a_1 (Table 8-1). Figure 8-7 shows the linear estimates for stiffness at low drift levels. Separation of the infill from the bounding frame causes the initial, or low-drift, stiffness to approach that of

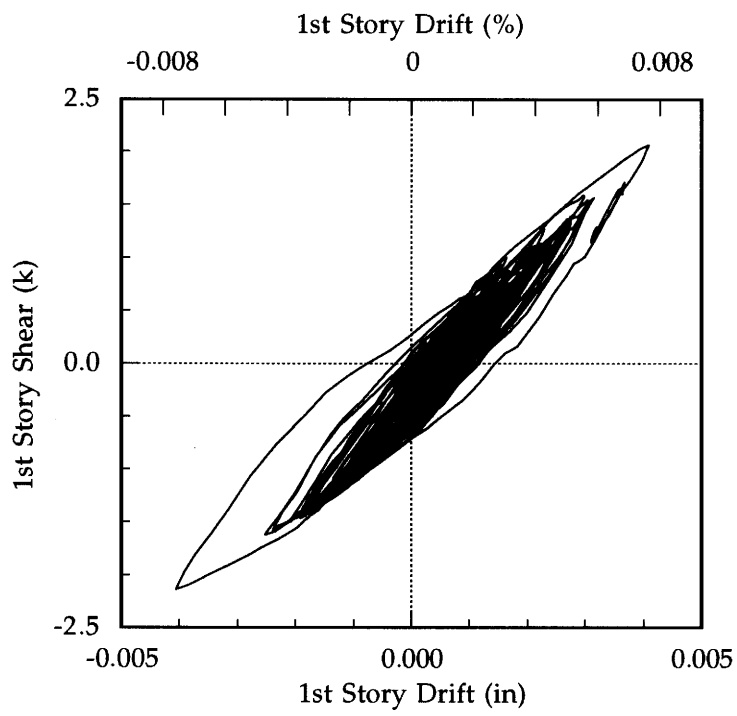
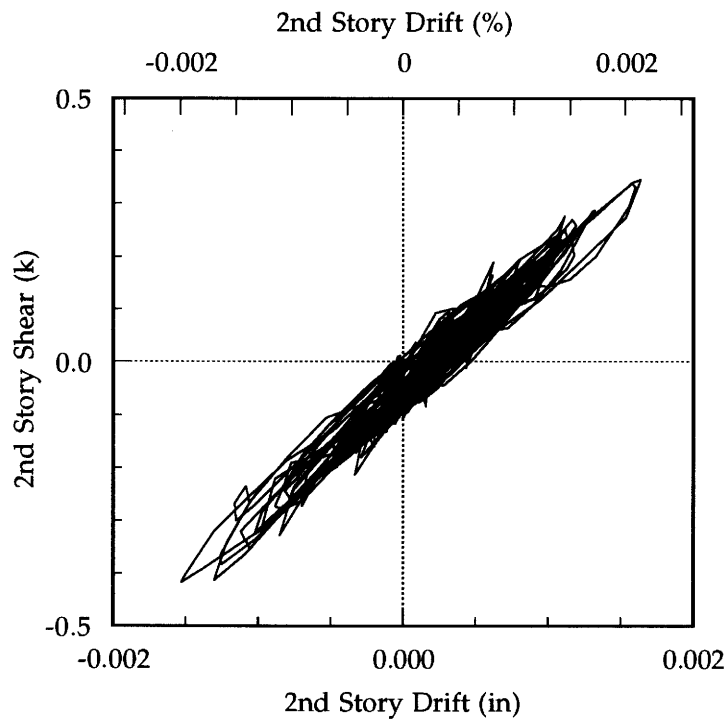


FIGURE 8-2 Taft 0.10g Story Hysteresis

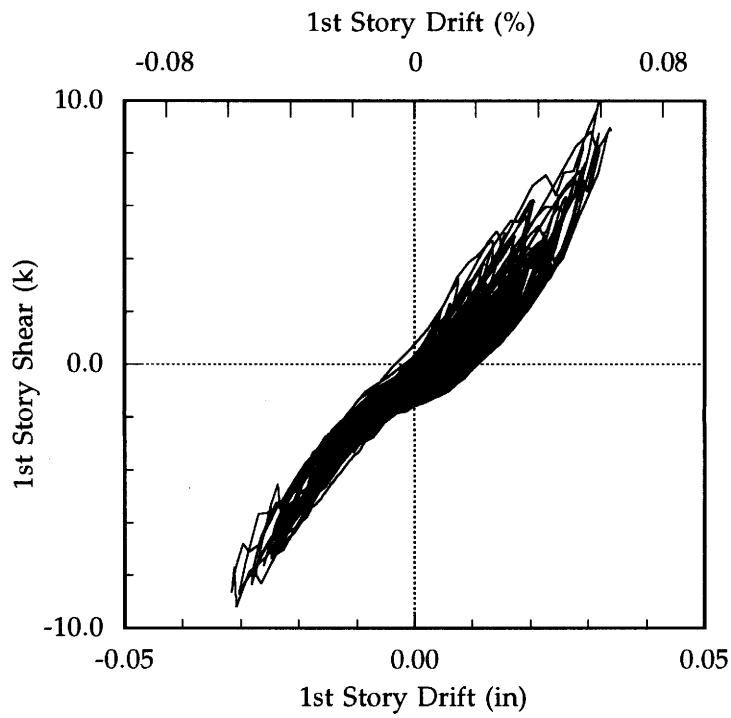
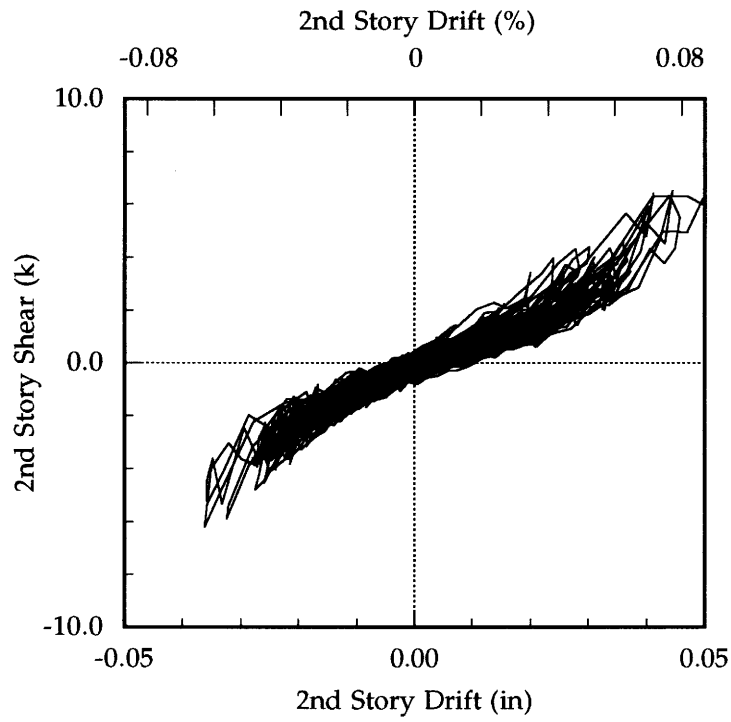


FIGURE 8-3 Taft 0.35g Story Hysteresis

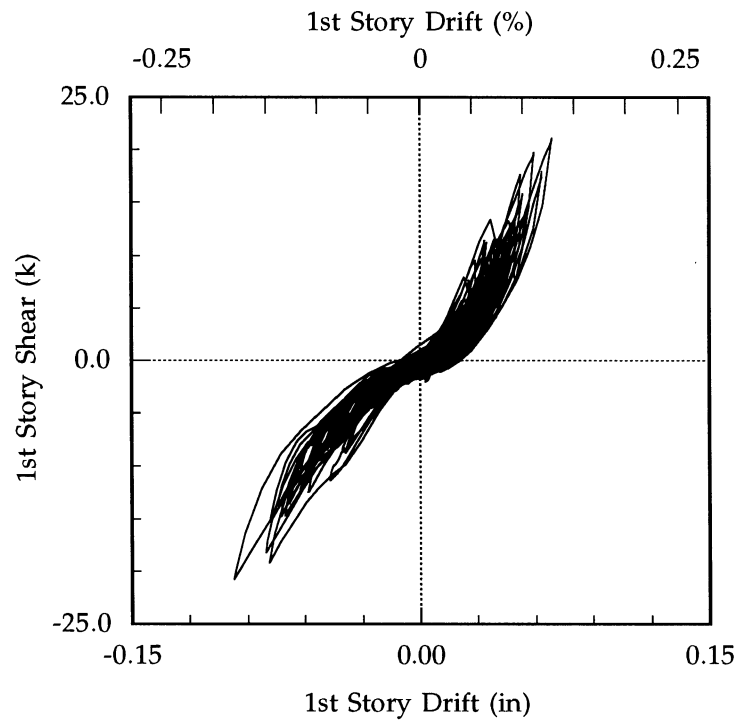
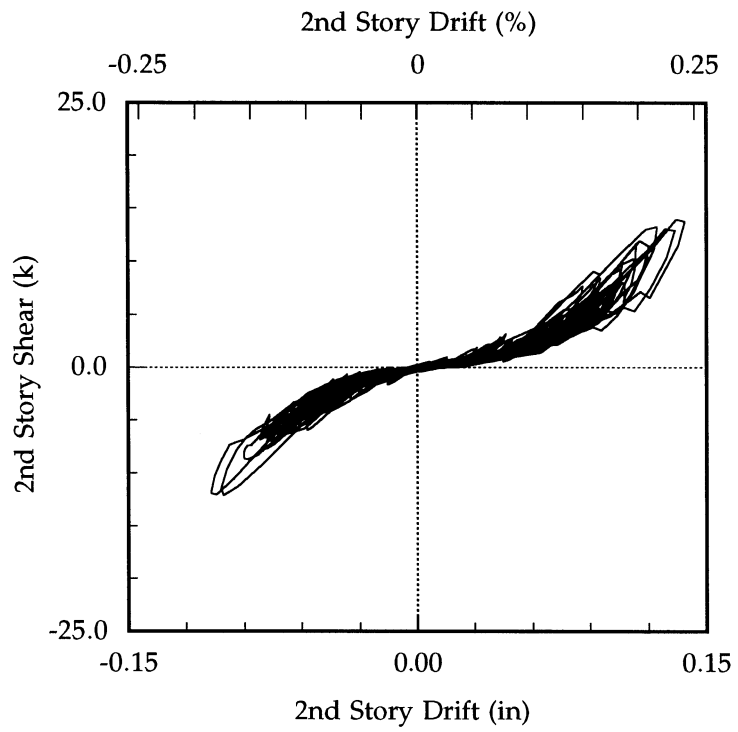


FIGURE 8-4 Taft 0.55g Story Hysteresis

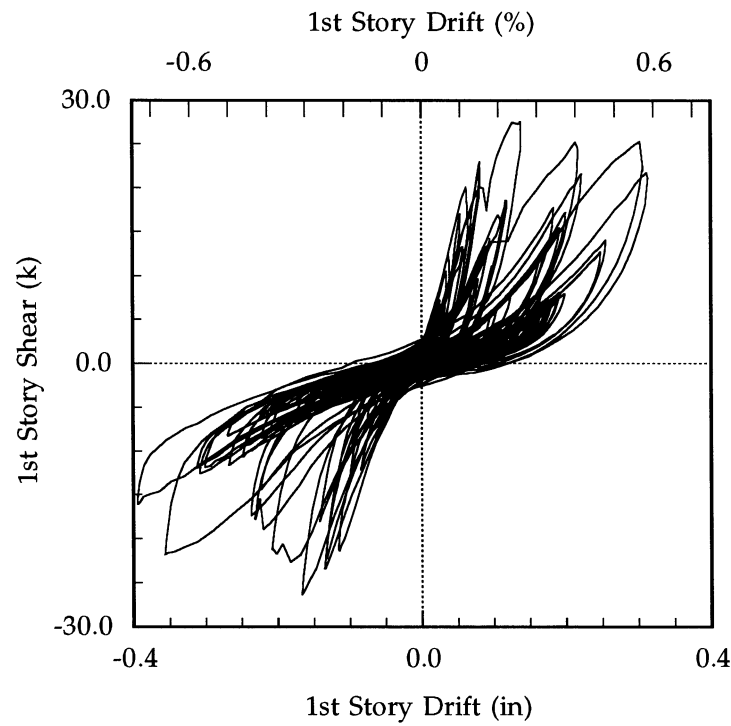
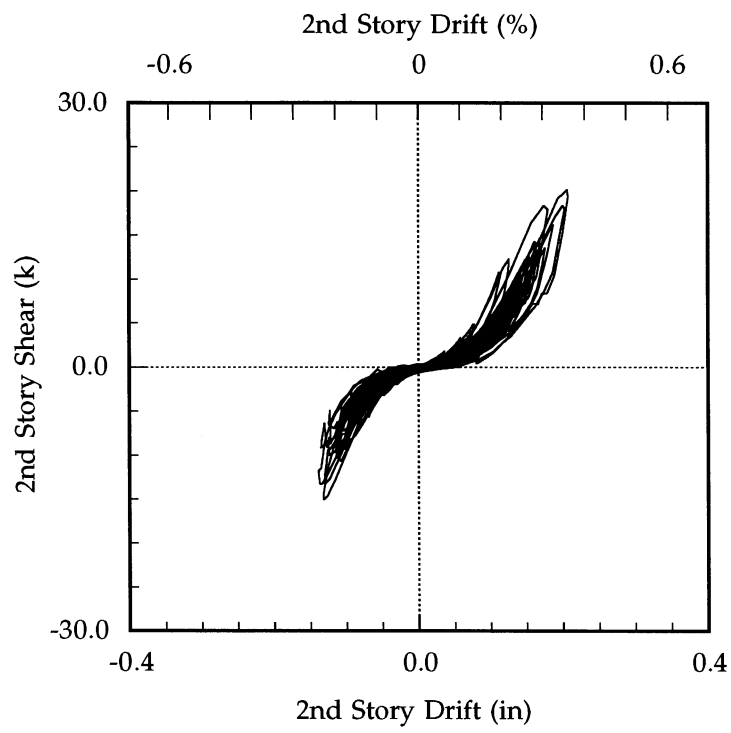


FIGURE 8-5 Taft 0.80g Story Hysteresis

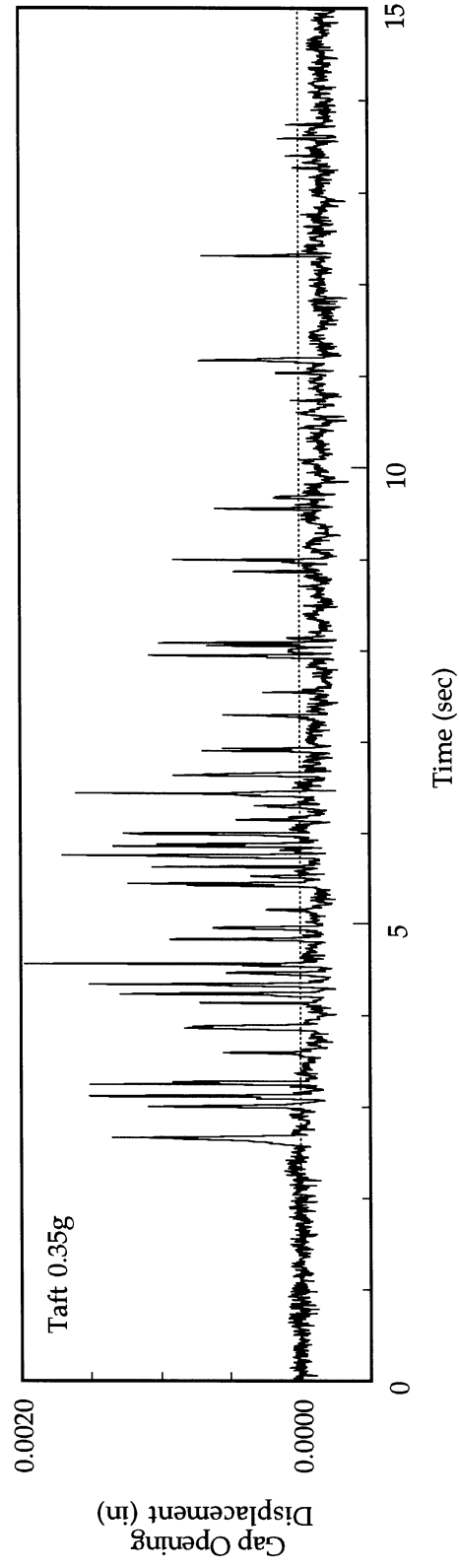
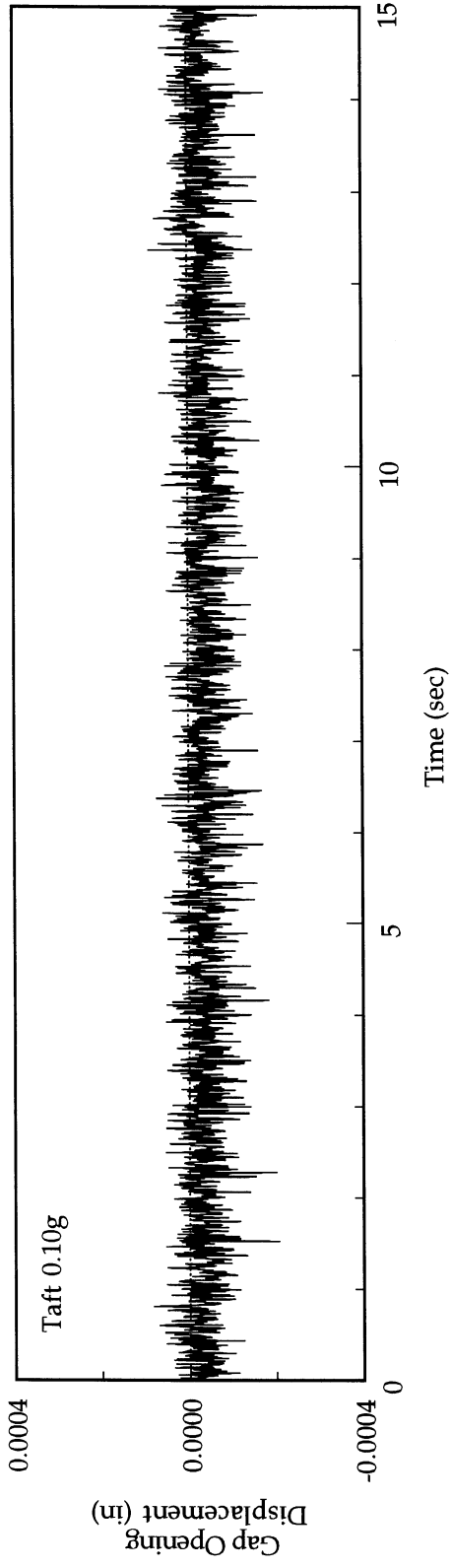


FIGURE 8-6 Gap Opening Displacement at DT32

the bare frame. For example in the Taft 0.55g test, the initial stiffness matrix may be estimated as

$$\mathbf{K}^0 = \begin{bmatrix} 146 & -29 \\ 29 & 29 \end{bmatrix} \text{ k/in,} \quad (8.2)$$

which is significantly less than that for the infilled frame in Eq. (4.15), and nearly equal to that for the bare frame in Eq. (4.3) especially in the second story. For the Taft 0.80g test (Figure 8-7) the second story stiffness falls below that of the bare frame as the excitation has caused some degradation in the frame itself. In the first story (Figure 8-7), the Taft 0.80g and bare frame initial stiffnesses are nearly identical. Although the first story frame has significant damage, some contact between frame and infill remains to offset that loss of stiffness in the frame. Once the structure has displaced sufficiently to close some length of the gap producing contact between the frame and infill, the stiffness will increase sharply due to the strut action induced in the infill, as seen in Figures 8.2 to 8.5 and in Eq. (8.1).

TABLE 8-1 Linear Estimates of Initial Stiffnesses

	1st Story	2nd Story
pga(g)	$a_1 = k_1^0$	$a_1 = k_2^0$
0.10	584	323
0.35	154	82.2
0.55	117	28.8
0.80	30.4	20.0

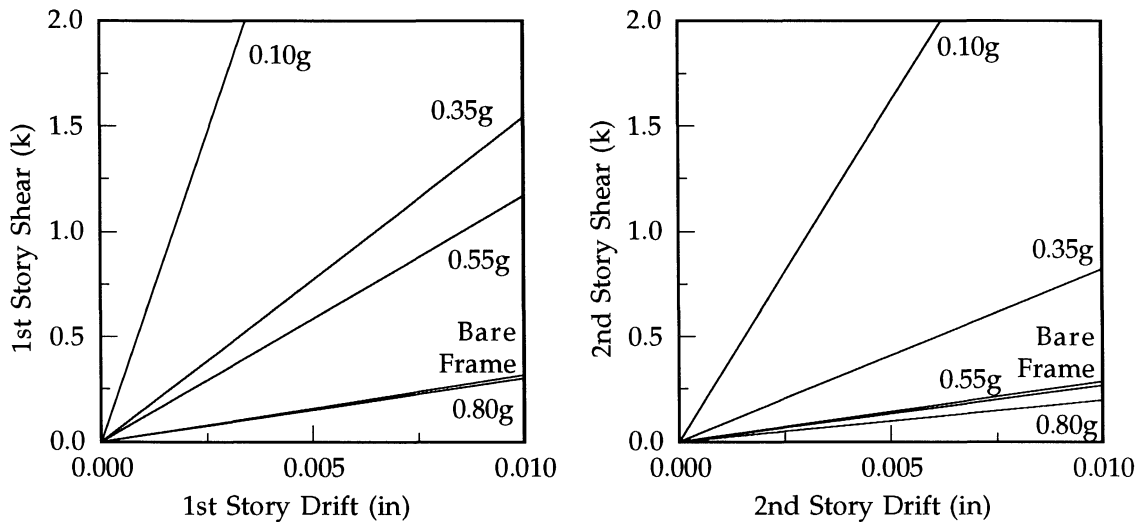


FIGURE 8-7 Linear Estimates of Initial Stiffnesses:

At the 0.55g level of excitation, cracking in the masonry also begins to contribute to degradation. In the second story, major diagonal cracks developed in both directions from window corners to panel corners (Figure 8-8). The majority of this cracking occurred relatively early in the record, before 5 sec, yet the second story continued to carry large story shears of about 12 k without excessive drift. The cracking stabilized after forming without ever producing excessive deformation or loss in strength (Figure 8-4). In the final test of Taft 0.80g, the second story hysteresis loops remained stable, accompanied by only minor additional cracking, and carried still greater story shear as high as 20 k (Figure 8-5). The first story, however, exhibited severe cracking (Figure 8-8) causing large increases in story drift from approximately 0.1 in to 0.3 in to carry story shears of about 25 k (Figure 8-5).

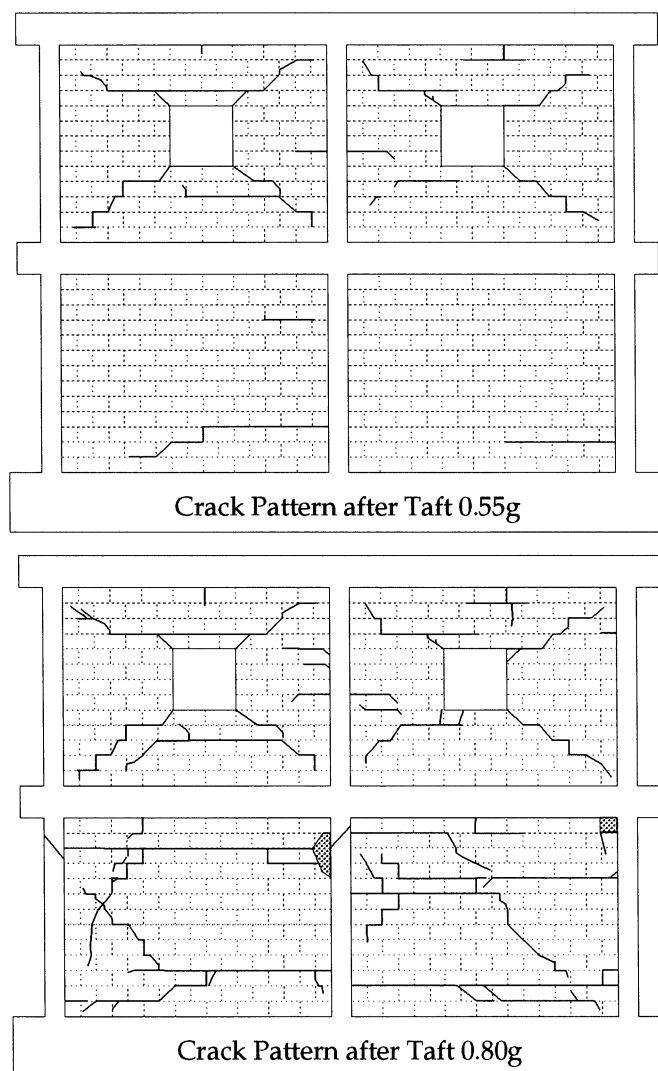


FIGURE 8-8 Final Crack Patterns

8.2.2. Energy Dissipation

The total energy balance for the structure may be written as

$$E_I = E_K + E_D + (E_H + E_S), \quad (8.3)$$

an analog of the equation of motion from Eq. (5.1) (Zahrah and Hall, 1984). The input energy imposed on the specimen by the earthquake

$$E_I = -\int_0^t \mathbf{v}^T \mathbf{M} \mathbf{a}_g dt \quad (8.4)$$

is balanced by kinetic energy

$$E_K = \int_0^t \mathbf{v}^T \mathbf{M} \mathbf{a} dt, \quad (8.5)$$

viscous damping energy

$$E_D = \int_0^t \mathbf{v}^T \mathbf{C} \mathbf{v} dt, \quad (8.6)$$

and the sum of hysteretic and strain energies

$$E_H + E_S = \int_0^t \mathbf{v}^T \mathbf{r} dt. \quad (8.7)$$

These energy expressions may be derived from the equation of motion by premultiplying by \mathbf{v} and integrating over time. Kinetic and strain energies are stored temporarily in the structure as it undergoes motion, while the damping and hysteretic energies are dissipated by the structure. The hysteretic energy, E_H , is equal to the area enclosed by each hysteresis cycle in the story shear-drift plots. With E_H calculated from the area of the hysteresis loops, the strain energy may be isolated by subtracting E_H from the sum in Eq. (8.7).

The hysteretic energy dissipation, E_H , may be considered a measure of material damage to the specimen. Figure 8-9, from the Taft 0.55g test, shows the typical cumulative hysteretic energy relation for each story. Table 8-2 lists the final hysteretic energy levels for each of the tests. Figure 8.10 normalizes the hysteretic energy of each story to the total, correlating the extensive damage in the first story walls during the Taft 0.80g with a sudden increase in relative hysteretic energy dissipation. Yet, despite significant cracking of the second story infill during the Taft 0.55g test, no significant changes in relative story hysteretic energy occurred.

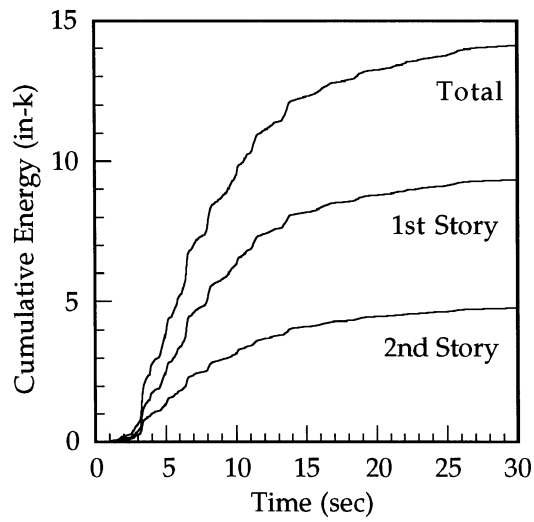


FIGURE 8-9 Taft 0.55g Story Hysteretic Energies

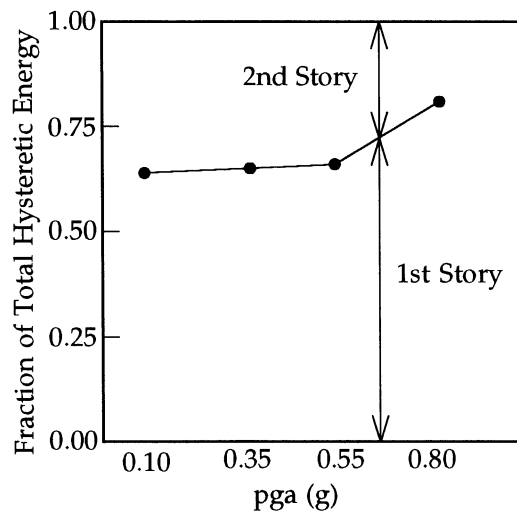


FIGURE 8-10 Normalized Story Hysteretic Energies

TABLE 8-2 Story Hysteretic Energies

pga(g)	Hysteretic Energy (in-k)		
	1st Story	2nd Story	Total
0.10	0.037	0.021	0.059
0.35	2.31	1.22	3.53
0.55	9.3	4.8	14.1
0.80	51.4	11.7	63.1

The hysteretic energy comprises only one part of the total energy stored and dissipated by the structure during excitation. Cumulative time histories of each energy term are shown in Figures 8.11 to 8.14. Note that strain and kinetic energies are very nearly zero at the end of the earthquake motion. For Taft 0.10g in Figure 8-11, the drift of strain energy from zero is due to thermal effects on the experimentally measured values of restoring force; it does not affect the overall nature of the graph.

Figure 8-15 shows the final values of total, hysteretic and viscous damping energies as a function of applied pga, and Table 8-3 lists the numerical values. The total dissipated energy increases rapidly with pga. This in itself is not unusual since even for a linear elastic structure with constant C and K , by Eqs. (8-6) and (8-7), dissipated energy should increase proportional the square of pga. Figure 8-15 normalizes the damping and hysteretic energies to the total dissipated energy. The onset of significant damage in the second story during the 0.55g test causes an increase in the damping fraction of energy. Significant first story damage during the Taft 0.80g test then causes an increase in hysteretic energy fraction. Whereas Figure 8-10 showed a clear relationship between story hysteretic energy dissipation and observed damage, a similar relationship is not evident here between observed damage and changes in relative amounts of damping and hysteretic energy dissipation.

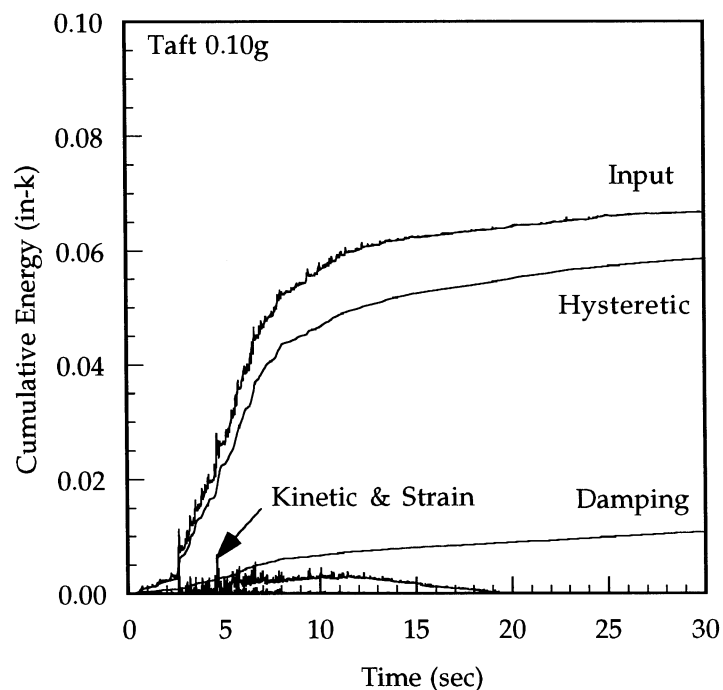


FIGURE 8-11 Taft 0.10g Energy Components

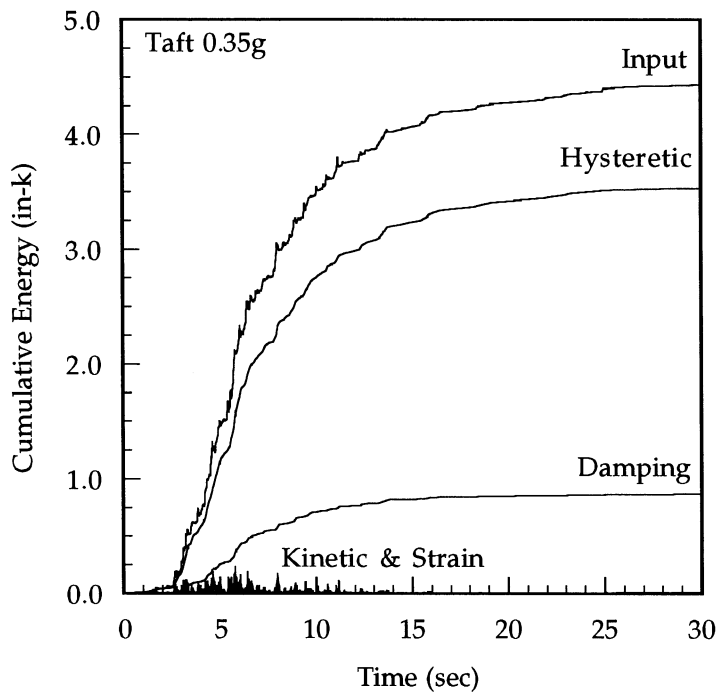


FIGURE 8-12 Taft 0.35g Energy Components

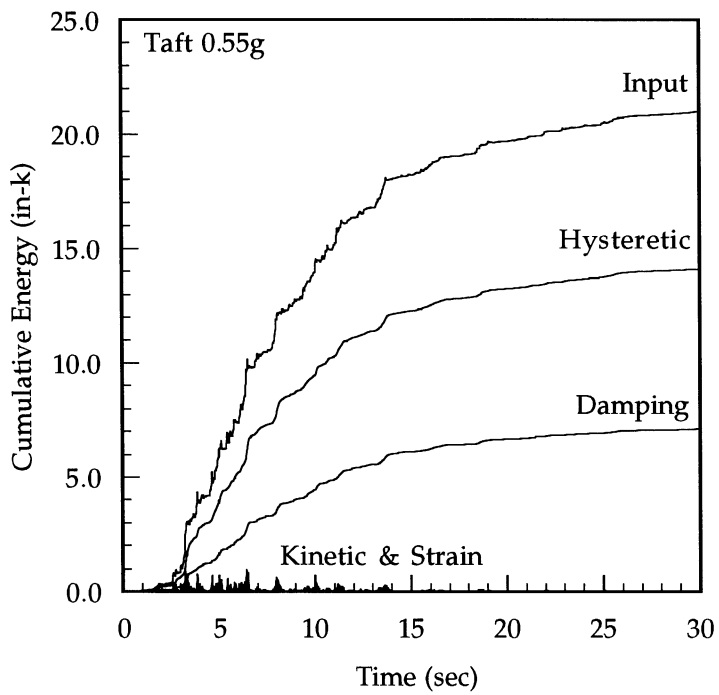


FIGURE 8-13 Taft 0.55g Energy Components

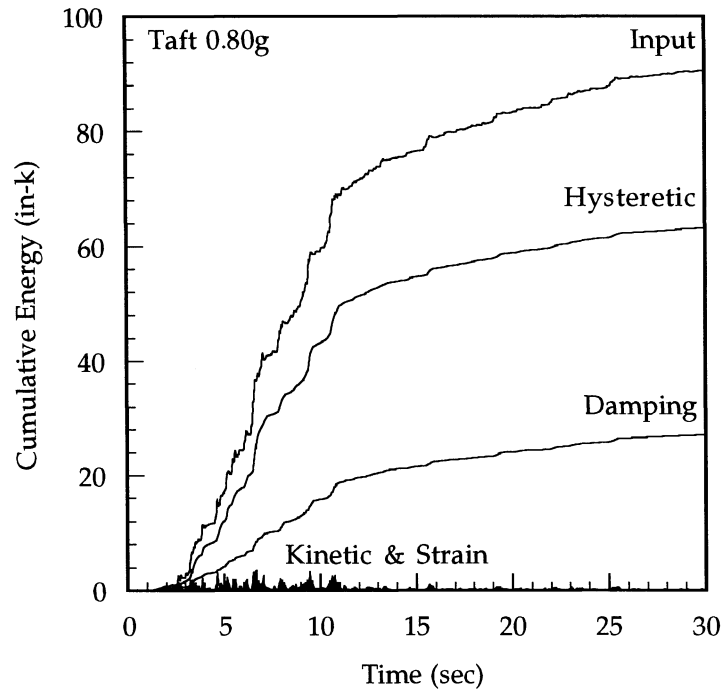


FIGURE 8-14 Taft 0.80g Energy Components

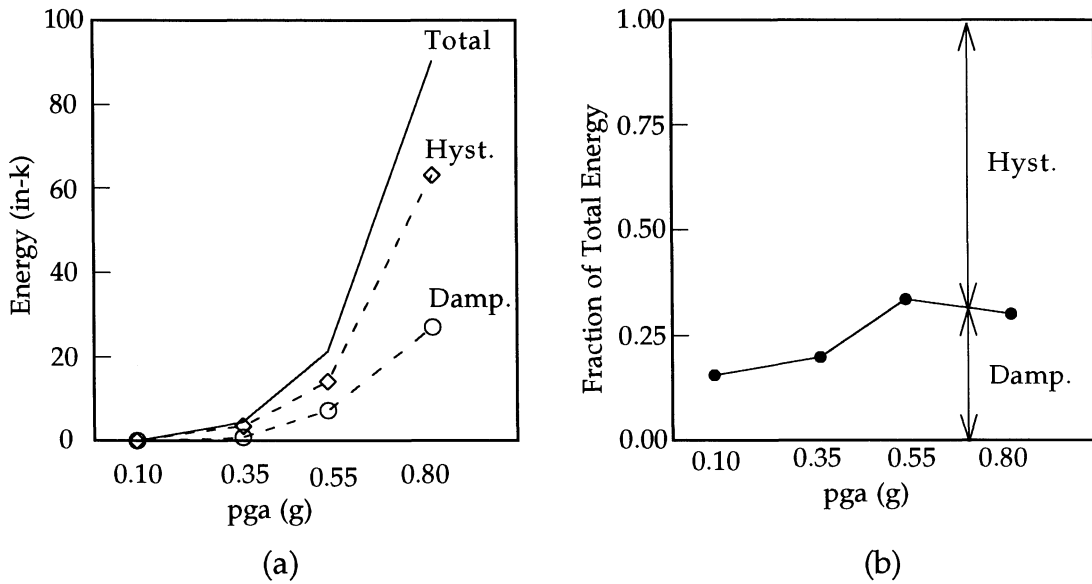


FIGURE 8-15 Dissipated Energy:
(a) Energy Increase with pga
(b) Normalized Hysteretic and Damping Fractions

TABLE 8-3 Dissipated Energy

pga(g)	Energy (in-k)		
	Damping	Hysteretic	Total
0.10	0.011	0.058	0.069
0.35	0.87	3.53	4.40
0.55	7.1	14.1	21.2
0.80	27.1	63.1	90.2

8.2.3. Frequency Spectra

A final measure of global behavioral change over the testing sequence can be seen from the predominant frequencies of motion in displacement time histories. Figure 8-16 compares the first story time histories from Taft 0.10g and 0.80g tests; note the 1 to 50 difference in the displacement scale for readability. The higher level test clearly tends to oscillate in a lower frequency range due to its decreased stiffness. A complete set of story displacement and force time histories appears in Buonopane (1997).

The frequency content can be calculated through the fast Fourier transform (FFT). Figure 8-17 compares frequency spectra corresponding to the time histories of Figure 8-16, clearly demonstrating the shift towards lower frequencies. Although the nonlinearity in the Taft 0.80g response prevents definition of specific modal frequencies, almost all the motion is contained below 5 Hz whereas the Taft 0.10g response contained significant motion near 14 Hz. Recall from Section 6.1 that 13 Hz and 28 Hz were the expected modal frequencies, and from Section 8.2 that the qualitative displaced shape of the structure was almost entirely first mode.

Frequency spectra may also be used to trace the stiffness degradation during a single test. Figure 8-18 shows first story displacement spectra based on the initial and final 1024 sample points (about 3.6 sec) of the Taft 0.80g response. Again the shift toward lower frequencies reveals stiffness degradation of the specimen. The smoother spectra here are due to the lower frequency resolution of the FFT with 1024 samples as compared to the nearly 8500 represented in Figure 8-17.

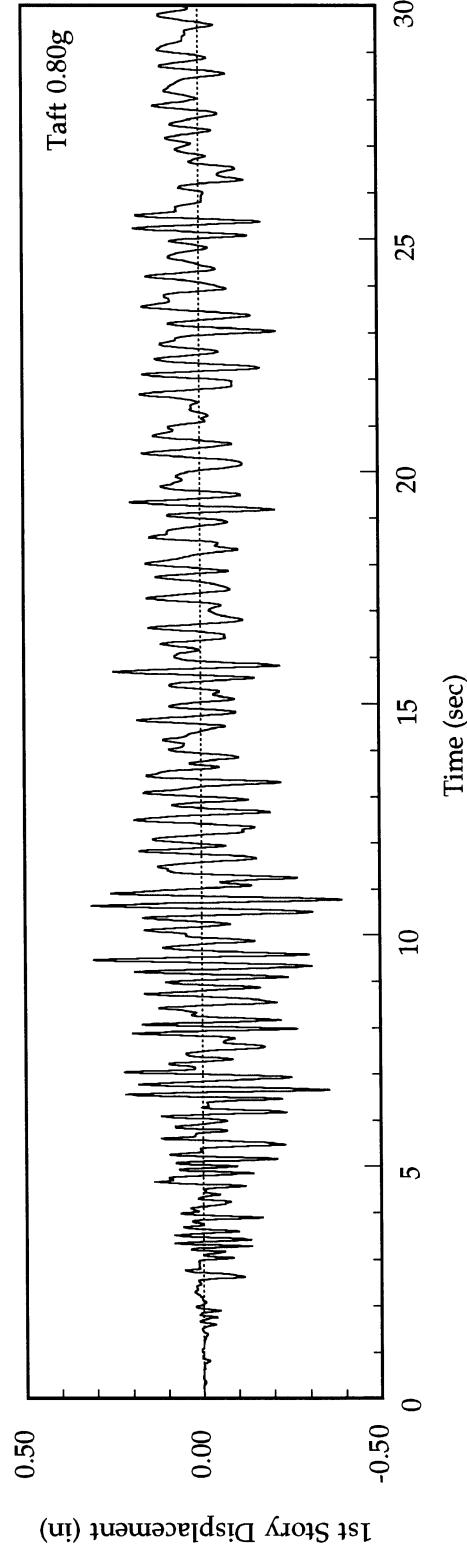
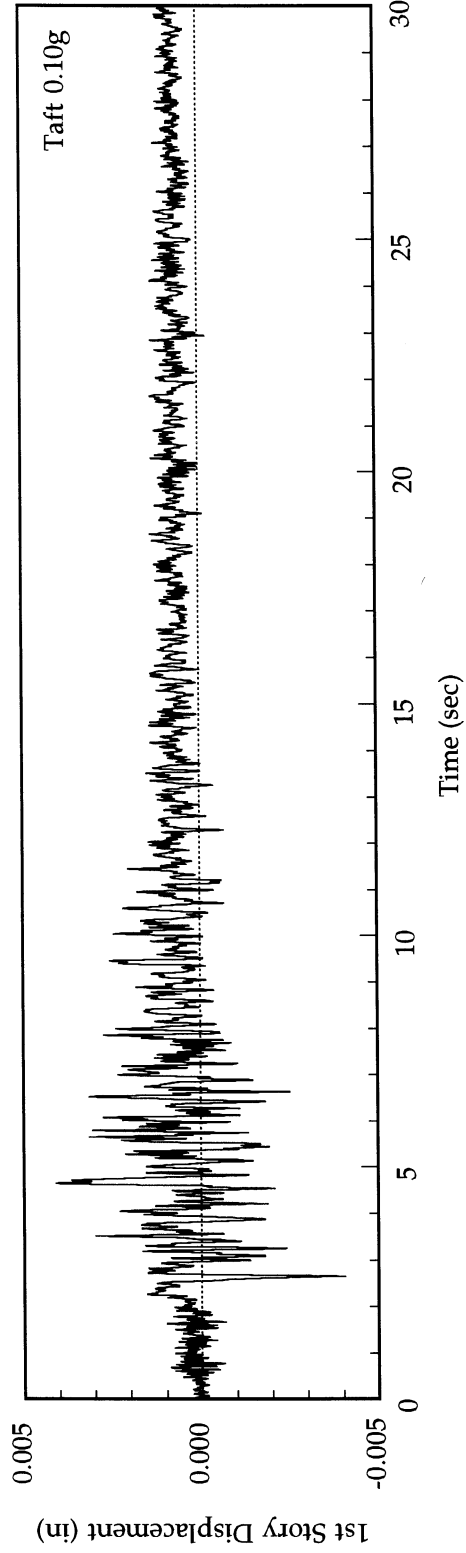


FIGURE 8-16 1st Story Displacements: Taft 0.10g and Taft 0.80g

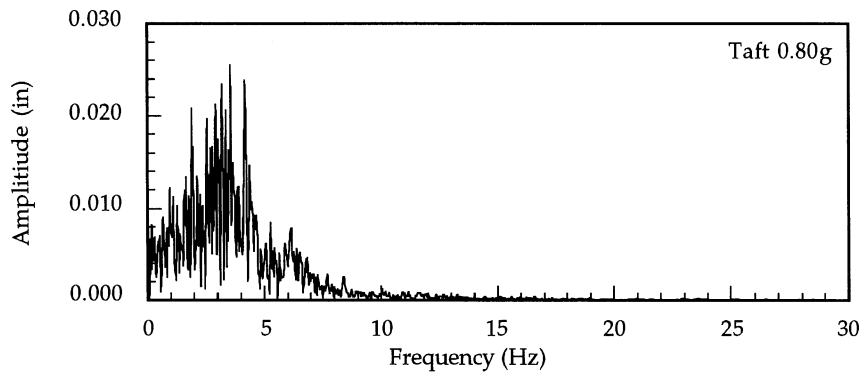
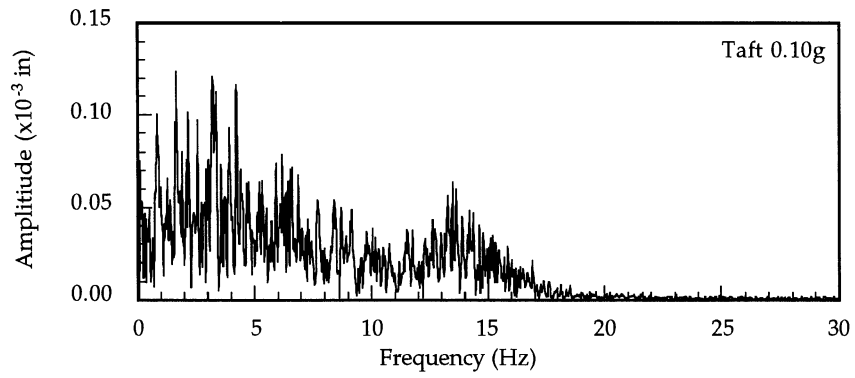


FIGURE 8-17 1st Story Displacement Frequency Spectra

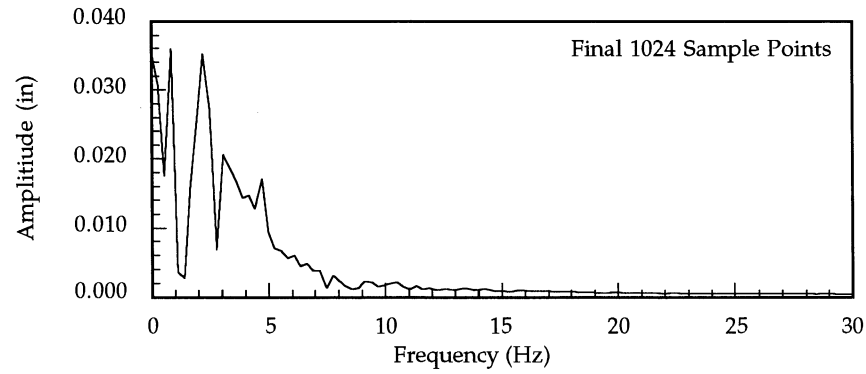
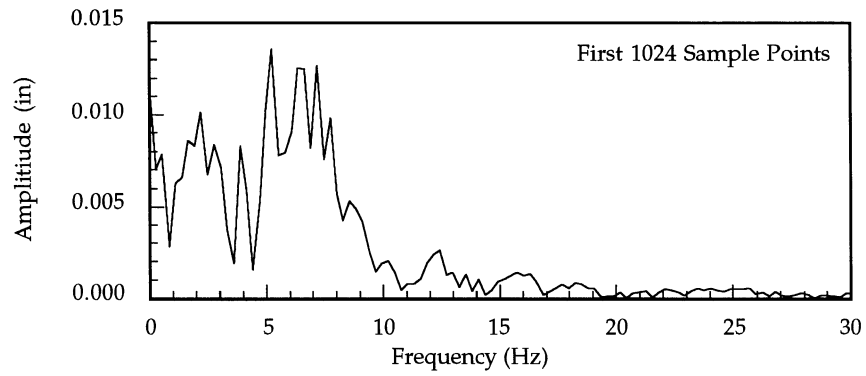


FIGURE 8-18 Taft 0.80g 1st Story Displacement Frequency Spectra

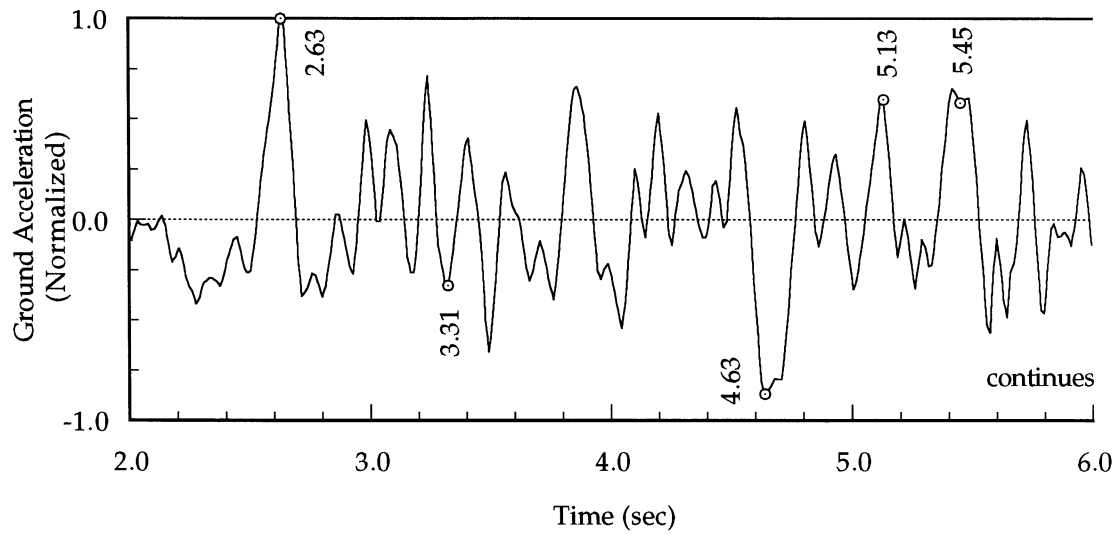
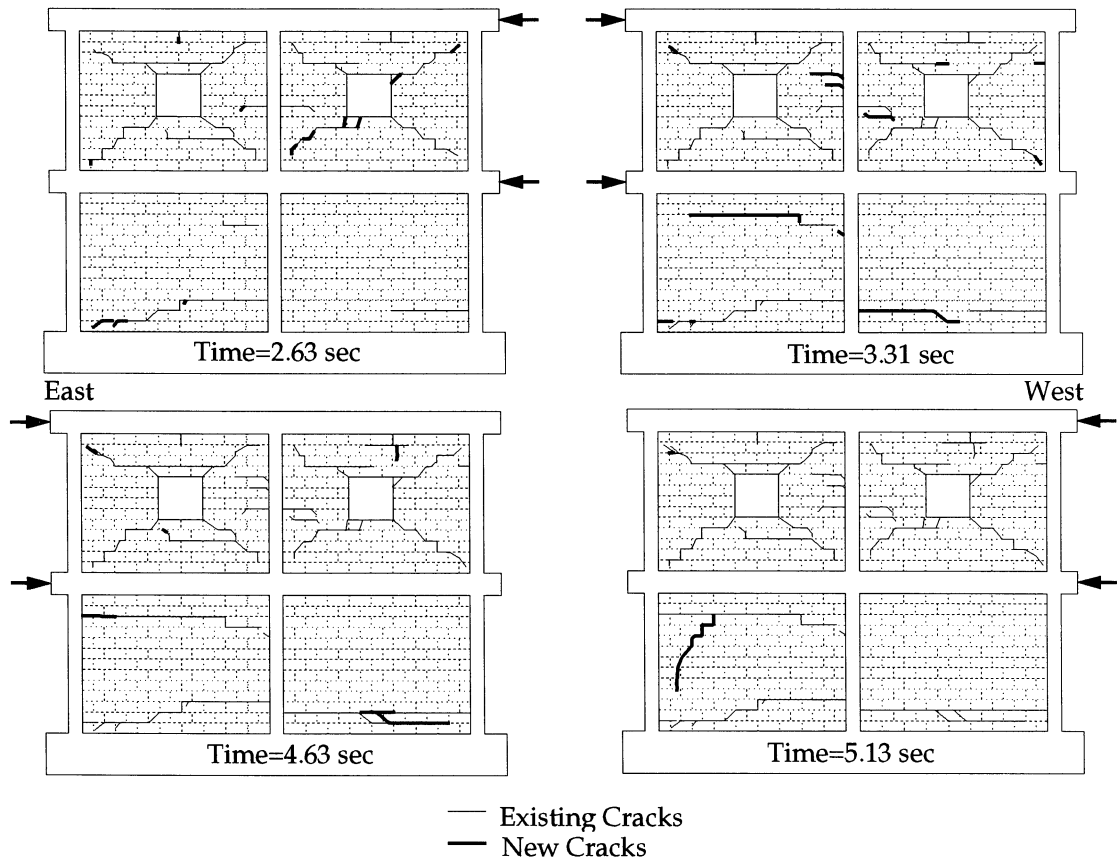
8.3. Masonry Crack Development

A brief study of the masonry cracking provides a convenient bridge between aspects of global and local behavior, for it is the cracking which causes overall losses in stiffness and strength described in the previous section, as well as leading to drastic changes in local behavior within elements of the frame and infill. The final crack patterns resulting from the Taft 0.55g and 0.80g tests are shown in Figure 8-8. Attention here will be focused on the Taft 0.80g test for which Figure 8-19 presents the history of crack propagation with the associated earthquake ground acceleration record. The first story shear-drift plot in Figure 8-20 shows the peak hysteresis loops also keyed by time to the earthquake ground acceleration record.

The first, and largest, peak of the ground motion occurs at 2.63 sec yet causes no major damage to the specimen, only minor extension of existing cracks in both the upper and lower stories. The first major shear failure of bed joints occurs at 3.31 sec. The shear-drift plot shows a significant drop as the bed joint fractures and slips and then, once the slip is limited by the bounding frame, a continued increase in load beyond the point of original cracking. Another large bed joint failure occurs at 5.45 sec in the lower west panel with similar associated response reflected in the shear-drift plot.

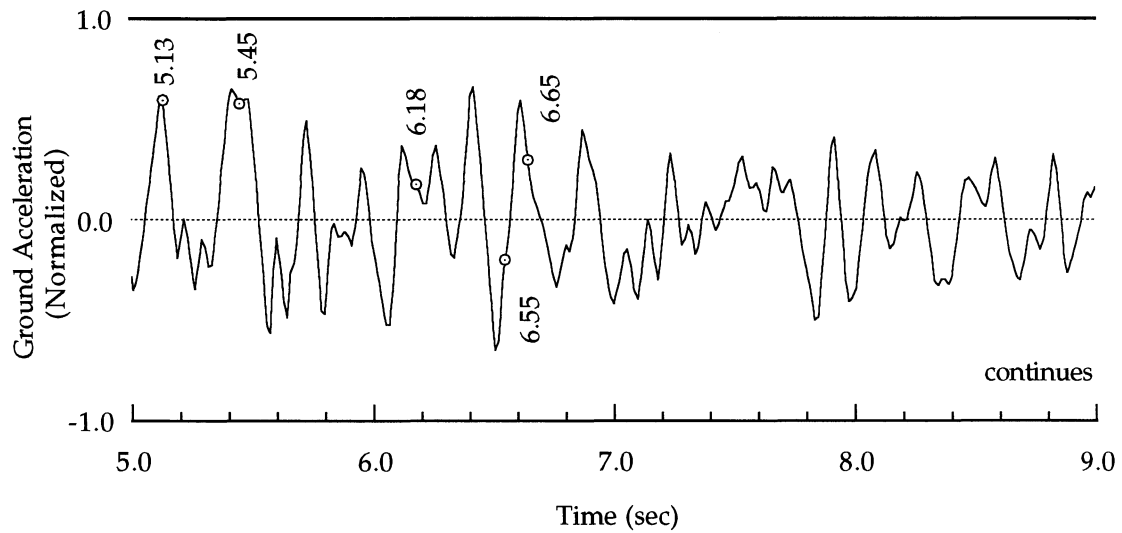
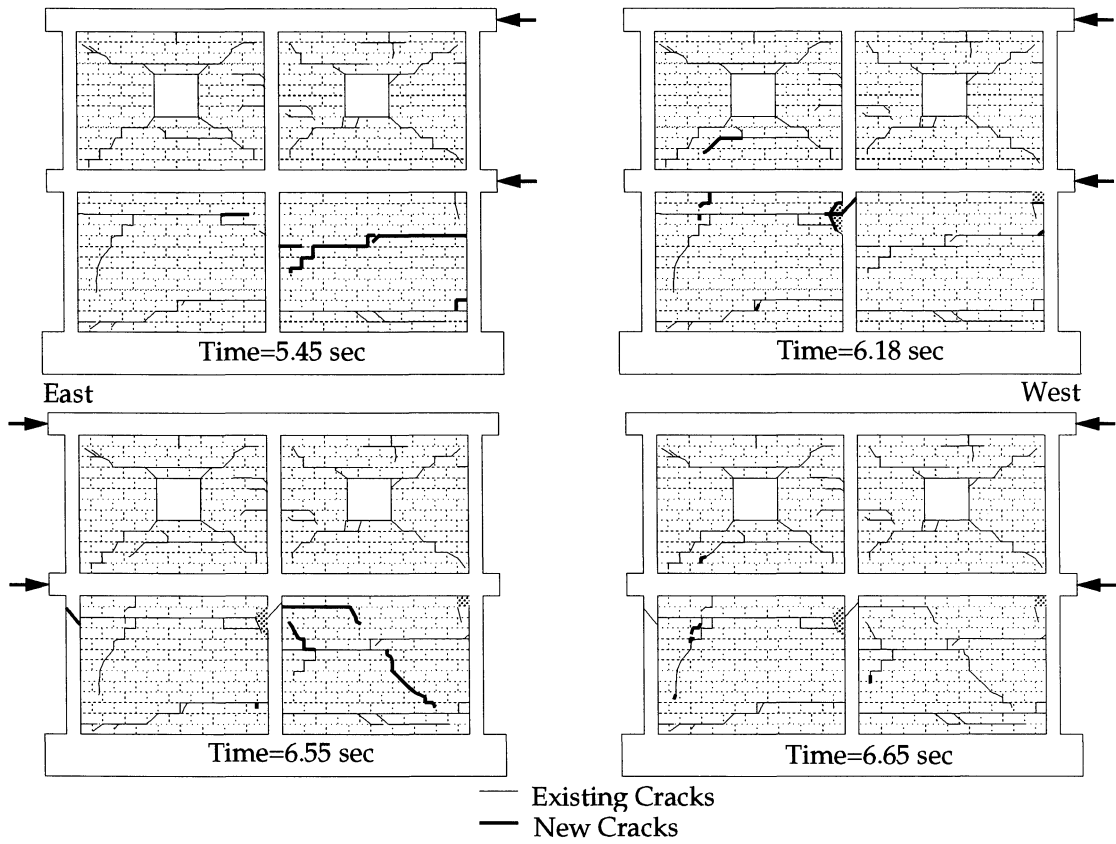
At 6.18 and 6.55 sec the center and east columns, respectively, crack in shear. The peak near 6.18 sec spalled parts of two masonry blocks adjacent to the center column, thus forming a complete bed-joint slip plane below the second course from the top in the lower east panel. The east column then cracks in shear at 6.55 sec, immediately after the next large ground motion in the opposite direction.

Other minor occurrences of cracking do not produce such noticeable effects in the shear-drift plot but contribute to the gradual accumulation of damage, causing significant seismic demand during later portions of the ground record. For instance, the local peak at 9.44 sec (about 70% of the pga) results in a drift demand of 0.3 in, only slightly less than the maximum for the entire record. The story shear demand of about 25 k also remains close to the maximum. Similar observations may be made for the 6.65 sec peak in the opposite direction. As the structure softens due to the accumulated damage, the peaks in the story-drift behavior tend to lag behind the peaks of the input motion, at 10.76 sec for example. This lag may be attributed to the larger inertial forces associated with the softened, more flexible, structure which develops story accelerations large enough to have greater influence in the equation of motion than the ground accelerations.



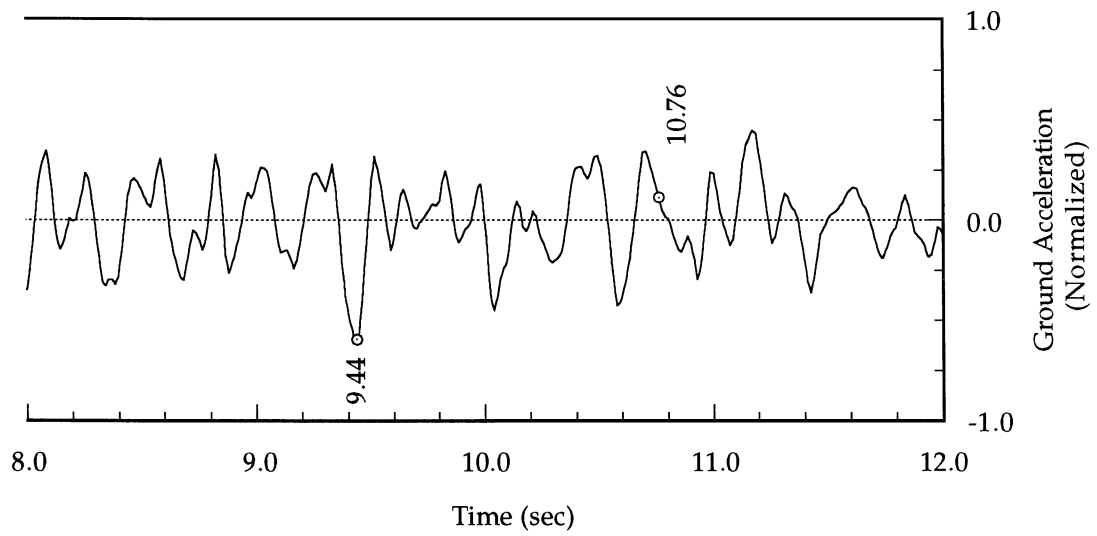
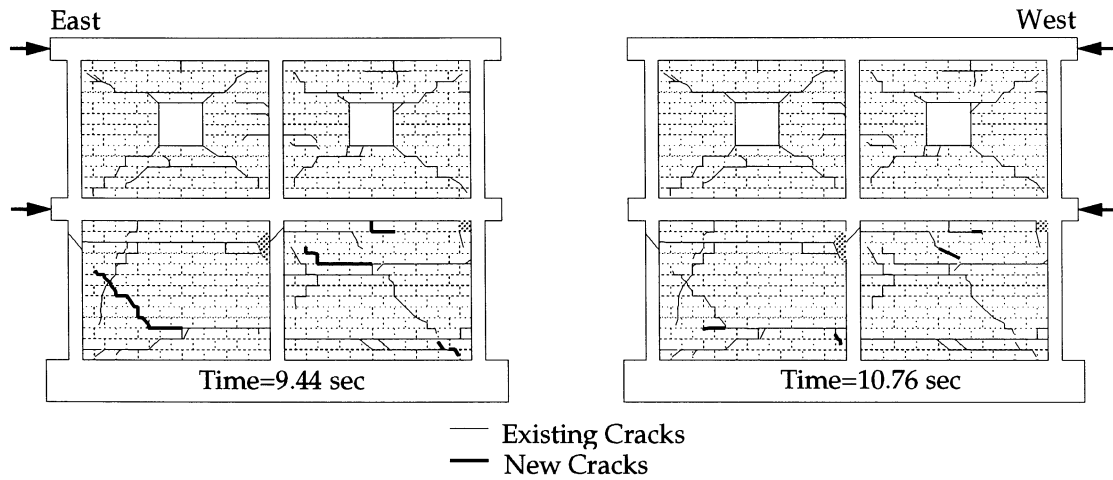
**FIGURE 8-19 Taft 0.80g Crack Development:
(a) 0.00 sec to 5.13 sec**

Figure 8-19 (Continued)



(b) 5.45 sec to 6.65 sec

Figure 8-19. (Continued)



(c) 9.44 sec to 10.76 sec

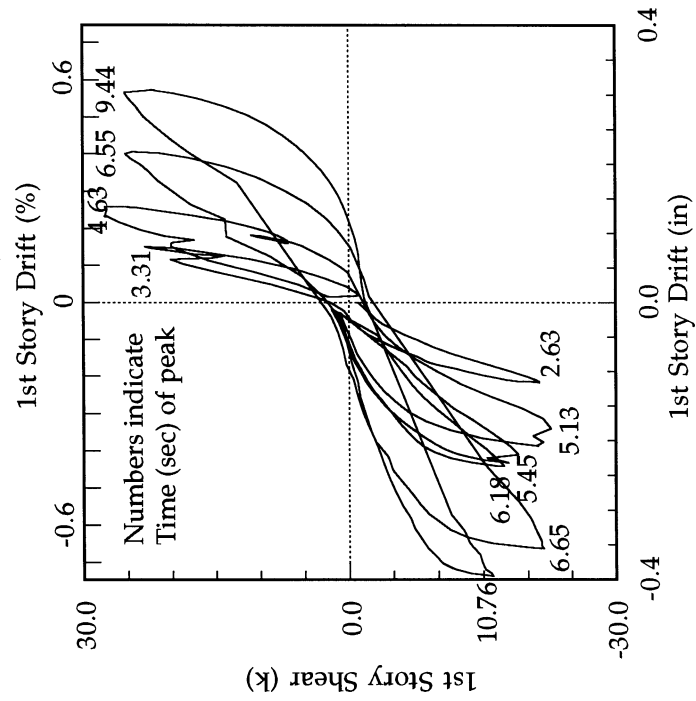
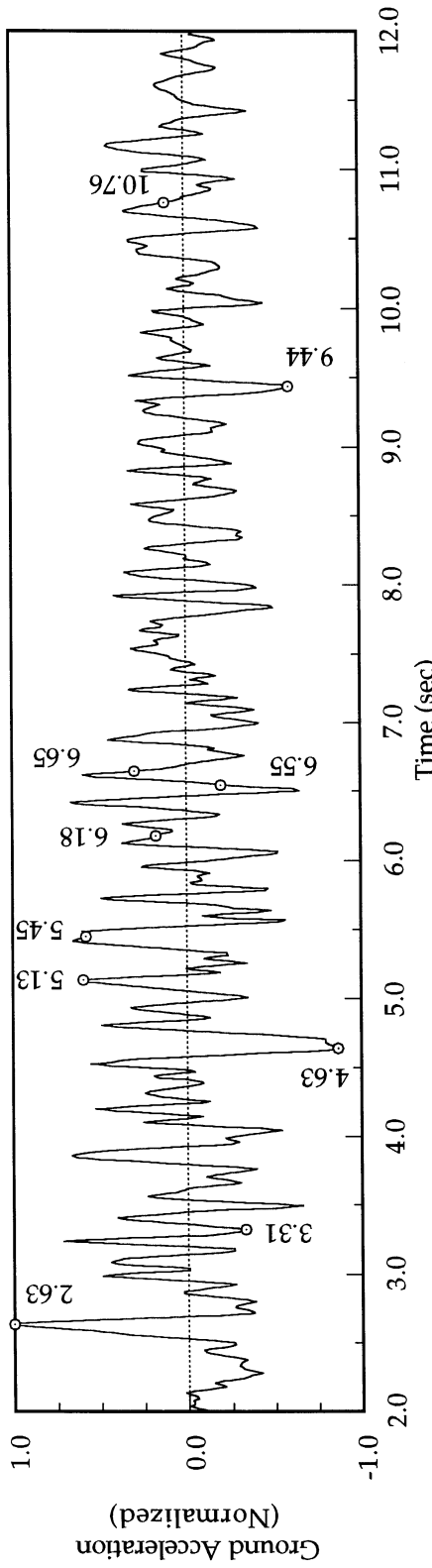


FIGURE 8-20 Taft 0.80g 1st Story Hysteresis

8.4. Local Behavior Critical Event Series

In order to focus examination of local specimen behavior it is convenient to identify representative peak occurrences from each test. One series of events is based upon maximum base shear; the other, upon maximum first story displacement. Tables 8-4 and 8-5 identify the time of occurrence of each of these events and associated story displacements and restoring forces. Other possible peak events may be identified, but most plausible event series will be composed of some combination of times from those in Tables 8-4 and 8-5. For instance, peak second story drift occurs at times of 4.64, 5.81, 6.52 and 4.66 sec for increasing pga from 0.10g to 0.80g. Note also that events in Tables 8-4 and 8-5 are chosen based on peak magnitude, the actual event direction (east or west) indicated by the presence or absence of a negative sign.

TABLE 8-4 Maximum Base Shear Series

pga (g)	Time (sec)	Story Displacement (in)		Story Force (k)	
		1st	2nd	1st	2nd
0.10	2.65	-0.0041	-0.0077	-1.22	-0.92
0.35	4.63	0.0318	0.0760	7.49	2.41
0.55	6.52	0.0689	0.1897	14.48	6.60
0.80	4.66	0.1384	0.3170	19.16	8.43

TABLE 8-5 Maximum First Story Displacement Series

pga (g)	Time (sec)	Story Displacement (in)		Story Force (k)	
		1st	2nd	1st	2nd
0.10	4.64	0.0041	0.0084	1.10	0.97
0.35	5.81	0.0339	0.0835	2.69	6.21
0.55	6.44	-0.0974	-0.1989	-12.06	-8.68
0.80	10.76	-0.3947	-0.5170	-7.34	-8.74

8.5. Infill-Frame Interaction

8.5.1. Maximum Base Shear Series

Moments and axial forces are computed from the strains recorded by pairs of gages mounted on the reinforcing steel. Material properties from Section 2.2, and the Todeschini stress-strain concrete model (MacGregor, 1988) are used to compute forces. A typical set of strain time histories from Taft 0.80g appears as Figure 8-21.

Figures 8-22a–d show moment and axial force diagrams for the maximum base shear series. Moments and axial forces are shown as percent of capacity, M_n or P_n , where M_n refers to the moment capacity at zero axial force and P_n the pure compression capacity. Complete interaction diagrams have been previously given in Figure 1-4. Moment diagrams are drawn on the tension side, and positive percentages of axial capacity indicate tension. True force magnitudes are indicated by the inset scales. Values of story displacements are given at the center column of the moment diagrams. Story forces are indicated by the arrows at the left-hand side of the figures. For visual comparison of these peak internal force diagrams across different pga levels, the diagrams have been oriented so that the story forces always appear on the left, although the true direction of load application may have been east or west, as indicated by the captions in the figures.

In the second story, the columns on the loaded side (LS) consistently exhibit the largest moments and a reversal of sign at the mid-height location. The relatively large slope of the moment diagram over the upper half of the column suggests a substantial shear force on the column due to interaction of the frame and infill. Such a shear force would be caused by the formation of a compressive strut originating near the loaded corner of the panel and inclined to pass below the window opening. Figure 8-23 suggests a possible strut mechanism which produces reversing curvatures consistent with those implied by the measured moments in the second story LS column. Note that the maximum moment occurs in the upper half of the column and may be significantly greater than that measured at mid-height. Also the distribution of interaction force is likely somewhat more complicated than the assumed uniform distribution, so many other possible moment diagrams exist. More experimental measurements of column moments or direct measurement of interaction bearing pressure would be needed to define more accurately the nature of the interaction force between frame and infill.

The off-diagonal strut mechanism shown in Figure 8-23 is similar to effective secondary struts previously proposed by Mainstone (1971) and Mander et al. (1993) to model infill walls without openings, but in which severe main diagonal compressive strut damage has occurred near the center of the panel. Here the window opening causes the formation of the struts along the off-diagonals even in the undamaged panel.

The formation of the effective strut is also supported by the presence of relatively uniform axial tension in the second story LS column, caused by the vertical component of force from the effective strut. At the first story column the axial force is substantially increased by the addition of induced tension from strut action in the first story panel. At the bottom of the first story loaded side column, axial tensions are large, while moments are small. After the beginning of separation of the infill and frame during the Taft 0.35g test

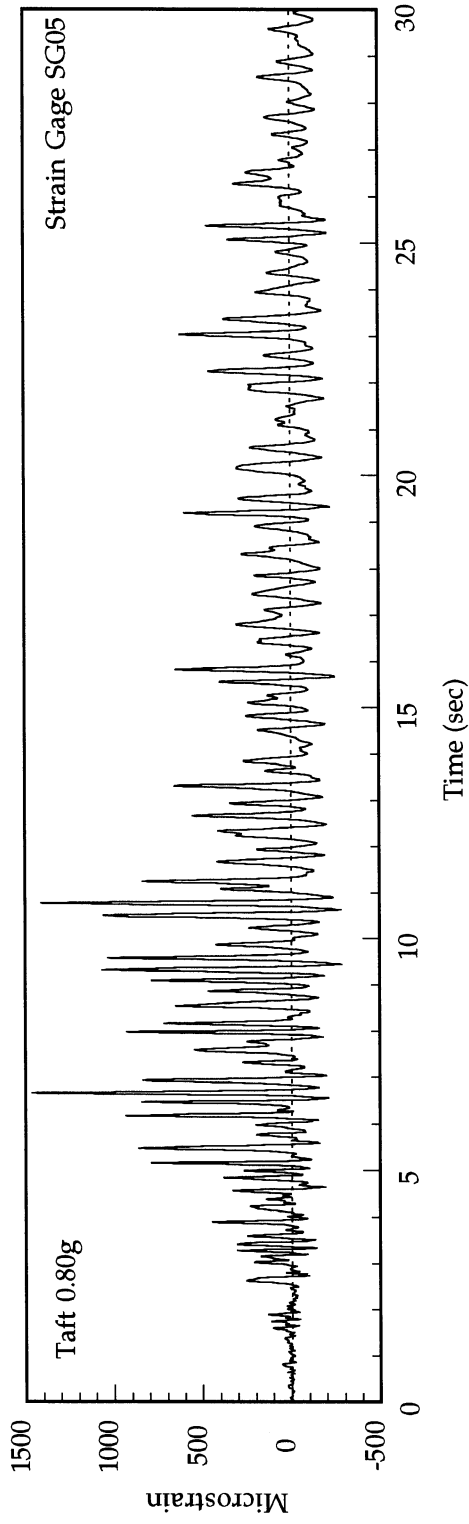
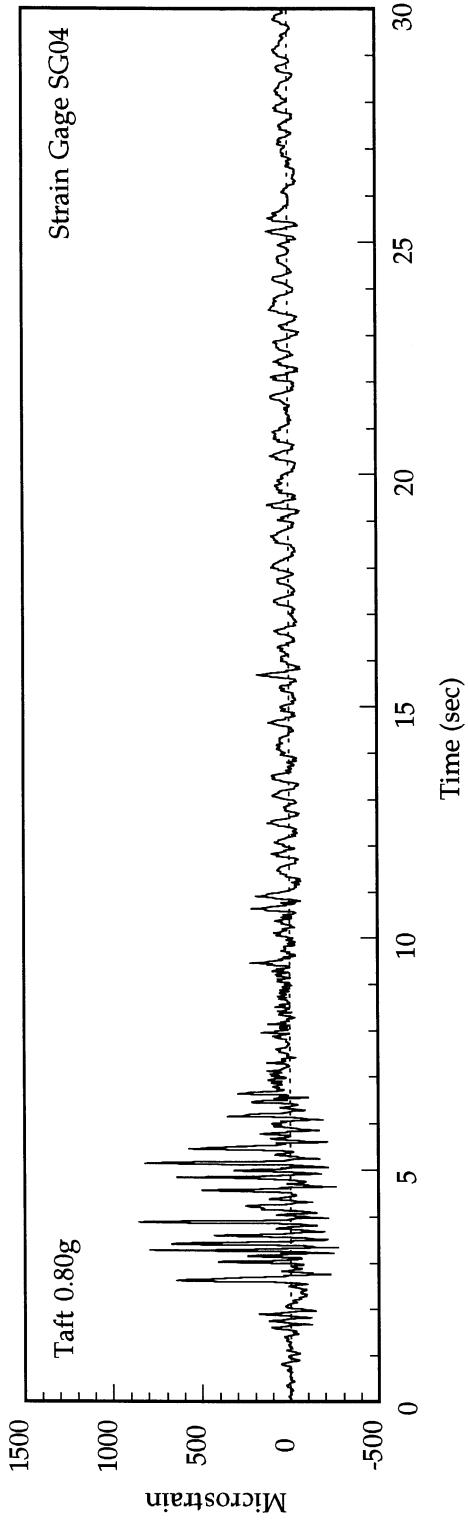
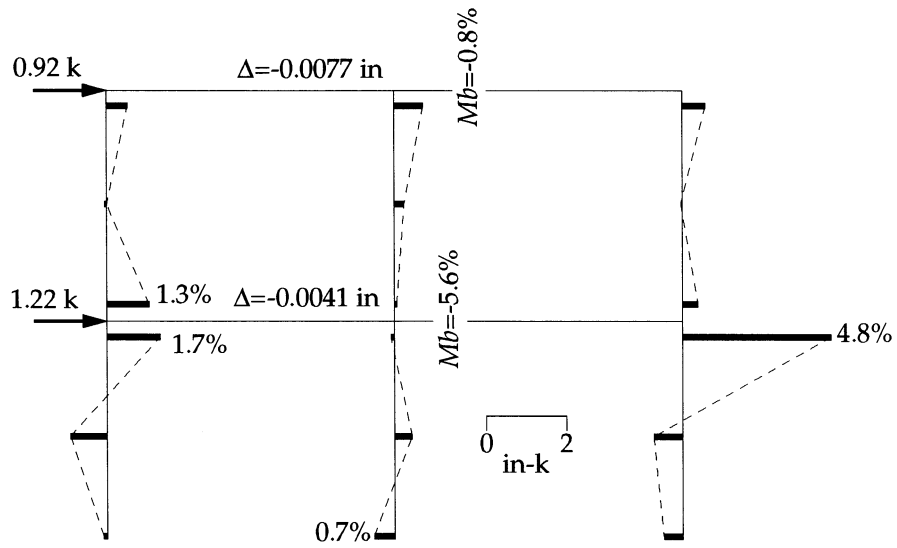


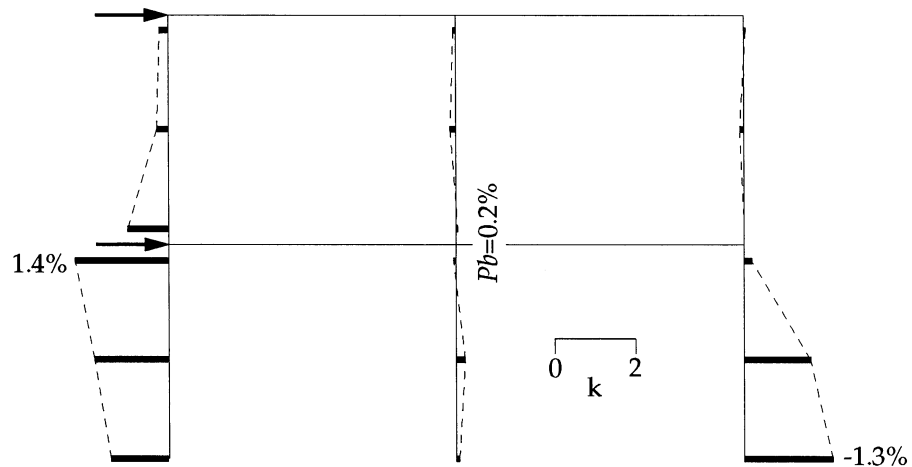
FIGURE 8-21 Taft 0.80g Strain Gage Time Histories



Moment Diagram

West

East



Axial Force Diagram

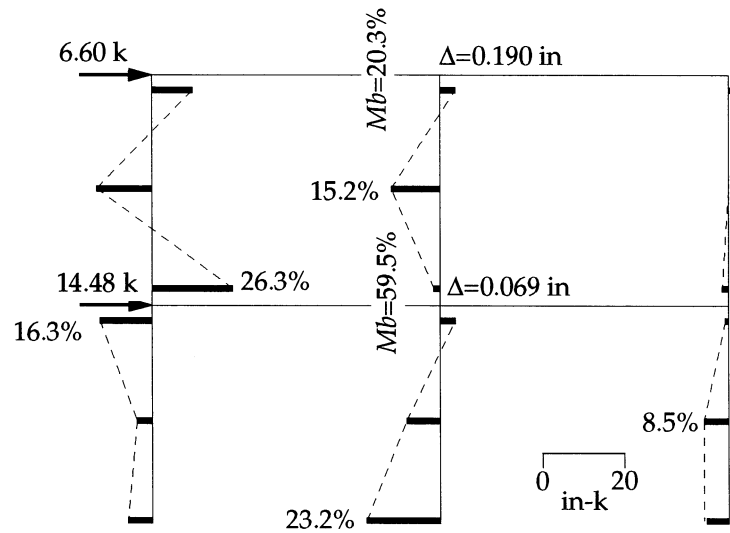
Notes:

1. Force values are % of capacity.
2. Moment diagram drawn on tension side.
3. Positive axial force indicates tension.
4. Mb and Pb indicate values of beam forces.

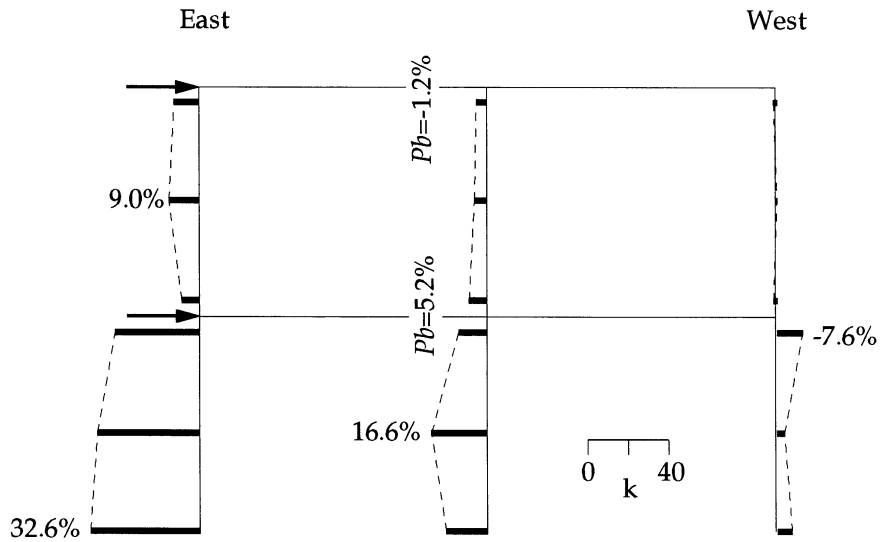
(a) Taft 0.1g at Maximum Base Shear, $t=2.65$ sec

FIGURE 8-22 Moment and Axial Diagrams for Maximum Base Shear Series

Figure 8-22 (Continued)



Moment Diagram



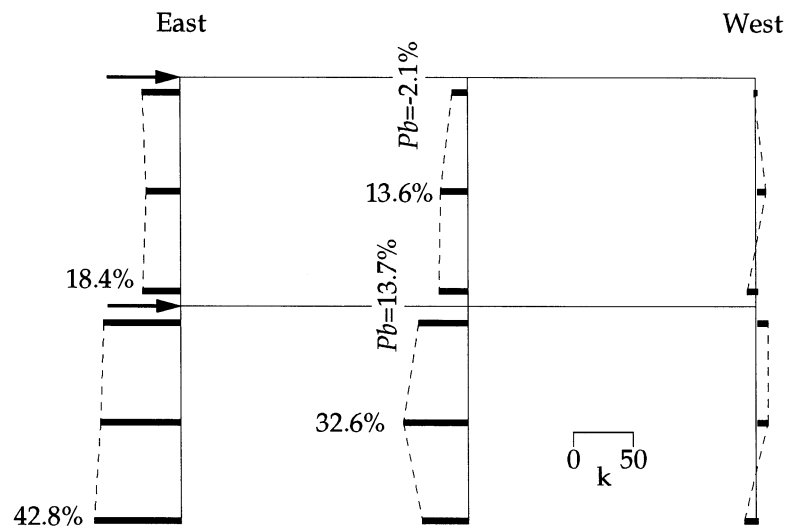
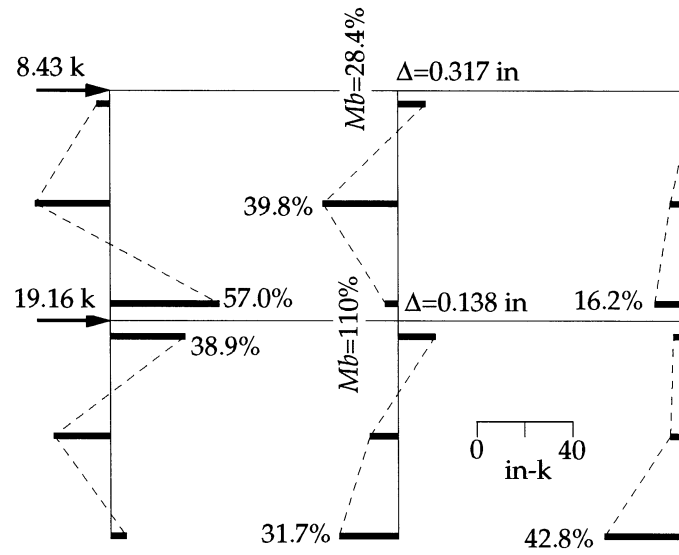
Axial Force Diagram

Notes:

1. Force values are % of capacity.
2. Moment diagram drawn on tension side.
3. Positive axial force indicates tension.
4. Mb and Pb indicate values of beam forces.

(c) Taft 0.55g at Maximum Base Shear, $t=6.52$ sec

Figure 8-22 (Continued)



- Notes:
1. Force values are % of capacity.
 2. Moment diagram drawn on tension side.
 3. Positive axial force indicates tension.
 4. M_b and P_b indicate values of beam forces.

(d) Taft 0.80g at Maximum Base Shear, $t=4.66$ sec

(Figure 8-22c), the column at the unloaded side (ULS) generally carries comparatively little compression, as such compression is more efficiently transferred diagonally through strut action in the wall. Thus the overturning moment caused by the lateral loads is counteracted by a moment-couple formed from axial tension in the LS column and compression in the masonry infill.

The second story LS column moment behavior remains qualitatively similar throughout the four tests, only increasing in magnitude with increasing excitation. Thus, even significant diagonal cracking, which occurred during the Taft 0.55g test, did not prevent the formation of strut action to transfer load around the window openings. Referring to the crack patterns of Figure 8-8a, it can be seen that triangular portions of the wall below the window openings remain almost entirely free of bed joint failure and thus compressive struts may develop here with little or no relative horizontal sliding of masonry courses. The maintained presence of strut action and lack of sliding failures helps to explain the stable diagonal crack pattern, as well as the minimal losses of shear and drift capacity of the second story (Figures 8.2 – 8.5).

The base shear series moment diagrams for the first story columns appear far more inconsistent, and no firm conclusions regarding strut action appear obvious. Yet certain isolated diagrams, the LS column of Taft 0.80g (Figure 8-22d), for example, are suggestive of strut action. A large change in moment exists over the upper half of the column, although the lower half of the column exhibits a smaller moment gradient. The far more complex cracking of the first story panels, and thus more complex behavior, may explain the varied local effects reflected in the column moment diagrams. Further discussion is given in Section 8.7.

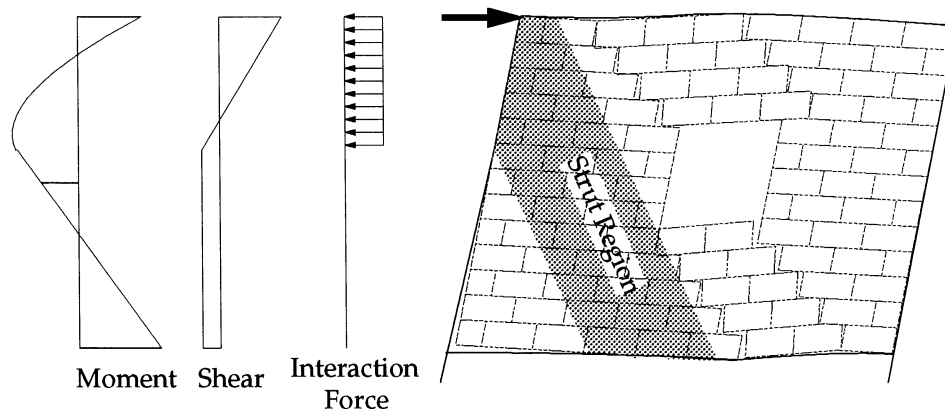


FIGURE 8-23 Hypothesized Strut Mechanism

8.5.2. Maximum First Story Displacement Series

Observations on the second story behavior made in the preceding section also apply here, but the maximum first story displacement series gives far more consistent and interpretable results for first story behavior (Figures 8.24a–d). In both the Taft 0.55g and 0.80g tests, after substantial separation of infill and frame, the first story ULS column shows a moment diagram similar in shape to that typical of a bare frame. That is, the moment diagram is almost entirely a function of the first story displacement, with minimal effect from interaction of the infill.

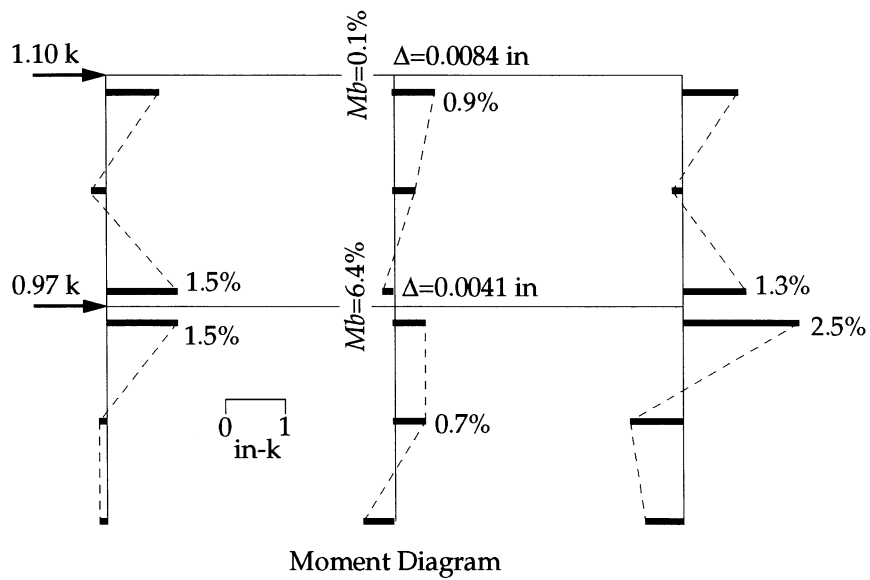
The first story LS columns tend to have very small base moments and large axial loads, again suggesting a moment couple formed from column tension and an infill compression resultant. However, in the Taft 0.35g and 0.55g tests (Figures 8.24b and c), moment diagrams suggest single curvature, significantly different than the reverse curvature expected in a bare frame response. Finally, in the Taft 0.80g test (Figure 8-24d), extremely large moment gradients appear in the top half of the LS and center columns.

8.5.3. Column Shear Cracking

Between 6.0 and 6.5 sec of the Taft 0.80g test, shear cracking occurred at the tops of the east and center columns. Figure 8-19b shows substantial bed joint sliding in the upper courses of the masonry and even spalling of some blocks directly adjacent to the columns by this time in the test. These local failures in the masonry allow significant shear force to develop over a relatively short portion of the column. In the center column, the top moment is 102.4 in-k (132%); and the mid-height moment, 64.5 in-k (83%). Estimating the magnitude of shear as the slope of the moment diagram over half the column height (24.8 in) gives

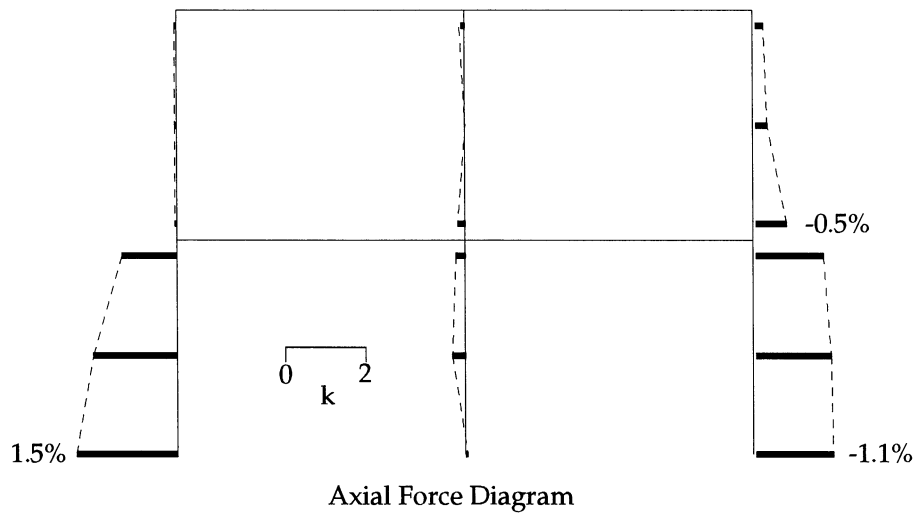
$$V = \frac{(102.4 + 64.5) \text{ in} \cdot \text{k}}{24.8 \text{ in}} = 6.7 \text{ k}. \quad (8.8)$$

The actual shear likely will be larger than this value as any lateral interaction force near the top of the column will tend to increase the local shear. The shear capacity of the column, neglecting axial force effects, may be estimated at 7.4 k according to ACI Eqs. (11-3) and (11-15) (ACI 318-95). The significant axial tension in the center column will further reduce the shear capacity.



East

West



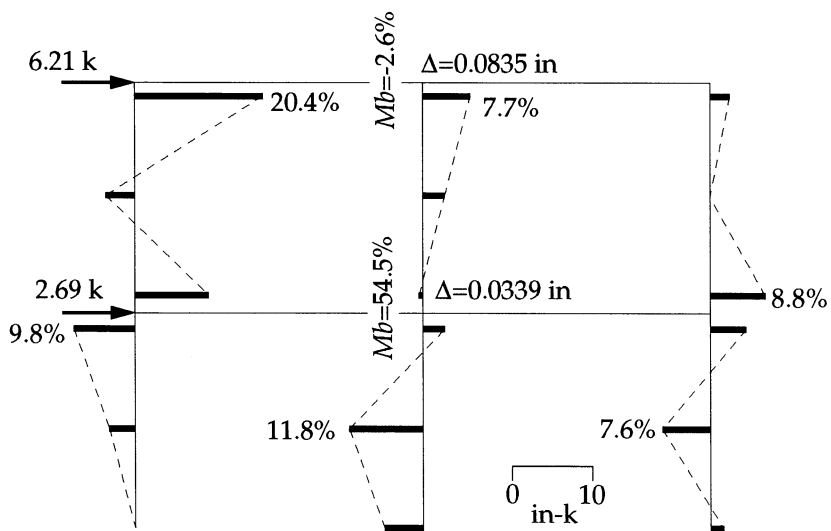
Notes:

1. Force values are % of capacity.
2. Moment diagram drawn on tension side.
3. Positive axial force indicates tension.
4. Mb and Pb indicate values of beam forces.

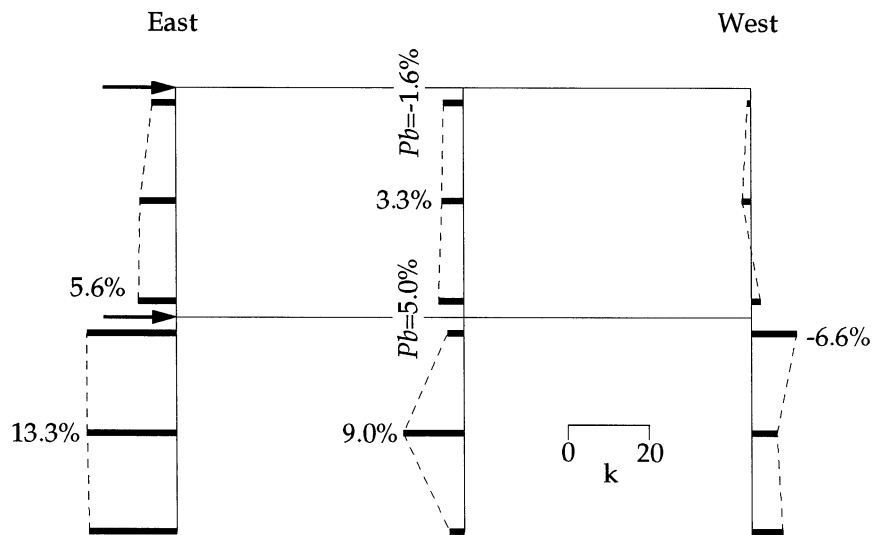
(a) Taft 0.1g at Maximum 1st Story Displacement, $t=4.64$ sec

FIGURE 8-24 Moment and Axial Diagrams for Maximum 1st Story Displacement Series

Figure 8-24 (Continued)



Moment Diagram



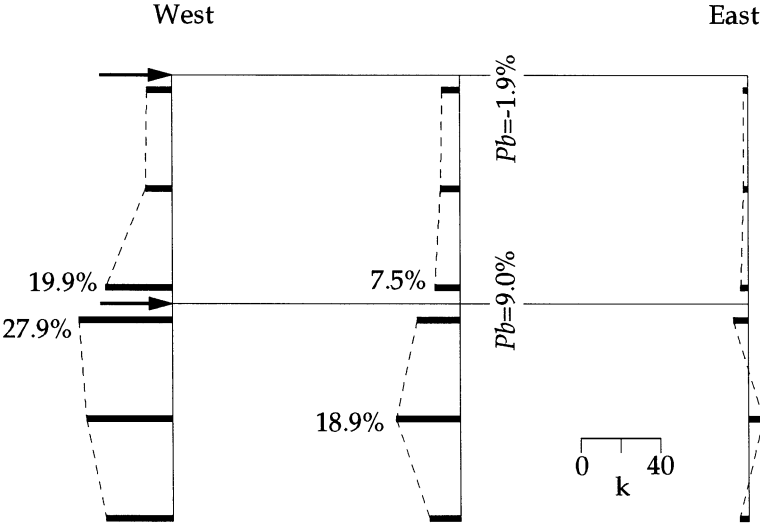
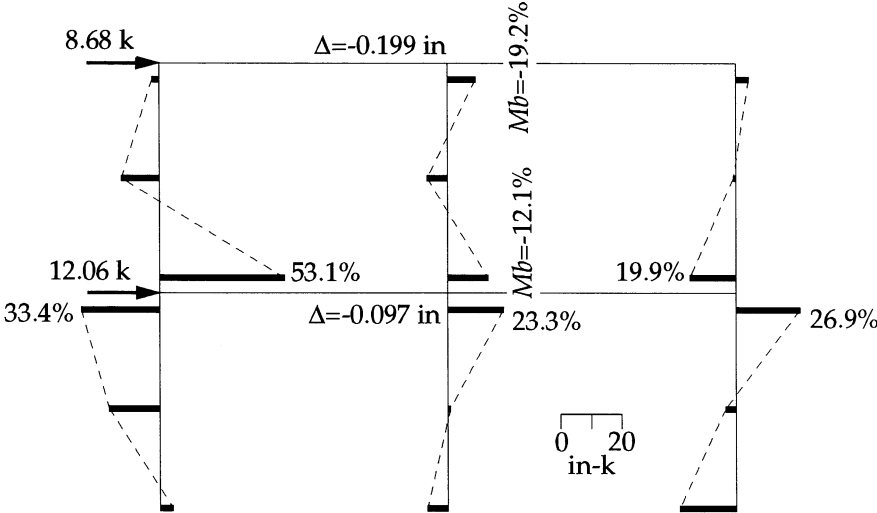
Axial Force Diagram

Notes:

1. Force values are % of capacity.
2. Moment diagram drawn on tension side.
3. Positive axial force indicates tension.
4. M_b and P_b indicate values of beam forces.

(b) Taft 0.35g at Maximum 1st Story Displacement, $t=5.81$ sec

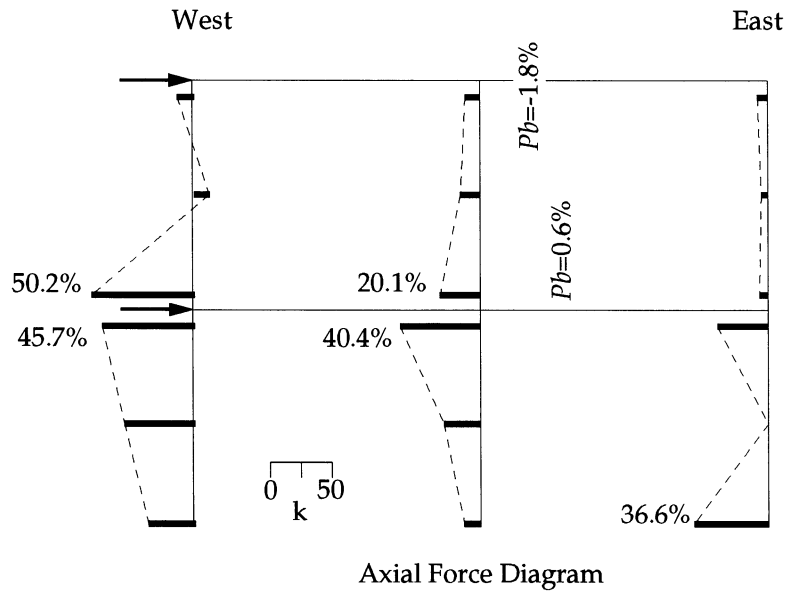
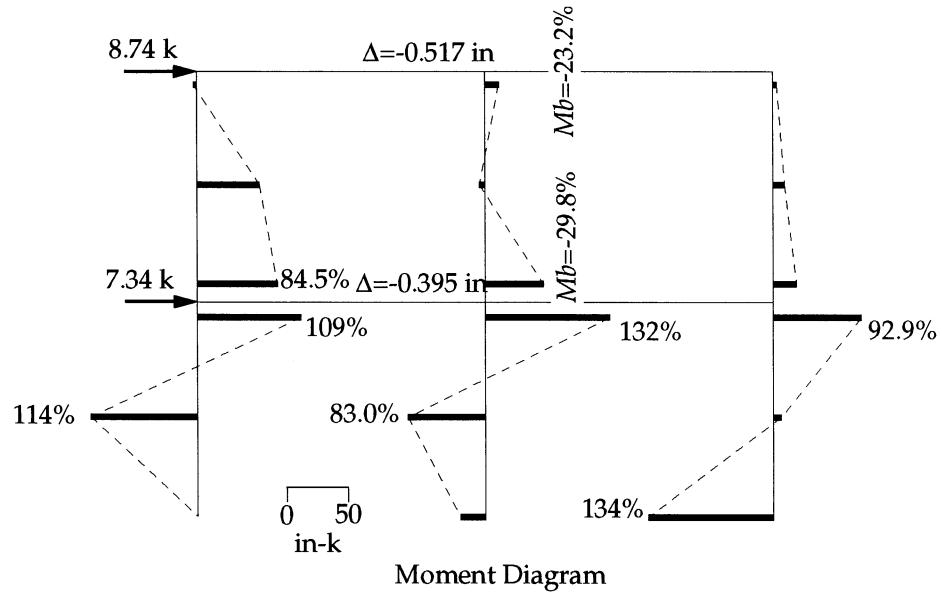
Figure 8-24 (Continued)



- Notes:
1. Force values are % of capacity.
 2. Moment diagram drawn on tension side.
 3. Positive axial force indicates tension.
 4. Mb and Pb indicate values of beam forces.

(c) Taft 0.55g at Maximum 1st Story Displacement, $t=6.44$ sec

Figure 8-24 (Continued)



Notes:

1. Force values are % of capacity.
2. Moment diagram drawn on tension side.
3. Positive axial force indicates tension.
4. M_b and P_b indicate values of beam forces.

(d) Taft 0.80g at Maximum 1st Story Deflection, $t=10.76$ sec

8.6. Infill Panel Behavior

8.6.1. Strain Rosettes

The strain gage rosettes applied to the surface of the first story masonry walls (Figure 3-5) allow for further detection and verification of diagonal strut mechanisms. Typical time histories from the central rosette of the east panel during Taft 0.55g are shown in Figure 8-26. Standard formulas are used to calculate principal strains and directions (Sabnis et al. 1983) from the raw data.

Principal strains and directions, over the previously defined peak shear and displacement series, are given in Tables 8-6 and 8-7, with rosette locations keyed by number to Figure 8-25. Note that one of the gages in the rosette at Location 4 gave consistently unreliable results, especially for higher level tests. The poor results from this gage are likely due to a crack in the masonry which propagated directly behind the gage.

The peak base shear series (Table 8-6) clearly reveals the presence of large principal compressive strains at all six locations. Tensile strains of considerably less magnitude appear as well. The inclination of the compressive strain below horizontal consistently fell between 35 and 45 degrees, compared to the main diagonal angle of about 37 degrees. Further, the inclination of the principal direction tended to reverse diagonals with reversing load. All of these observations lend support to the idealization of the masonry infill as a compressive strut.

The compressive strains generally increase with increasing p_g , although a noticeable drop-off occurs for some of the gages of the east panel (Locations 5 and 6) at 0.80g. This may be due to the difference in the state of cracking at $t=4.66$ sec, when the 0.80g peak base shear occurs. At this time Figure 8-19a shows the east wall to have major bed joint failures near the top and bottom of the panel, whereas the west wall has such failure only near the bottom. Any ability to develop significant compressive forces corner-to-corner in the east panel will be severely reduced by the horizontal slipping along the failed bed joints, caused by the horizontal force component of the strut itself. But here with the adjacent west panel in a less damaged state, the strut resistance lost in the east panel may be compensated by the higher strains of the west panel.

This hypothesized sensitivity of the compressive strut action to the state of cracking, especially long bed joint failures, is further supported by the peak first story displacement series in Table 8-7. Similar trends for the low-level earthquakes appear here as previously described. However, the sample time for the Taft 0.80g test is now $t=10.76$ sec by which time severe damage has occurred in the masonry walls. Figure 8-19c shows at least two full-width horizontal bed joint failures in each wall panel as well as numerous diagonal

and stepped cracks. Here all of the rosettes show diminished compressive strains. The increase in first story drift seen in the hysteresis plot (Figure 8-20) may be associated with the failure of the infill to mobilize an effective compressive strut mechanism due to the extensive damage and many prominent horizontal slip planes.

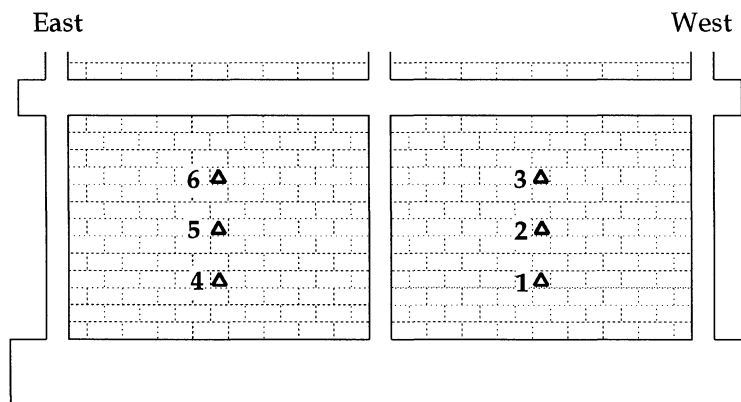


FIGURE 8-25 Strain Gage Rosette Locations

8.6.2 Panel DCDTs

Typical time histories from diagonal panel displacement transducers (DCDTs) are shown in Figure 8-27 from Taft 0.35g. In the first and second stories displacements were measured along main diagonals over a gage length of about 77 in. Second story instrumentation also included off-diagonal measurements over gage lengths of about 55 in. Individual values of elongation (positive) or shortening (negative) displacement for the peak base shear series under Taft 0.35g are given in Figure 8-28; and under Taft 0.80g, in Figure 8-29.

For the Taft 0.35g test, the main diagonals in compression shorten about 0.010" to 0.015". The opposing diagonals elongate to a lesser degree than the loaded diagonals shortened, and the extension of the second story main diagonals was significantly greater than that in the first story. The window opening in the second story panels causes behavior better modeled as two adjacent half-width panels, and thus the displacements measured by the second story off-diagonal DCDTs show nearly equal shortening and lengthening. This also supports the formation of compressive strut action inclined to pass below the openings, earlier suggested by the crack patterns (Section 8.3) and frame moments (Section 8.5). In all cases the DCDTs of the panels on the loaded side (east) exhibited displacements of greater magnitude, suggesting that the loaded side infill panels carry more than half of the load.

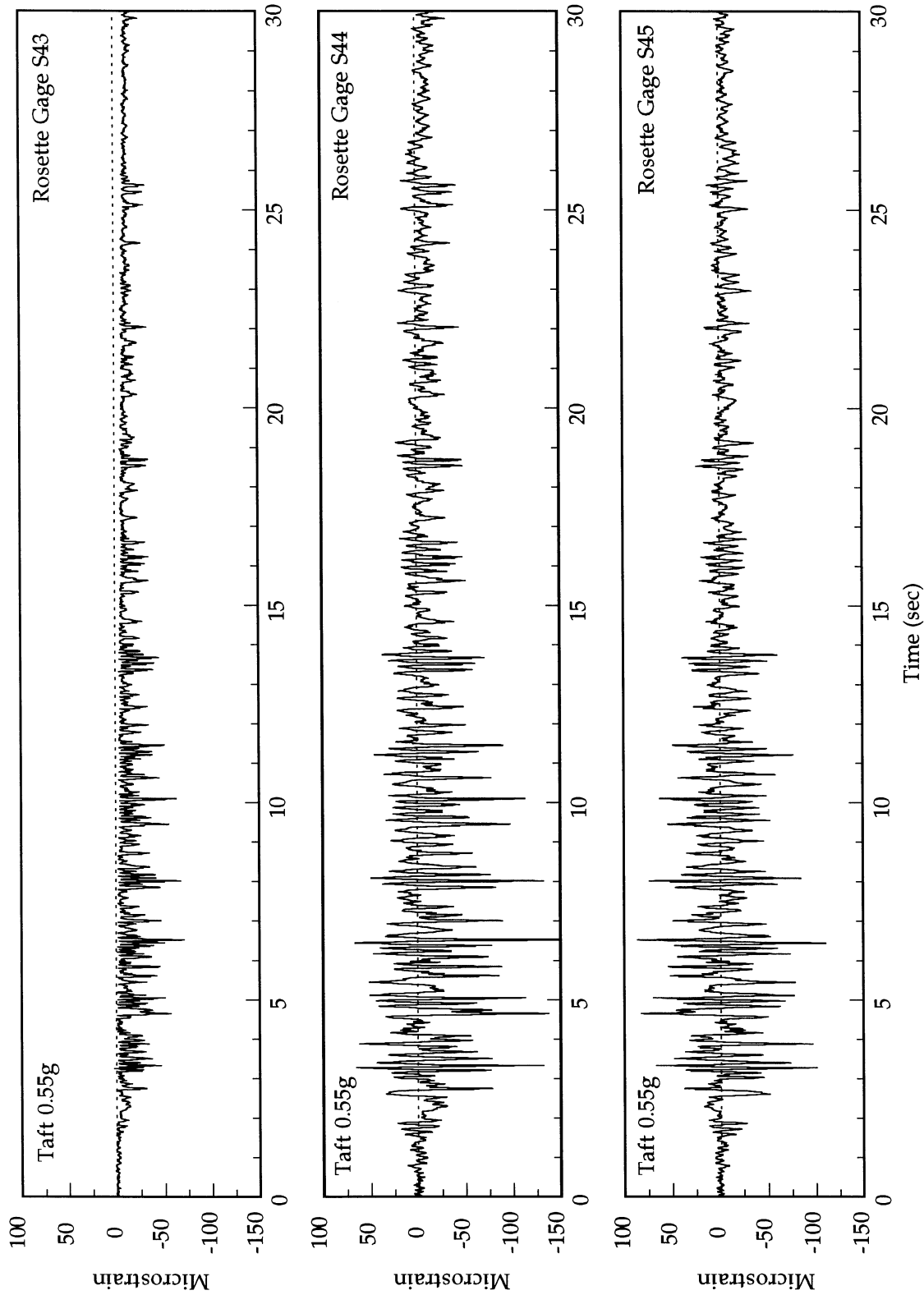


FIGURE 8-26 Taft 0.55g Strain Gage Rosette Time Histories

TABLE 8-6 Rosette Strains: Maximum Base Shear Series

Loc.	1	2	3	4*	5	6
pga (g)	Principal Tensile Strain (microstrain)					
0.10	4.1	10	12	1.1	5.8	1.3
0.35	26	38	35	126	52	21
0.55	40	94	72	218	96	59
0.80	61	203	101	436	125	39
	Principal Compressive Strain (microstrain)					
0.10	-8.9	-15	-14	-19	-18	-15
0.35	-89	-72	-49	-51	-106	-78
0.55	-187	-187	-158	-83	-213	-154
0.80	-366	-370	-296	-185	-215	-104
	Compressive Strain Inclination (degrees)					
0.10	37	43	42	44	40	44
0.35	43	41	44	33	44	44
0.55	41	40	40	27	42	42
0.80	39	41	38	18	45	40

*Loc. 4 unreliable, see text.

TABLE 8-7 Rosette Strains: Maximum First Story Displacement Series

Loc.	1	2	3	4*	5	6
pga (g)	Principal Tensile Strain (microstrain)					
0.10	-0.28	0.70	3.8	12	-0.19	-0.13
0.35	22	40	37	130	52	23
0.55	31	72	97	22	110	42
0.80	4.3	40	197	131	83	22
	Principal Compressive Strain (microstrain)					
0.10	-14	-15	-15	-7.9	-26	-14
0.35	-64	-66	-45	-47	-96	-67
0.55	-72	-134	-113	-348	-217	-160
0.80	-69	-104	-99	-1040	-107	-33
	Compressive Strain Inclination (degrees)					
0.10	43	42	36	29	29	43
0.35	39	40	43	32	45	45
0.55	34	40	43	41	42	43
0.80	34	28	31	41	41	38

*Loc. 4 unreliable, see text.

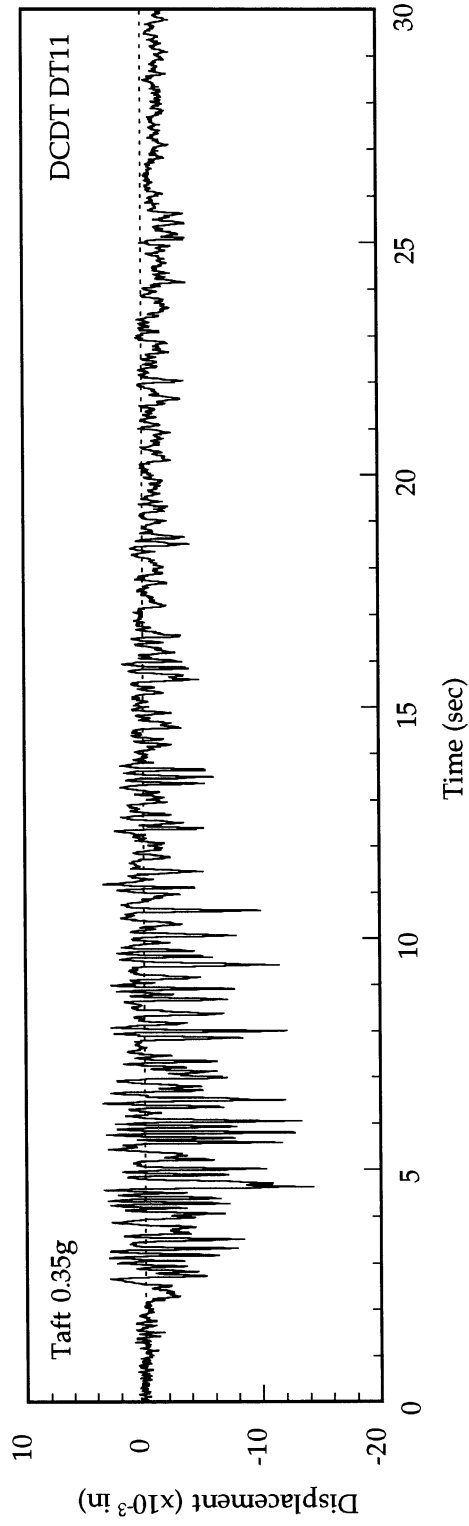
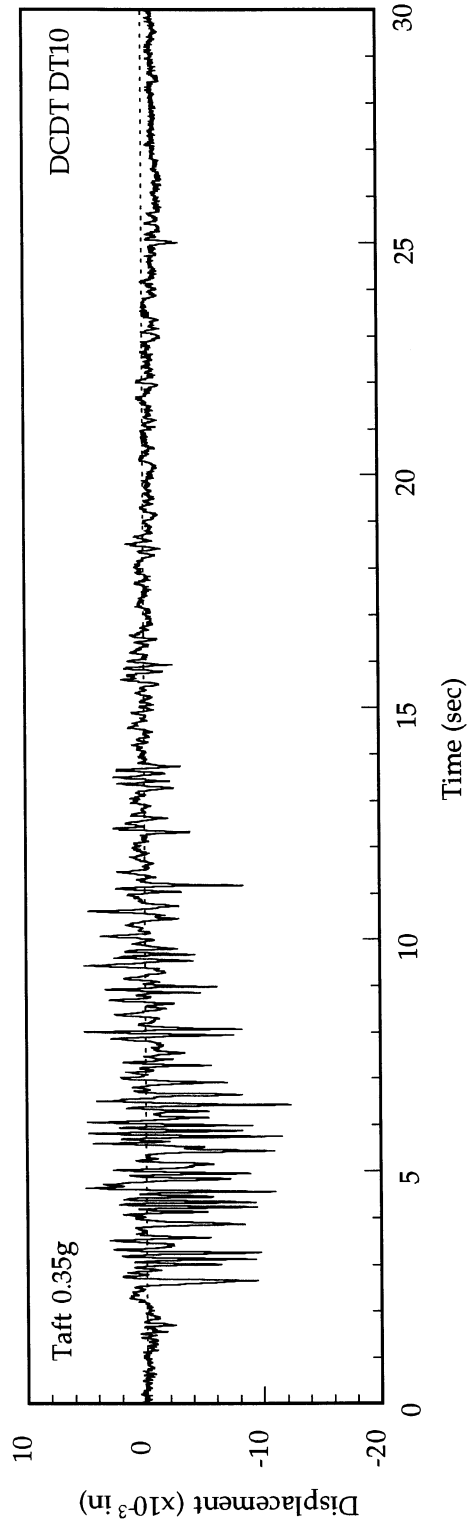
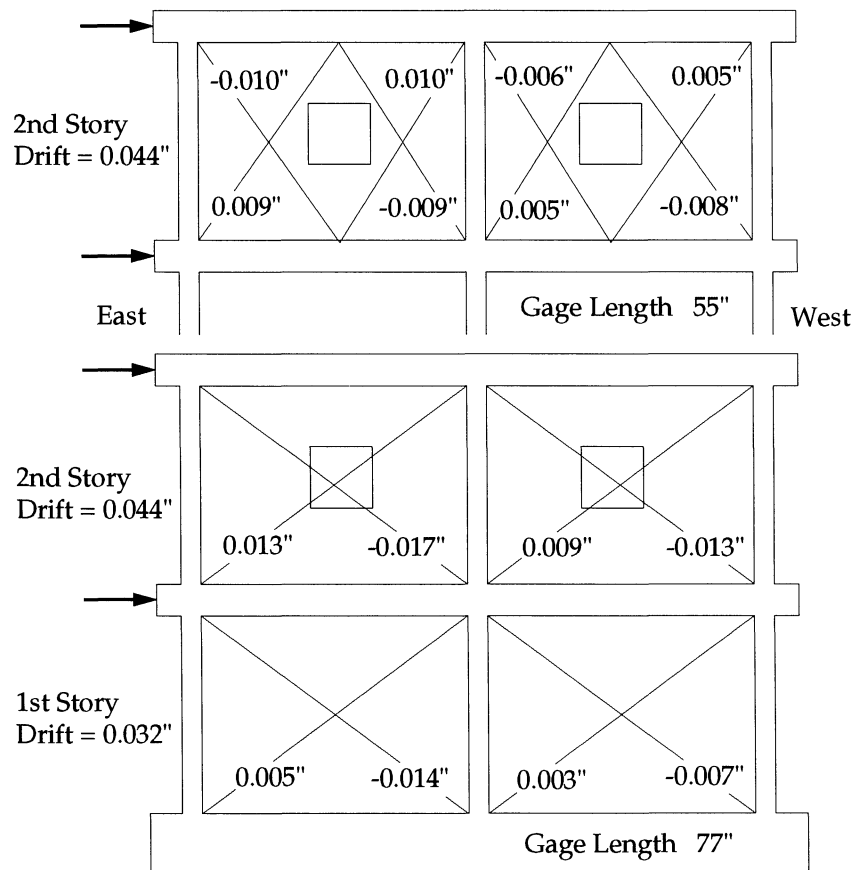


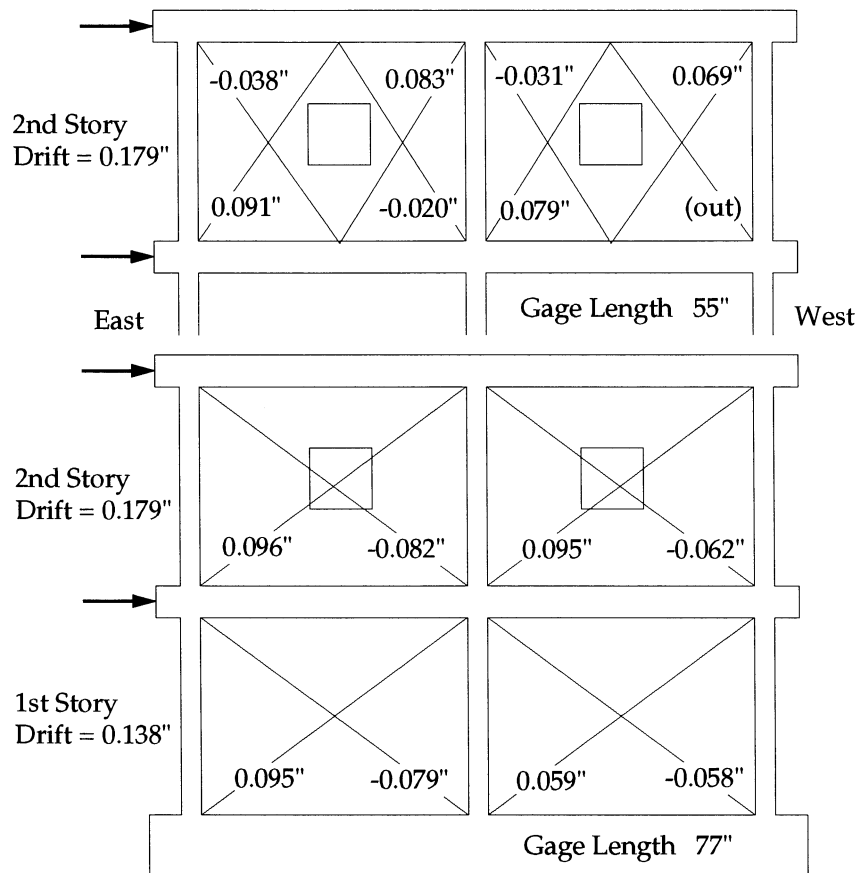
FIGURE 8-27 Taft 0.35g DCDT Time Histories

Comparing the Taft 0.35g results to those from the Taft 0.80g test shows diagonal displacements which increase by a factor of generally at least 5, and in some cases nearly 20, with only an approximate four-fold increase in story drifts. The measurements from the Taft 0.80g test consistently show compressed diagonals shortening significantly less than the opposing diagonals lengthen. However, during this test significant cracking has occurred within the panels resulting in geometric discontinuities which affect the DCDT measurements. For instance in the first story, the portion of the masonry panel above a large bed joint sliding crack will displace in the loaded direction relative to the portion of the panel below the bed joint, thereby further shortening the compressed diagonal and elongating the opposing diagonal. With significant bed joint sliding failures within the gage length spanned by a diagonal DCDT, the measured value cannot be expected to have a direct relationship to the force transferred through the masonry. These DCDTs span across large portions of the wall panels and therefore are not suited to capture local effects caused by masonry cracking. Both sliding bed joints and stepped cracks occurring within the panel will produce changes in the diagonal measured displacements, but the type of cracking generally cannot be differentiated based on such measurements alone.



Negative indicates shortening.

FIGURE 8-28 Taft 0.35g DCDT Displacements at Maximum Base Shear



Negative indicates shortening.

FIGURE 8-29 Taft 0.80g DCDDT Displacements at Maximum Base Shear

If diagonal shortening or lengthening occurs due to racking deformation of the panels only, with no axial deformation of the columns, then the diagonal displacement must equal the story drift multiplied by the cosine of the inclination angle of the main or off-diagonal. Based on the story drifts the diagonals should exhibit length changes as given in Table 8-8. In all cases these displacements due to racking are much greater than the measured quantities.

TABLE 8-8 Panel Diagonal Displacements Due to Racking Deformation

pga (g)	1st Story		2nd Story		
	Drift (in)	Main Diag. Disp. (in)	Drift (in)	Main Diag. Disp. (in)	Off-Diag. Disp. (in)
0.35	0.032	0.026	0.044	0.035	0.021
0.80	0.138	0.111	0.179	0.143	0.083

8.7. Strut Mechanisms

8.7.1. Effective Strut Width and Stiffness

Much of the experimental data reviewed in the previous sections has suggested that strut mechanisms might serve as acceptable idealizations for certain features of the observed infill behavior. For unreinforced masonry, compressive strut models have the potential to model the initial stiffness and low-level behavior of the infill before significant bed-joint shear failure. Based on a beam-on-elastic-foundation analogy and experimental results, Stafford Smith and others (see Section 1.3.2) have derived expressions for contact lengths between frame and infill. From Drysdale et al. (1994), the vertical contact length is given by

$$\alpha_h = \frac{\pi}{2} \sqrt[4]{\frac{4E_c I_c h}{E_m t \sin 2\theta}}, \quad (8.9)$$

and the horizontal by

$$\alpha_L = \pi \sqrt[4]{\frac{4E_c I_b L}{E_m t \sin 2\theta}}, \quad (8.10)$$

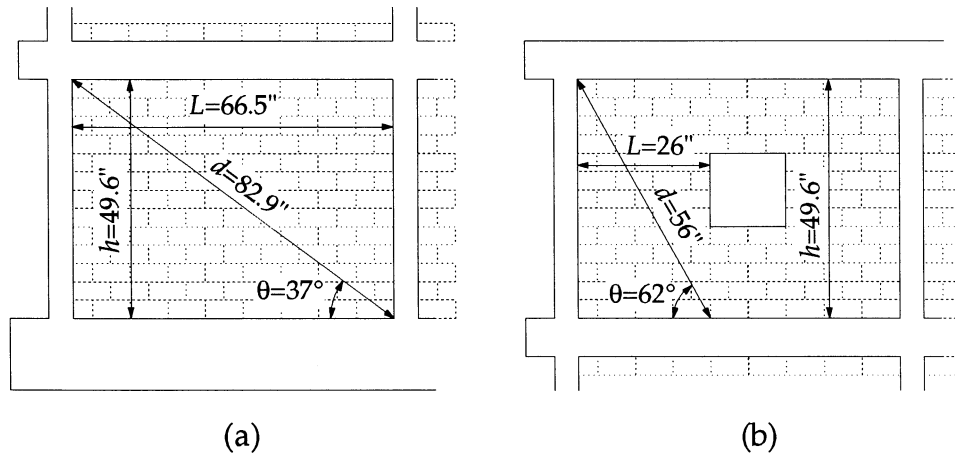
where I_c and I_b are moments of inertia of the column and beam, E_c and E_m are moduli of the frame and masonry, h and L are height and length on the infill panel, t is the mortared thickness of the masonry and θ is the angle of inclination of the main diagonal. Hendry (1990) relates the effective strut width, w , to the contact lengths by

$$w = \frac{1}{2} \sqrt{\alpha_h^2 + \alpha_L^2}. \quad (8.11)$$

Based on an assumed strut width, the axial stiffness is

$$k_s = \frac{wtE_m}{d}. \quad (8.12)$$

Figure 8-30a gives the dimensions of a lower story panel of the infilled frame specimen. Transformed, elastic moments of inertia of the beam and column are 233 in⁴ and 65 in⁴, respectively. Using the material properties of Sections 2.2 and 2.3, the contact lengths are $\alpha_h = 21.3$ " and $\alpha_L = 63.2$ ". By Eq. (8.11) the strut width would be $w = 33.3$ " (40% of the main diagonal length); and the axial stiffness by Eq. (8.12), $k_s = 597$ k/in. Incorporating two such struts into a beam-element frame model results in a first story lateral stiffness of 851 k/in. Recall from Eq. (4.15) that the measured lateral stiffness of the first story,



(a) (b)
FIGURE 8-30 Infill Panel Dimensions

assuming shear building behavior, was 486 k/in. Therefore, this strut idealization results in a stiffness of 175% of the measured value.

Paulay and Priestley (1992) recommend a conservatively high strut width approximation of

$$w = \frac{1}{4}d, \quad (8.13)$$

where d is the length of the panel diagonal. For the first story of this specimen, the strut width would be 20.7" and the story lateral stiffness, 617 k/in (127% of measured). FEMA-273 (1997) recommends a strut width of

$$w = 0.175(\lambda_1 h_{col})^{-0.4} r_{inf} = 0.175 \left(\frac{\pi h}{2\alpha_h} \right)^{-0.4} d \quad (8.14)$$

which gives a strut width of 8.7" (10% of the panel diagonal), and a lateral story stiffness of 296 k/in (61% of measured).

The strut width provided by Eq. (8.11) largely overestimates the measured stiffness, while a strut width of one-fourth the diagonal length, Eq. (8.13), provides perhaps a reasonable and conservative overestimate of the measured stiffness. The FEMA-273 method, however, largely underestimates the measured stiffness. An underestimate of strut stiffness will result in a more flexible frame-strut model and may unconservatively result in a lower seismic demand. An underestimate of the strut stiffness will also distribute less of the total load to the infill, resulting in an underestimate of the force demand on the infill. However, a more flexible frame-strut model may result in larger story drifts, and therefore greater deformation demand on the infill,

consistent with the FEMA-273 classification of infill panels as a deformation-controlled component. Note also that for strut widths which are proportional to diagonal length, the axial strut stiffness becomes independent of diagonal length.

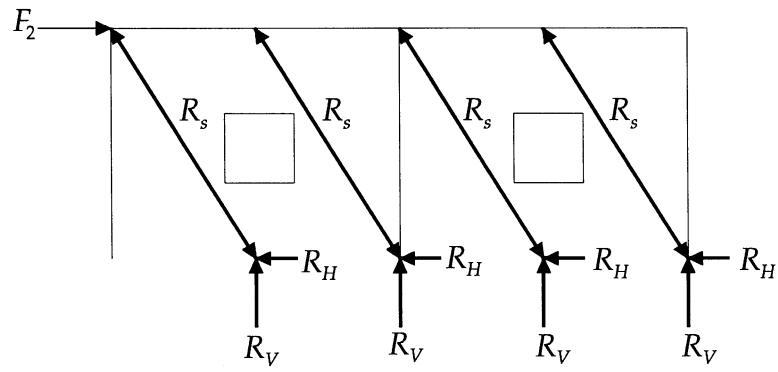
The second story stiffness may be estimated by dividing each infilled bay into two half-panels (Figure 8-30b), resulting in $\alpha_h=22.2"$ and $\alpha_L=51.9"$. The equivalent strut width is 28.2" (50% of diagonal) by Eq. (8.11); and the axial stiffness, 748 k/in. Incorporating four struts into a frame model gives a second story lateral stiffness of 576 k/in, 240% of the measured stiffness of 240 k/in (Eq. (4.15)). A strut width of one-fourth the length of the half-panel diagonal results in a strut width of 14" and a lateral story stiffness of 365 k/in (152% of measured). Both of these methods overestimate lateral stiffness. The FEMA-273 equation results in a strut width of 5.9" (11% of diagonal) and a lateral story stiffness of 206 k/in (86% of measured), again underestimating the stiffness.

The stiffness reduction due to window openings can also be estimated by applying a reduction factor to the full-panel stiffness, based on the relative area of window opening to infill panel. Both experiments and numerical studies have shown a wide range of stiffness reduction factors, dependent upon both overall size and location of the opening. Finite element studies by Mosalam (1996) determined stiffness reduction factors for square, centrally-placed window openings covering various percentages of total panel area. With a window area of 8% of panel area in this specimen, the reduction factor is about 0.85. Since the full-panel geometry of the second story panel is identical to that of the first, the second story stiffness would be estimated as 85% of 851 k/in, or 723 k/in (175% of measured), also a large overestimate.

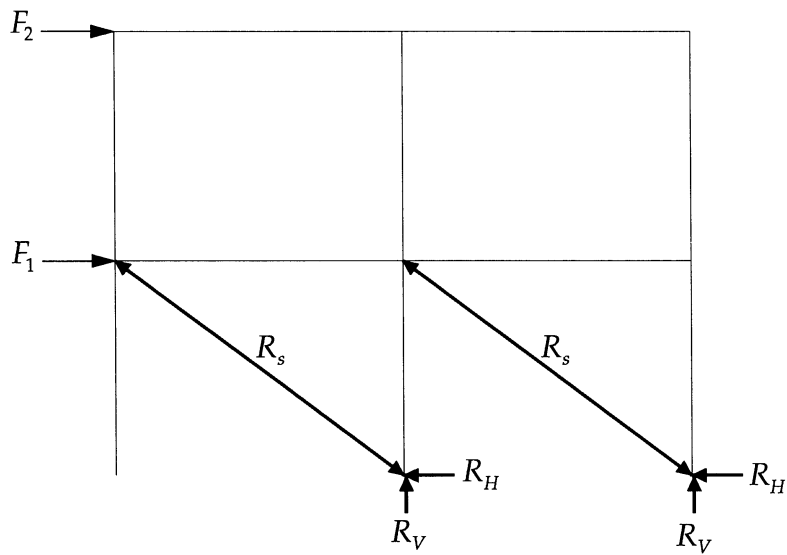
8.7.2. Experimental Strut Forces

Strut forces can be directly estimated from experimentally measured frame forces by assuming a reasonable geometric strut configuration and applying static equilibrium. Figure 8-31 shows possible strut configurations for first and second story infills. In the first story two main diagonal struts are assumed; in the second story, four half-panel struts. In both stories, all struts will be assumed to act equally in resisting the applied horizontal loads, although the DCDT measurements presented in Section 8.6.2 suggest that the struts nearer to the applied load will carry slightly more of the load.

For the Taft 0.35g test at the time of peak base shear, the total base shear is 9.90 k (see Table 8-4), giving a first story horizontal strut component $R_H = 4.95$ k for each strut. For the corresponding axial strut force, $R_s = 6.17$ k, the average



(a) Section below 2nd Story Infill



(b) Section below 1st Story Infill

FIGURE 8-31 Assumed Strut Configurations and Forces

axial stress may be approximated as 220 psi, by dividing by the strut width of 20.7" and mortared thickness of 1.36". Finally, by dividing the axial stress by the masonry modulus of 1095 ksi, the axial strain is approximated as 200 microstrain. Over the entire length of a main diagonal, this strain would cause a total change in length of 0.017". In a similar manner for the Taft 0.80g test at peak base shear, the total change in main diagonal length would be 0.046". These displacement values are of the same magnitude as the measured values shown in Figures 8.28 and 8.29, and agree extremely well with values in Table 8-8. The assumption here that all of the applied shear force is transferred through the diagonal struts is essentially equivalent to the assumption of pure racking deformation used in Section 8.6.2 to calculate the values in Table 8-8. However, the calculations for Table 8-8 are based on measured story drifts, while those here are based on measured story forces, so the good correspondence observed is not necessarily guaranteed by the similar behavioral assumptions.

For the second story infill, the horizontal component of each strut force may be estimated as one-fourth of the measured second story shear. For the Taft 0.35g test at peak base shear this approximation gives $R_H = 0.60$ k. In a similar manner as was done for the first story struts, the total displacement along the half panel diagonal is found to be 0.003". For the Taft 0.80g test, $R_H = 2.11$ k and the total diagonal displacement is 0.012". These approximated values are less than both the measured values shown in Figures 8.28 and 8.29 and the estimated values in Table 8-8.

8.8. Infill Shear Behavior

For unreinforced masonry walls, sliding shear failures of bed joints may significantly alter the nature of interaction between frame and infill, reducing the effectiveness of main diagonal struts and producing large local forces on frame members. In Section 8.5.3 the shear cracking at the tops of two first story columns was related to the large lateral forces imposed by the adjacent full-width, bed-joint sliding. Typically for masonry, a Mohr-Coulomb friction relationship defines shear strength, τ , as

$$\tau = \tau_0 + \mu\sigma, \quad (8.15)$$

where τ_0 is the cohesive strength; μ , the coefficient of friction; and σ , the applied normal stress. In lieu of actual material test data, Paulay and Priestley (1992) cite an average value of cohesive strength of $\tau_0 = 0.03f'_m$, and a typical range for the coefficient of friction of $0.3 \leq \mu \leq 1.2$.

Paulay and Priestley (1992) argue that almost all of the clamping force across sliding planes is provided by the vertical component of the strut force. Interface gaps between the frame and infill will exist due to initial construction and lengthening of the tension (LS) column, thus preventing transfer of significant portions of the gravity loads from higher stories through the masonry panels. For a diagonal strut force, R_s , the lateral shear strength of a single infill panel may be estimated by

$$V_b = \tau_0 Lt + \mu R_s \sin \theta, \quad (8.16)$$

the force analog of Eq. (8.15). The lateral shear strength must also equal the horizontal component of the strut force

$$V_b = R_s \cos \theta. \quad (8.17)$$

Solving Eqs. (8.16) and (8.17) simultaneously results in a compressive strut force

$$R_s = \frac{(\tau_0 Lt / \cos \theta)}{1 - \mu \tan \theta}, \quad (8.18)$$

and a lateral force to cause sliding failure

$$V_b = \frac{\tau_0 Lt}{1 - \mu \tan \theta}. \quad (8.19)$$

Alternatively, Eq. (8.19) can be reformulated as an average shear stress for sliding failure as

$$f_v = \frac{V_b}{Lt} = \frac{\tau_0}{1 - \mu \tan \theta}. \quad (8.20)$$

A coefficient of friction of 0.89 has been measured experimentally by Mehrabi et al. (1994) using identical CMU to those of this specimen and comparable mortar. For this coefficient of friction, $\tau_0 = 0.03f'_m$ and dimensions given in Figure 8-30, Eq. (8.19) gives a first story lateral strength of 24 k. Assuming nearly all of the story shear is carried by the masonry infill before significant bed joint sliding, the average shear stress would be 131 psi.

The Taft 0.55g test (Figures 8.4 and 8.8) caused the first masonry shear failures at a peak story shear of about 20k. Far more extensive bed-joint sliding occurred during the Taft 0.80g test (Figure 8-19), and Section 8.3 related specific bed-joint cracking events with noticeable drops in the force values of the hysteretic relation (Figure 8-20). Many of these force losses occurred in the range of 15 to 25 k, although the structure then continued to carry increased load beyond that point. Bed-joint failure resulted in a momentary loss of strength as the actual sliding occurred until a new, stable geometry of the

infill can be formed based on the boundary conditions imposed by the frame. With the new geometry, further strut action allowed for increased load carrying capacity, although now likely with a different strut configuration. The first story shear strength was about 27 k or 150 psi. The analytical estimate of first story lateral strength of 24 k is 20% greater than the story shear which caused the first observed bed-joint shear failure, and about 11% less than the measured first story strength.

Using the lower bound coefficient of friction of 0.30 results in a first story lateral strength of 10 k, or an average shear stress of 57 psi. This lower bound strength is certainly well below any of the experimentally observed cracking forces, and may be an acceptable conservative assumption for design. However, for more accurate assessment of existing structures a better estimation of μ would be desirable. Unfortunately, material testing data for coefficients of friction is scarce in the published literature, and that which is available shows large variation and strong dependence upon the specific types of block and mortar used (Hendry, 1990). To further compound the problem, the lateral shear strength shows very sensitive dependence upon μ . Figure 8-32 shows this sensitive dependence of lateral shear strength by Eq. (8.20) as a function of coefficient of friction, μ . Previous research (Buonopane, 1995) has shown that such sensitive dependence on μ exists even in more advanced analytical models for lateral strength of infilled frames. For unreinforced masonry infill, where lateral shear strength plays a determining role in overall behavior, research must be focused on better understanding of the shear-friction behavior. In fact, most current design guidelines (Paulay and Priestley, 1992) recommend conservatively neglecting the shear-friction contribution to lateral strength, and consider only the frame capacity based on assumed locations of plastic hinging caused by infill interaction.

Other methods available for determining the shear strength of unreinforced masonry, such as FEMA-273 (1997), NEHRP (1997) or ACI 530 (1995), do not account for additional lateral strength due to the interaction of the frame and infill, but rather consider only the cohesive bond of the bed joints. FEMA-273 allows an average shear strength of 27 psi for running bond masonry in good condition when no in-place shear tests are available. For ungrouted, running bond masonry both ACI 530-95 and NEHRP (1997) limit shear stress to 37 psi based on a parabolic stress distribution, corresponding to a limiting average stress of 25 psi. These shear strengths are considerably less than the measured value of 150 psi, showing that the diagonal compression induced by frame-infill interaction can produce a significant increase in friction-based shear strength. ACI 530-95 and NEHRP (1997) allow an increase in shear strength due to gravity load compression. This increase is not appropriate for infill frames since nearly all gravity load will be carried through the frame.

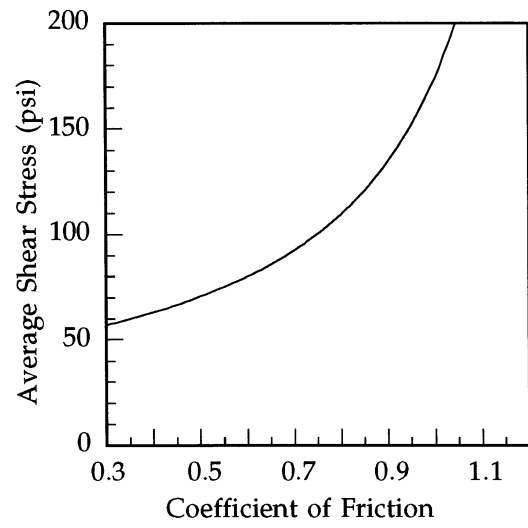


FIGURE 8-32 Shear Strength Dependence on μ

SECTION 9 CONCLUSIONS

The experimental work of this research aimed to address three research needs relating to the evaluation of unreinforced masonry infilled frames. The pseudodynamic experimental program was intended to provide new behavioral information on multi-story, lightly reinforced concrete frames including openings in some of the infill panels. Pseudodynamic testing was used to subject the two-story specimen to realistic seismic demands.

9.1. Pseudodynamic Testing

An explicit PSD testing algorithm proved a successful and viable alternative for testing this specimen of moderate stiffness. Propagation of experimental errors in higher natural modes often have been found to cause significant difficulties in pseudodynamic testing of structures with moderate or high stiffnesses. With the introduction of an actuator control iteration scheme, the explicit PSD algorithm can maintain displacement control errors within a tight tolerance band. The actuator control algorithm relies on physical “soft coupling” of the structural specimen to the actuators, characterized by the displacement control matrix, \mathbf{Q} . As part of this research, a method for direct measurement of \mathbf{Q} , within a traditional static stiffness test, was proposed and successfully executed. The experimentally determined \mathbf{Q} matrix provided excellent displacement control during the final testing sequence, even in the higher level excitations with substantial stiffness degradation.

In order to further guarantee the stability and accuracy of the PSD algorithm, the effects of several parameters in the iteration scheme were investigated with low-level testing. Optimization of certain parameters helped to minimize actuator movement iterations and overshooting, while other parameters prevented actuator control stagnation and iteration convergence failure.

The displacement error characteristics from the PSD tests were carefully studied to ensure accurate and reliable results. Previous PSD error research, based almost entirely on numerical simulation, has suggested that certain peaks in the displacement error frequency spectra can be used to measure the performance of the PSD test. In this research, numerically simulated PSD tests with experimental errors reproduced poor-performance spectral indicators even in what would be considered well-behaved tests based on time history data. No direct performance indicator was found which was consistent with both displacement time histories and error frequency spectra. Analysis of displacement errors from the actual PSD tests verified that error

frequency spectra are not, in fact, reliable measures of performance. Further comparative study between real and simulated PSD errors will be needed to determine the reasons for such discrepancies.

9.2. Experimental Behavior and Strut Mechanisms

Pseudodynamic testing using the Taft 0.10g to 0.80g ground accelerations provided substantial information on the seismic behavior of masonry infill and effects of interaction with the GLD concrete frame. The ability of the structure to resist lateral loads without excessive drift by mobilizing and maintaining effective compressive strut action was found to be closely related to the type of cracking observed—stepped diagonal or bed joint.

Significant cracking damage in the masonry infill appeared in the second story during the Taft 0.55g test. A stepped, diagonal pattern was formed which stabilized with little additional cracking even during the Taft 0.80g test. In contrast, during the Taft 0.80g test, the first story infill deteriorated with long bed-joint shear failures causing large increases in drift and a soft first story response. The bed-joint failures of the first story produced a definite increase in normalized dissipated hysteretic energy, while development of the second story stepped cracks produced no large effect on normalized dissipated hysteretic energy. Although in this experiment the bed-joint failures produced a fairly ductile response with substantial hysteretic energy dissipation, the sliding failures of the masonry do have the potential to cause a sudden and brittle failure of the lightly reinforced concrete bounding frame.

The difference in crack patterns and associated hysteretic behavior between the two stories suggests different idealizations as strut mechanisms may be needed to capture each story's behavior. The first story infill behavior can be characterized by a main diagonal strut at low force levels. However for higher force levels, large bed joint shear failures reduce the effectiveness of the main diagonal strut. The relative sliding of the masonry courses allows for large drifts to occur as the geometry of the infill deforms laterally until it is restrained by the bounding frame. Relative sliding of masonry courses also produces large local forces on the bounding frame, which in this test specimen caused shear cracking in two of the reinforced concrete columns. Any strut action which can form in the heavily damaged lower story walls must be greatly affected in configuration and capacity by the numerous sliding shear planes.

In the second story, the window openings cause compressive struts to form inclined at steep angles so as to pass around the openings. Diagonal stepped cracks form roughly parallel to the inclined struts. The large inclination of the strut provides enough normal force on the bed joints to prevent widespread shear failure. The bed joint shear failures which do occur are

almost entirely above or below the window openings where normal forces are low.

Certain strut models for infill stiffness were found to give reasonable approximations to the measured values for undamaged, full panels. For panels with openings, initial stiffness approximations using a reduction factor based on the opening area could be developed to give acceptable results for a small, similar range of infill types and geometries, but no such method has proven applicable to a wide class of infill types. The importance of masonry shear failure as a limiting factor in lateral strength has been previously recognized, and observed in this experimental program. Existing analytical approximations for lateral shear strength were found to give acceptable estimations of the experimental base shear necessary for development of sliding shear failures. However, such formulations are extremely sensitive to the value of the coefficient of friction used, and no good guidelines exist for determination of the coefficient of friction without extensive material tests.

9.3. Recommendations for Future Research

Proper assessment of the seismic behavior of masonry infilled frames remains a concern, especially in regions of low and moderate seismicity. Both experimental and analytical methods must be pursued to continue to advance the behavioral knowledge of infilled structures. Further experimental effort must be focused on the testing of more realistic multi-story, multi-bay specimens. Pseudodynamic testing recently has been shown to be a viable alternative for testing moderate and large scale specimens, and should be used in conjunction with shake table testing. The controlled testing speed of PSD allows for careful monitoring of crack development, crucial to proper assessment of strut formation and deterioration; although studies of the effects of strain rate on masonry cracking are necessary.

While many of the practical problems of experimental error control in PSD testing have recently been overcome, further development and improvement of advanced control schemes, like the "soft coupling" scheme used in this research, will allow PSD testing to be conducted by more researchers with modest equipment requirements. Finally standardized measures of PSD performance must be developed to ensure reliability and accuracy of results, and such benchmarks must be investigated and developed based on true PSD error data, not just numerical error simulation.

Current equivalent strut models can give acceptable estimates of low-level behavior for relatively undamaged infill panels with no openings. To extend the use of strut models to panels with openings, strut configurations which recognize the geometric constraints and boundary conditions imposed by the openings should be researched. Several multi-strut models already have

been proposed, and their applicability should be tested against previous and new experimental data and finite element models. A better understanding of the nature of the interaction force between frame and infill would help to predict possible local effects on the frame members. These interaction forces could be measured directly by inserting low-profile pressure gages between the frame and infill.

In order to extend strut models beyond low-level load or displacement ranges, certain nonlinear properties must be included. While some strut models have included nonlinear axial behavior, nonlinear shear behavior must also be incorporated, especially for unreinforced masonry infills. Since the shear behavior of masonry infill has been found to be highly sensitive to the coefficient of friction, more extensive research is needed to characterize friction behavior across a wide range of masonry types. Finally, the progression of cracking may impose changing boundary conditions, requiring adapted strut configurations in the nonlinear range.

9.4. Recommendations for Analysis and Design

Based on the results of this experiment and review of some simple analytical techniques proposed by others, several recommendations are offered for analysis and design of unreinforced masonry, infilled frames.

- A range of strut widths from 1/6th to 1/4th of the panel diagonal length will likely bound the true stiffness, although the widths predicted by Eqs. (8.11) and (8.14) should be considered for comparison. Since the lateral stiffness of a typical infilled frame structure will be dominated by the contribution of the diagonal struts, seismic demand may be highly dependent on the assumed strut width. An underestimate of strut width may result in less force being transferred to the masonry, affecting the prediction of cracking or crushing.
- For panels with openings, a multiple strut configuration should be used which recognizes the boundary conditions imposed by the openings. Again, strut widths of between 1/6th and 1/4th of the strut diagonal lengths will likely bound the true stiffness.
- Infill shear strengths based on cohesive bond alone (e.g. FEMA-273, ACI 530, NEHRP 1997) are extremely conservative, as they do not account for the shear-friction contribution produced by the compressive strut action. Potential shear-friction contributions from gravity load should not be used to increase the shear strength as gravity load will be carried by the bounding frame.

- Infill shear-friction models which account for strut action (e.g. Eq. (8.19)) should be used only with a lower-bound coefficient of friction. A value of 0.30 is currently accepted as appropriate. If available, measured coefficients of friction from masonry unit testing should be used only with extreme caution and a close examination of the sensitivity of shear strength to the coefficient of friction.
- The localized forces applied to the bounding frame by the deteriorating masonry should be accounted for by estimating locations of plastic hinging in the frame members and calculating the lateral force associated with such a frame failure mode. For conservative design, the lateral strength of the frame with assumed hinge locations should be greater than the shear strength of the infill, including interaction effects.

SECTION 10 REFERENCES

- Abdel-Mouti, A. (1997). PhD Dissertation, Dept. of Civil Engrg., Aim Shams Univ., Cairo, Egypt. [In preparation].
- Abrams, D.P., ed. (1994). "Proceedings from the NCEER Workshop on Seismic Response of Masonry Infills." *Technical Report NCEER-94-0004*, National Center for Earthquake Engineering Research, State Univ. of N.Y. at Buffalo.
- Abrams, D.P., Calvi, G.M. (1994). "Proceedings of the U.S.-Italy Workshop on Guidelines for Seismic Evaluation and Rehabilitation of Unreinforced Masonry Buildings." *Technical Report NCEER-94-0021*, National Center for Earthquake Engineering Research, State Univ. of N.Y. at Buffalo.
- Angel, R., Abrams, D., Shapiro, D., Uzarski, J., Webster, M. (1994). "Behavior of Reinforced Concrete Frames with Masonry Infills." *Struct. Res. Ser. No. 589, UILU-ENG-94-2005*, Dept. of Civil Engrg., Univ. of Illinois, Urbana-Champaign, Ill.
- American Society for Testing and Materials (ASTM). (1995) *Annual Book of ASTM Standards*, ASTM, Philadelphia, Penn. [N.B. Designation numbers of individual standards are given directly in text.]
- Barua, H.K., Mallick, S.K. (1977). "Behaviour of Mortar Infilled Steel Frames under Lateral Load." *Bldg. and Environ.*, Pergamon Press, 12, 263-272.
- Benjamin, J.R., Williams, H.A. (1957). "The Behavior of One-Story Reinforced Concrete Shear Walls." *J. Struct. Div.*, ASCE, 83(ST3), 1254, 1-49.
- Benjamin, J.R., Williams, H.A. (1958). "The Behavior of One-Story Brick Shear Walls." *J. Struct. Div.*, ASCE, 84(ST4), 1723, 1-30.
- Benjamin, J.R., Williams, H.A. (1958). "Behavior of One-Story Reinforced Concrete Shear Walls Containing Openings." *J. Am. Conc. Inst.*, ACI, 30(5), 605-618.
- Beres, A., White, R.N., Gergely, P. (1992a). "Seismic Behavior of Reinforced Concrete Frame Structures with Nonductile Details: Part I—Summary of Experimental Findings of Full Scale Beam-Column Joint Tests." *Technical Report NCEER-92-0024*, National Center for Earthquake Engineering Research, State Univ. of N.Y. at Buffalo.

- Beres, A., White, R.N., Gergely, P. (1992b). "Experimental Results of Repaired and Retrofitted Beam-Column Joint Tests in Lightly Reinforced Concrete Frame Buildings." *Technical Report NCEER-92-0025*, National Center for Earthquake Engineering Research, State Univ. of N.Y. at Buffalo.
- Beres, A., Pessiki, S.P., White, R.N., Gergely, P. (1996). "Implications of Experiments on the Seismic Behavior of Gravity Load Designed RC Beam-to-Column Connections." *Earthquake Spectra*, EERI, 12(2), 185-198.
- Bertero, V., Brokken, S. (1983). "Infills in Seismic Resistant Building." *J. Struct. Engrg.*, ASCE, 109(6), 1337-1361.
- "Building Code Requirements for Masonry Structures." (1995). *ACI Standard 530-95*, American Concrete Institute (ACI), Farmington Hills, Michigan.
- "Building Code Requirements for Structural Concrete." (1995). *ACI Standard 318-95*, American Concrete Institute (ACI), Farmington Hills, Michigan.
- Buonopane, S. (1997). "Seismic Evaluation of a Masonry Infilled Reinforced Concrete Frame by Pseudodynamic Testing." M.S. Thesis, School of Civil & Environ. Engrg., Cornell Univ., Ithaca, N.Y.
- Buonopane, S. (1995). "Reliability Analysis of Masonry Infilled Frames." Unpublished research report.
- Calvi, G.M., Kingsley, G.R., Magenes, G. (1996). "Testing of Masonry Structures for Seismic Assessment." *Earthquake Spectra*, EERI, 12(1), 145-162.
- Chopra, A.K. (1995). *Dynamics of Structures*. Prentice Hall, Upper Saddle River, N.J.
- Dawe, J.L., Schriver, A.B., Sofocleous, C. (1989). "Masonry Infilled Steel Frames Subjected to Dynamic Load." *Can. J. Civ. Engrg.*, 16, 877-885.
- Dawe, J.L., Seah, C.K. (1989). "Behaviour of Masonry Infilled Steel Frames." *Can. J. Civ. Engrg.*, 16, 865-876.
- Dhanasekar, M., Page, A.W. (1986). "The Influence of Brick Masonry Infill Properties on the Behaviour of Infilled Frames." *Proc. Instn. of Civil Engrs.*, 81(2), 593-605.
- Donea, J., Magonette, G., Negro, P., Pegon, P., Pinto, A., Verzeletti, G. (1996). "Pseudodynamic Capabilities of the ELSA Laboratory for Earthquake Testing of Large Structures." *Earthquake Spectra*, EERI, 12(1), 163-180.

- Drysdale, R.G., Hamid, A.A., Baker, L.R. (1994). *Masonry Structures: Behavior and Design*. Prentice Hall, Englewood Cliffs, N.J.
- El-Attar, A-G., White, R.N., Gergely, P. (1991a). "Shake Table Test of a 1/8 Scale Three-Story Lightly Reinforced Concrete Building." *Technical Report NCEER-91-0018*, National Center for Earthquake Engineering Research, State Univ. of N.Y. at Buffalo.
- El-Attar, A-G., White, R.N., Gergely, P. (1991b). "Shake Table Test of a 1/6 Scale Two-Story Lightly Reinforced Concrete Building." *Technical Report NCEER-91-0017*, National Center for Earthquake Engineering Research, State Univ. of N.Y. at Buffalo.
- El-Attar, A-G., White, R.N., Gergely, P. (1997). "Behavior of Gravity Load Design Reinforced Concrete Buildings Subjected to Earthquakes." *ACI Struct. J.*, 94(2), 133-145.
- "FEMA-273. NEHRP Guidelines for the Seismic Rehabilitation of Buildings" (1997). Building Seismic Safety Council, Washington, D.C.
- Harris, H.G., Ballouz, G.R., Kopatz, K.W. (1993). "Preliminary Studies in Seismic Retrofitting of Lightly Reinforced Concrete Frames Using Masonry Infills." *The 6th North American Masonry Conf.* Philadelphia, Penn.
- Hendry, A.W. (1990). *Structural Masonry*. MacMillan Education, Ltd., London.
- Hilber, H., Hughes, T., Taylor, R. (1977). "Improved Numerical Dissipation for Time Integration Algorithms in Structural Dynamics." *Earthquake Engrg. Struct. Dyn.*, 5, 283-292.
- Holmes, M. (1961). "Steel Frames with Brickwork and Concrete Infilling." *Proc. Instn. of Civil Engrs.*, 19, 473-478.
- Holmes, M. (1963). "Combined Loading on Infilled Frames." *Proc. Instn. of Civil Engrs.*, 25, 31-38.
- Igarashi, A., Seible, F., Hegemeir, G., Priestley, M.J.N. (1994). "The U.S.-TCCMAR Full-Scale Five-Story Masonry Research Building Test: Part III - Seismic Load Simulation." *Struct. Systems Res. Proj., Rep. No. SSRP-94/03*, University of California, San Diego, La Jolla, Calif.
- Jirsa, J.O., ed. (1996). "Theme Issue: Repair and Rehabilitation Research for Seismic Resistance of Structures." *Earthquake Spectra*, EERI, 12(4).
- Kahn, L.F., Hanson, R.D. (1979). "Infilled Walls for Earthquake Strengthening." *J. Struct. Div.*, ASCE, 105(ST2), 283-296.


- Kim, W., El-Attar, A-G., White, R.N. (1988). "Small-Scale Modeling Techniques for Reinforced Concrete Structures Subjected to Seismic Loads." *Technical Report NCEER-88-0041*, National Center for Earthquake Engineering Research, State Univ. of N.Y. at Buffalo.
- Klingner, R.E., Bertero, V.V. (1976). "Infilled Frames in Earthquake-Resistant Construction." *Report No. EERC 76-32*, Earthquake Engrg. Res. Ctr., University of California, Berkeley, Calif.
- Kosmatka, S.H., Panarese, W.C. (1988). *Design and Control of Concrete Mixtures*, 13th Ed. Portland Cement Association, Skokie, Ill.
- Liauw, T.C. (1970). "Elastic Behaviour of Infilled Frames." *Proc. Instn. of Civil Engrs.*, 46, 343-349.
- Liauw, T.C. (1979). "Tests on Multistorey Infilled Frames Subject to Dynamic Lateral Loading." *ACI Journal*, 76(4), 551-563.
- Liauw, T.C., Kwan, K.H. (1982). "Non-Linear Analysis of Multistorey Infilled Frames." *Proc. Instn. of Civil Engrs., Part 2*, 73, 441-454.
- Liauw, T.C., Kwan, K.H. (1983a). "Plastic Theory of Non-Integral Infilled Frames." *Proc. Instn. of Civil Engrs., Part 2*, 75, 379-396.
- Liauw, T.C., Kwan, K.H. (1983b). "Plastic Theory of Infilled Frames with Finite Interface Shear Strength." *Proc. Instn. of Civil Engrs., Part 2*, 75, 707-723.
- Liauw, T.C., Kwan, K.H. (1984). "Nonlinear Behaviour of Non-Integral Infilled Frames." *Comps. & Structs.*, Pergamon Press, 18(3), 551-560.
- Liauw, T.C., Kwan, K.H. (1984). "Plastic Design of Infilled Frames." *Proc. Instn. of Civil Engrs., Part 2*, 77, 367-377.
- Liauw, T.C., Kwan, K.H. (1985). "Static and Cyclic Behaviours of Multistorey Infilled Frames with Different Interface Conditions." *J. Sound & Vibr.*, 99(2), 275-283.
- MacGregor, J.G. (1988). *Reinforced Concrete: Mechanics and Design*, 2nd Ed. Prentice Hall, Englewood Cliffs, N.J.
- Mahin, S., Shing, P.B. (1985). "Pseudodynamic Method for Seismic Testing." *J. Struct. Engrg.*, ASCE, 111(7), 1482-1503.
- Mahin, S., Shing, P.B., Thewalt, C.R., Hanson, R.D. (1989). "Pseudodynamic Test Method—Current Status and Future Directions." *J. Struct. Engrg.*, ASCE, 115(8), 2113-2128.

- Mainstone, R.J. (1971). "On the Stiffnesses and Strengths of Infilled Frames." *Proc. Instn. of Civil Engrs. Suppl.*, 57-89.
- Mallick, D.V., Garg, R.P. (1971). "Effect of Openings on the Lateral Stiffness of Infilled Frames." *Proc. Instn. of Civil Engrs.*, 49, 193-209.
- Mallick, D.V., Severn, R.T. (1967). "The Behaviour of Infilled Frames under Static Loading." *Proc. Instn. of Civil Engrs.*, 38, 639-656.
- Mallick, D.V., Severn, R.T. (1968). "Dynamic Characteristics of Infilled Frames." *Proc. Instn. of Civil Engrs.*, 39, 261-287.
- Mander, J.B., Nair, B., Wojtkowski, K., Ma, J. (1993). "An Experimental Study on the Seismic Performance of Brick-Infilled Steel Frames With and Without Retrofit." *Technical Report NCEER-93-0001*, National Center for Earthquake Engineering Research, State Univ. of N.Y. at Buffalo.
- MATLAB (1993). *Signal Processing Toolbox User's Guide*. The MathWorks, Natick, Mass.
- Mehrabi, A.B., Shing, P.B., Schuller, M.P., Noland, J.L. (1994). "Performance of Masonry Infilled R/C Frames Under In-Plane Lateral Loads." *Research Series No. CU/SR-94/6*. Dept. of Civil, Environ. & Arch. Engrg., University of Colorado, Boulder, Col.
- Mehrabi, A.B., Shing, P.B., Schuller, M.P., Noland, J.L. (1996). "Experimental Evaluation of Masonry-Infilled RC Frames." *J. Struct. Engrg.*, ASCE, 122(3), 228-237.
- Mosalam, K.A.M. (1996). "Experimental and Computational Strategies for the Seismic Behavior Evaluation of Frames with Infill Walls." PhD Dissertation, School of Civil & Environ. Engrg., Cornell Univ., Ithaca, N.Y.
- Nakashima, M., Kaminosono, T., Ishida, M., Ando, K. (1990). "Integration Techniques for Substructure Pseudodynamic Testing." *Proc. 4th U.S. Natl. Conf. on Earthquake Engrg.*, Palm Springs, Calif., II, 515-524.
- National Center for Earthquake Engineering Research. (1994). "Research Accomplishments: 1986-1994." NCEER, State Univ. of N.Y. at Buffalo.
- Negro, P., Pinto A.V., Verzeletti, G., Magonette, G.E. (1996). "PsD Test on Four-Story R/C Building Designed According to Eurocodes." *J. Struct. Engrg.*, ASCE, 122(12), 1409-1417.
- "NEHRP Recommended Provisions for Seismic Regulations for New Buildings." (1997). Building Seismic Safety Council, Washington, D.C.

- Paulay, T., Priestley, M.J.N. (1992). *Seismic Design of Reinforced Concrete and Masonry Buildings*. John Wiley and Sons, New York, N.Y.
- Peek, R., Yi, W-H. (1990a). "Error Analysis for Pseudodynamic Test Method. I: Analysis." *J. Engrg. Mech.*, ASCE, 116(7), 1618-1637.
- Peek, R., Yi, W-H. (1990b). "Error Analysis for Pseudodynamic Test Method. II: Application." *J. Engrg. Mech.*, ASCE, 116(7), 1638-1658.
- Pessiki, S.P., Conley, C.H., Gergely, P., White, R.N. (1990). "Seismic Behavior of Lightly-Reinforced Concrete Column and Beam-Column Joint Details." *Technical Report NCEER-90-0014*, National Center for Earthquake Engineering Research, State Univ. of N.Y. at Buffalo.
- Pires, F., Carvalho, E.C. (1992). "The Behaviour of Infilled Reinforced Concrete Frames Under Horizontal Cyclic Loading." *Proc. 10th World Conf. on Earthquake Engrg.*, Madrid, 8, 3419-3422.
- Sabnis, G.M., Harris, H.G., White, R.N., Mirza, M.S. (1983). *Structural Modeling and Experimental Techniques*. Prentice Hall, Englewood Cliffs, N.J.
- Sachanski, S. (1960). "Analysis of the Earthquake Resistance of Frame Buildings Taking into Consideration the Carrying Capacity of the Filling Masonry." *Proc. 2nd World Conf. on Earthquake Engrg.*, Tokyo, III, 2127-2141.
- San Bartolomé, A., Quinn, D., Torrealva, D. (1992). "Seismic Behaviour of a Three-Story Half Scale Confined Masonry Structure." *Proc. 10th World Conf. on Earthquake Engrg.*, Madrid, 8, 3527-3531.
- Scaletti, H., Chariarse, V., Cuadra, C., Cuadros, G., Tsugawa, T. (1992). "Pseudodynamic Tests of Confined Masonry Buildings." *Proc. 10th World Conf. on Earthquake Engrg.*, Madrid, 8, 3493-3497.
- Seible, F., Hegemier, G.A., Igarashi, A., Kingsley, G.R. (1994a). "Simulated Seismic-Load Tests on Full-Scale Five Story Masonry Building." *J. Struct. Engrg.*, ASCE, 120(3), 903-924.
- Seible, F., Priestley, M.J.N., Kingsley, G.R., Kürkchübasche, A.G. (1994b). "Seismic Response of Full-Scale Five Story Reinforced-Masonry Building." *J. Struct. Engrg.*, ASCE, 120(3), 925-946.
- Seible, F., Hegemier, G.A., Igarashi, A. (1996). "Simulated Seismic Laboratory Load Testing of Full-Scale Buildings." *Earthquake Spectra*, EERI, 12(1), 57-86.

- Shen, J., Zhu, R. (1994). "Earthquake Response Simulation of Reinforced Concrete Frames with Infilled Brick Walls by Pseudo-Dynamic Test." *Earthquake Resistant Construction & Design*, (Savdis, ed.), Balkema, Rotterdam, 955-962.
- Shing, P.B., Mahin, S. (1985). "Computational Aspects of a Seismic Performance Test Method Using On-Line Computer Control." *Earthquake Engrg. Struct. Dyn.*, 13, 507-526.
- Shing, P.B., Mahin, S. (1987a). "Cumulative Experimental Errors in Pseudodynamic Tests." *Earthquake Engrg. Struct. Dyn.*, 15, 409-424.
- Shing, P.B., Mahin, S. (1987b). "Elimination of Spurious Higher-Mode Response in Pseudodynamic Tests." *Earthquake Engrg. Struct. Dyn.*, 15, 425-445.
- Shing, P.B., Mahin, S. (1990). "Experimental Error Effects in Pseudodynamic Testing." *J. Engrg. Mech.*, ASCE, 116(4), 805-821.
- Shing, P.B., Vannan, M.T. (1991). "Implicit Time Integration for Pseudodynamic Tests: Convergence and Energy Dissipation." *Earthquake Engrg. Struct. Dyn.*, 20, 809-819.
- Shing, P.B., Vannan, M.T., Cater, E. (1991). "Implicit Time Integration for Pseudodynamic Tests." *Earthquake Engrg. Struct. Dyn.*, 20, 551-576.
- Shing, P.B., Nakashima, M., Bursi, O.S. (1996). "Application of Pseudodynamic Test Method to Structural Research." *Earthquake Spectra*, EERI, 12(1), 29-56.
- Stafford Smith, B. (1962). "Lateral Stiffness of Infilled Frames." *J. Struct. Div.*, ASCE, 88(ST6), 183-199.
- Stafford Smith, B. (1966). "Behavior of Square Infilled Frames." *J. Struct. Div.*, ASCE, 92(ST1), 381-403.
- Stafford Smith, B. (1967). "Methods for Predicting the Lateral Stiffness and Strength of Multi-Storey Infilled Frames." *Build. Sci.*, Pergamon Press, 2, 247-257.
- Stafford Smith, B. (1968). "Model Test Results of Vertical and Horizontal Loading of Infilled Frames." *ACI Journal*, 65-44, 618-624.
- "Standard Practice for Selecting Proportions for Normal, Heavyweight, and Mass Concrete." (1991). *ACI Standard 211.1-91*, American Concrete Institute (ACI), Farmington Hills, Michigan.

- Takanashi, K., Udagawa, K., Seki, M., Okada, T., Tanaka, H. (1975). "Nonlinear Earthquake Response Analysis of Structures by a Computer-Actuator On-Line System." *Bull. of Earthquake Resistant Struct. Res. Ctr. No. 8*, Instn. of Indust. Science, University of Tokyo, Japan.
- Takanashi, K., Nakashima, M. (1987). "Japanese Activities on On-Line Testing." *J. Engrg. Mech.*, ASCE, 113(7), 1014-1032.
- Thewalt, C.R. (1994). "Performance Parameters for Pseudodynamic Tests" *J. Struct. Engrg.*, ASCE, 120(9), 2768-2781.
- Thewalt, C.R., Mahin, S. (1995). "An Unconditionally Stable Hybrid Pseudodynamic Algorithm." *Earthquake Engrg. Struct. Dyn.*, 24, 723-731.
- Todeschini, C.E., Bianchini, A.C., Kesler, C.E. (1964). "Behavior of Concrete Columns Reinforced with High Strength Steels." *J. Am. Conc. Inst.*, ACI, 61(6), 701-716.
- Wood, R.H. (1958). "The Stability of Tall Buildings." *Proc. Instn. of Civil Engrs.*, 11, 69-102.
- Yamazaki, Y., Nakashima, M., Kaminosono, T. (1989). "Reliability of Pseudodynamic Test in Earthquake Response Simulation." *J. Struct. Engrg.*, ASCE, 115(8), 2098-2112.
- Zahrah, T.F., Hall, W.J. (1984). "Earthquake Energy Absorption in SDOF Structures." *J. Struct. Engrg.*, ASCE, 110(8), 1757-1772.
- Zarnic, R. (1994a). "Experimental Investigation of the R/C Frame Infilled by Masonry Wall." *Experimental Modelling*, 7(1-2), 37-45.
- Zarnic, R. (1994b). "Inelastic Model of R/C Frame with Masonry Infill—Analytical Approach." *Experimental Modelling*, 7(1-2), 47-54.
- Zarnic, R., Tomazevic, M. (1984) "Study of the Behaviour of Masonry Infilled Reinforced Concrete Frames Subjected to Seismic Loading—Part One." *Report*, Institute for Testing and Research in Materials and Structures, Ljubljana, Yugoslavia.
- Zarnic, R., Tomazevic, M. (1985) "Study of the Behaviour of Masonry Infilled Reinforced Concrete Frames Subjected to Seismic Loading—Part Two." *Report*, Institute for Testing and Research in Materials and Structures, Ljubljana, Yugoslavia.
- Zawilinski, D. (1994) "Experimental Investigation of Infilled Frames Under Lateral Loading." MS Thesis, School of Civil & Environ. Engrg., Cornell Univ., Ithaca, N.Y.



MULTIDISCIPLINARY CENTER FOR EARTHQUAKE ENGINEERING RESEARCH

A National Center of Excellence in Advanced Technology Applications

University at Buffalo, State University of New York
Red Jacket Quadrangle ■ Buffalo, New York 14261-0025
Phone: 716/645-3391 ■ Fax: 716/645-3399
E-mail: mceer@acsu.buffalo.edu ■ WWW Site: <http://mceer.buffalo.edu>



University at Buffalo *The State University of New York*

ISSN 1520-295X